



Department of Precision and Microsystems Engineering

A study on Micro-Actuators for Atomic Force Microscopes

Name: Chonghe Zhong

Report no: PT 11.038

Coach: Johan F.C. van Gorp

Professor: Urs Staufer

Specialisation: Micro and Nano Engineering

Type of report: Master thesis

Date: 30/10/2011

25 October, 2011

Internship & Final MSc Project combined (part two)
for Mister
C. Zhong

Comparative Micro-Actuator Study

Introduction:

The current MSc Project aims at comparing voice coil and piezo actuators for scanning probe applications and proposes solutions for improving fabrication costs, robustness and performance. This project is in collaboration with the company Nanosurf AG, an innovative manufacturer for scanning tunneling and scanning force microscope for industrial applications. Their product is currently the only one on the market based on voice coil actuators. This solution has some advantages and some drawbacks. The goal is to evaluate them and compare them to solutions with piezo actuators.

The following criteria shall be considered (the list does not reflect the priority):

1. Compactness of design and the possibility for further miniaturization.
2. Frequency bandwidth and scan speed (3D) considering scan range and including aspects of the driver electronics.
3. Cost for the scan head and the driver electronics.
4. Heat generation and required cooling.
5. Performance in terms of linearity, creep, aging, resonances, quality factor.
6. Cross-coupling (Mechanical and electrical)
7. Control algorithms.

Assignment:

1. Conduct an experimental characterization of the currently used scanners Nanit A and B.
2. Experimentally characterize a new type of electromagnetic z-actuator and compare it to the Nanit A and B.

Based on this analyses suggestions to the following production related questions shall be derived:

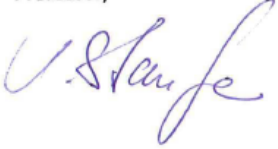
1. Develop a Flex design for z-piezo actuators and compare it to the electromagnetic actuators Nanit A and B.
2. Simulate a miniaturized version of this piezo-flex actuator to be accommodated in an existing scan head.
3. Describe possibilities to reduce the sensitivity for seismic disturbances using compensation masses (mainly for voice coil actuators).

Starts: 15 January 2011
Finishes: 15 September 2011

Study-input: 35+15=50 ECTS
O.E.-code: ME2400-15 & ME2490-35

Coaching: Ir. J.F.C. van Gurp

Professor,



Prof.dr. U. Staufer

Acknowledgements

I would like to express my gratitude to all the people who have contributed to my thesis. First of all, I would like to thank Prof. Urs Staufer, my project supervisor. I think that by encouraging me to discover the underlying reason of everything encountered, and offering new ideas in solving problems, and spending times in discussing problems, he teaches me what a real engineer should do in practical scientific researches. I would like to thank the people working at Nanosurf in Liestal, who always strive to bring their products in a high level. Especially, my thanks go to Lukas Howald who initialized this nice project and provided me the opportunity to collaborate with his company. My grateful heart also goes to Hans van Gorp, an excellent PhD researcher, who offered many suggestions and creative ideas in the process of this project. His willingness to help makes the whole project go much smoother. I am also very grateful to Hugo Perez Garza, who is always keen to help and gave me a great amount of help on the lab instruments.

I would like to thank Merlijn van Spengen and Rene Poelma for sharing their innovative lab equipment. Many thanks to Rob Luttjeboer, Harry Jansen, Patrick van Holst and Jos van Driel for their lab support. I also think with gratitude of my officemates: Ronald Stoute, an intelligent guy who is never tired of answering my questions; Eda Kuran who gave a lot of aid with COMSOL simulations, Federico Buja who is always ready to help and nice to work with, and of course, the already graduated Kees Schilder and the new smart guy, Dominik Kohl. I would not accomplish my master education without the help of Jan Neve, the Msc Coordinator, and the lovely Marli Guffens. It is a great honor to work with all the people in the MNE group.

Last but not least, I am very grateful to my grandma Weifen Lu, my parents Meixiang Yu and Weiping Zhong for their loving support during my years of education. Their foresights of supporting me to study abroad make what I am today, and the experience of studying and living in the Netherlands will definitely benefit me all lifelong.

Summary

With the extraordinary imaging function, Atomic Force Microscope has become an indispensable tool for various industrial applications, especially for scientific researches. This thesis focuses on studying the micro actuators in the Nanite systems, a product line of Atomic Force Microscopes developed by Nanosurf. Currently, the Nanite family comprises two members, Nanite A and Nanite B, both adopting the triangular-formed electromagnetic actuator for the probe driving. This actuation structure is designed to be capable of 3-axis scanning, with a maximum driving range of about 100 μ m separately along the predefined x and y axis, and of 10 μ m along its z axis. In the scanning process, as the cantilever chip needs to follow the sample topography to timely reflect the depth information, a fast and accurate actuation process (perpendicular to the sample surface) is needed. Among all the influencing parameters, the actuation resonance frequency is a key factor in determining the scanning speed, and is therefore imperative to know. To achieve that, the Laser Doppler Vibrometer "MSA 400" from Polytec is utilized to characterize the dynamic properties of the z-axis actuation for the old versioned actuator- the actuator used in Nanite A and B. With proper connections and multiple tests, this first actuation resonance frequency characterized to be in the order of 205Hz.

To boost the system's performance, a different actuation concept is conceived in developing the new Nanite generation. In this concept, the actuators are decoupled from each other, meaning that individual electromagnetic actuators are employed to independently accomplish the actuations along different axes. In this sense, the z actuator, responsible for the z axis actuation, deserves of investigations. To better understand this new z actuator and to know some of its paramount parameters, some simulations and practical experiments are involved and discussed. With the help of COMSOL MULTIPHYSICS, a simulation model is established, and the generated Lorentz force is estimated to be in the range of 0.0353N ~0.0597N, which is considered to be large enough (compared to the weight of the bending structure) for actuation. As the linearity is very important for an AFM actuator, the relation between the maximum deflection and the power input is investigated. With the help of a high resolution camera, the deflection of the flexprint is traced under different power inputs. The result shows a proportional relation in between the two parameters, with a linear increasing rate of approximately 15.8 μ m/V (for two sides bending). This means that for a static current input of about 150mA, the generated deflection could be around 10.67 μ m, which is more or less the same as what the previous actuator (the actuator used in Nanite A and B) can achieve. Assisted with the Laser Doppler Vibrometer (LDV), the dynamic response of this new z actuator is obtained. The characterized resonance frequency is about 1150Hz, which is much higher than what the old version can achieve. This indicates that without influencing the other criteria too much, the z actuator in the new Nanite generation can be operated in a higher frequency and thus can achieve a higher scan speed. On the other hand, since the thermal issue is not negligible for the MEMS structures, it is necessary to check how heat is conducted through the flexprint and whether it is sufficient. In terms of that and further to check whether the size of the bonding pad influences the heat conduction, thermal camera "FLIR 315" is utilized to obtain the thermal topographies of the two flexprint designs (at the room temperature). It is discovered that the maximum temperature always appears in the middle of the coils no matter how large the bonding pad is. It also gives information that the flexprint with big bonding pads has a lower maximum temperature (55.6 $^{\circ}$ C) in comparison with the design having small bonding pads (61.1 $^{\circ}$ C). Besides, through simulations, we clearly see the temperature span in the big-bonding-pad case is much smaller than the other one. All the phenomena indicate the size of the bonding pad does influence the heat conduction in the flexprint, and fact is the larger the bonding pad is, the more efficient the heat conduction will be.

As piezoelectric materials have superior properties (such as low mass, high actuation resolution, large generated force, and low power consumption) on Micro actuation, possible actuating concepts are conceived on the basis of

the ceramic bimorph bender "CMBP02" to replace the electromagnetic actuator used in the new Nanite generation. In process of the brainstorming, the concept "half actuator" and "symmetric actuator" are initially considered to be more potential in replacing the electromagnetic actuator used in the new Nanite generation. By using COMSOL simulation, these two concepts are further compared from multiple aspects, including the actuation stroke, the resonance frequency, the mass, volume and the cost. Judging from the results, the half actuators show more promising qualities in achieving the actuation task. It is therefore considered to be a good alternative.

As the ultimate goal is to adapt the half bimorph actuator to the main AFM body, there will be many requirements limiting the design flexibility, such as the volume, the mass, and the desired performances. However, as this concept is still in its infancy, the requirements are not really specified. To benefit the miniaturization step in the future, simulations are done to explore the influencing parameters on the maximum deflection (including the power input, the individual bender length, and the overlap of the two adjacent benders). The results show that the maximum deflection is proportional to the power input and in proportion to the square of the individual bender length, but inversely proportional to the overlap in between. To verify the simulations, we further build the actuators (with different actuating layers) up. With the White Light Interferometer and reference planes, we successfully measured the approximate deflections under different power inputs, and the dynamic responses are also obtained with the help of the LDV. The simulation and test result for both cases are more or less the same. This proves that the simulations can be actually used as a good reference for parameter selections in the miniaturization step.

Contents

Acknowledgements	V
Summary.....	VII
Contents	IX
List of Figures.....	XI
List of Tables	XIII
1 Introduction	1
1.1 State of Art.....	1
1.2 Task Description.....	2
2 Theoretical Background	5
2.1 The Configuration of AFM.....	5
2.2 Operating Modes [10].....	9
2.3 Actuators.....	10
2.3.1 Piezoelectric actuators in AFM.....	10
2.3.2 Electromagnetic actuators in AFM.....	13
3 Characterization of the Dynamics of the Actuator in Nanite A and Nanite B.....	17
3.1 Principle of Laser Doppler Vibrometer	17
3.1.1 Out-of-plane motion detection.....	17
3.1.2 In-plane motion detection	19
3.2 Measurement Setup	19
3.2.1 Test sample	19
3.2.2 Input signal.....	20
3.2.3 Measurement setup.....	20
3.2.4 Measuring strategies.....	21
3.3 Result and Discussion.....	22
3.3.1 Measurements along the z' axis.....	22
3.3.2 Measurements along the z axis.....	26
4 Characterizations of the z Actuator in the New Nanite Generation	29
4.1 Simulation of the Lorentz force	30
4.2 Characterization of the deflection	31
4.3 Characterization of the resonance frequency	33
4.3.1 Calculations.....	33
4.3.2 Measurement and result.....	34
4.4 Characterization of the heat conduction	35
4.4.1 Simulations.....	36
4.4.2 Measurement and result.....	38
5 Bimorph Actuator for the Next Nanite Generation	41
5.1 Concepts of the Bimorph Actuator	41
5.2 Concept Comparisons	43
5.2.1 Comparison of the Deflection	43
5.2.2 Comparison of the Resonance Frequency	45
5.2.3 Other comparisons.....	46
5.3 Simulations of the Influencing Parameters.....	47
5.3.1 Power input.....	47
5.3.2 Individual bender length	48

5.3.3 Glue width/overlap	48
5.4 Built-up Actuators	49
5.5 Measurement	49
5.5.1 Deflection measurement	49
5.5.2 Frequency Measurement	50
6 Conclusions and Recommendations	53
Bibliography	57
Appendices	59
Appendix A: Literature Review for the AFM actuators	59
A.1 Introduction	59
A.2 Actuator Concepts	61
A.3 Performance Criteria	71
A.4 Problems and solutions	75
A.5 Conclusions	87
A. References	89
Appendix B	93
Appendix C	94
Appendix D	95

List of Figures

Figure 1. 1, different AFM actuators: a, tripod actuator; b, bimorph actuator; c, piezoelectric tube actuator	1
Figure 2. 1, the quantum tunneling effect.....	5
Figure 2. 2, tunneling effect used in STM between the probe and the sample	5
Figure 2. 3, the interaction force between the probe and the sample (the principle of the AFM).....	6
Figure 2. 4, the interaction force between the probe and the sample in the process of approaching one to the other [7].....	6
Figure 2. 5, a, the fabricated wafer with cantilever chips on; b, a single cantilever chip; c, magnified picture of the cantilever beam; d, the probe [8].....	7
Figure 2. 6, light reflection based signal detection mechanism	7
Figure 2. 7, probe scan	8
Figure 2. 8, sample scan	8
Figure 2. 9, the general configuration of an AFM.....	9
Figure 2. 10, a, the static operating mode; b, the dynamic operating mode	9
Figure 2. 11, the atom distributions in a piezoelectric cubic lattice: before force treatment (left) and after (right) force treatment.	11
Figure 2. 12, the tripod actuator, constructed with three piezo bars perpendicular connected	11
Figure 2. 13, bimorph actuator: left) the series bimorph; right) the parallel bimorph [12]	12
Figure 2. 14, the piezoelectric tube actuator	13
Figure 2. 15, the basic principle of an electromagnetic actuator [13].....	13
Figure 2. 16, the actuation concept used in Nanite A and B	14
Figure 2. 17, the actuator for x- and y- axis actuating	15
Figure 2. 18, the vertical actuation concept.....	15
Figure 2. 19, the actuation concept for z axis actuating.....	16
Figure 2. 20, the compositional concept of 3D scanning.....	16
Figure 3. 1, the general working principle of a laser vibrometer	18
Figure 3. 2, the test sample, marked with the actuator's coordinate system and the cantilever chip's coordinate system.....	19
Figure 3. 3, the signal processing mechanism used in a general Nanite system	20
Figure 3. 4, the measuring mechanism with the frequency changing signal.....	20
Figure 3. 5, the configuration of the measurement setup	21
Figure 3. 6, the BNC breakout box from Nanite B	21
Figure 3. 7, the orientations of the sample: left) for measurement along the z' axis, right) for measurement along the cantilever chip's z axis	22
Figure 3. 8, the displacement response of the actuator A, B, and C with 8V z-axis input	23
Figure 3. 9, the velocity response of the actuator A, B, and C with 8V z-axis input	23
Figure 3. 10, the displacement response of the actuator A, B, and C with 3V z-axis input	24
Figure 3. 11, measuring mechanism without input	24
Figure 3. 12, measuring mechanism without controller.....	24
Figure 3. 13, measurement with and without input/ controller	25
Figure 3. 14, the displacement response of the actuator A, B, and C with 8 V x-axis input.	26
Figure 3. 15, the displacement response of the actuator A, B, and C with 8V y-axis input.....	26
Figure 3. 16, the actuation frequency responses with respect to the three measurement points.....	27

Figure 3. 17, the actuation responses with input signal (pink) and without input signal.....	27
Figure 4. 1, left) the test sample: the flexprint with coil inside was suspended through a fabricated frame (black) which is additionally utilized to hold the magnets from an orthogonal direction; right) the corresponding driving mechanism.	29
Figure 4. 2, the real coil structure with its cross section	30
Figure 4. 3, the simulation model for the Lorentz Force	30
Figure 4. 4, left) magnetic flux density; right) the force distribution.	31
Figure 4. 5, the side view image of the flexprint's end.....	32
Figure 4. 6, power input vs. maximum deflection.	32
Figure 4. 7, the dynamic response of the new z actuator under treatment of 0.4V(green), 0.8 V(blue) , 1.0V(red) and no input (black).....	34
Figure 4. 8, the dynamic response of the new z actuator under a treatment of 1.0V (red), no input (black) and the dynamic response of the clamp structure (cyan)	35
Figure 4. 9, flexprint with different sized banding pads.	36
Figure 4. 10, temperature distribution on the flexprint: left) with small bonding pad; right) with big bonding pad .	36
Figure 4. 11 a simulation on the metal pad area.	38
Figure 4. 12, left) the device for heat conduction measurement; right) the device in a vacuum chamber.	38
Figure 4. 13, thermal topography images of the flexprint: left) with small bonding pad; right) with big bonding pad.	39
Figure 5. 1, ceramic bimorph bender "CMBP02"	41
Figure 5. 2, a, single beam deflection, , with a generated angle θ at the beam end with respect to the horizontal line ; b, structure with two bimorph benders; c, structure with three bimorph benders.	42
Figure 5. 3, two benders connected endto end, with their polarization positioned in different direction.....	42
Figure 5. 4, the symmetric actuator	42
Figure 5. 5, benders joint with overlap.....	42
Figure 5. 6, left) half actuator with 4-layer design; right) symmetric actuator with 3-layer design.....	43
Figure 5. 7, the deformation of the platform: left) from the half actuator with 1-layer design; right) from the symmetric actuator with 1-layer design. 错误! 未定义书签。	43
Figure 5. 8, the frequency responses of the "half actuators". the first resonance frequency with respect to the 1-layer design, 2-layer design, 3-layer design, 4-layer design separately appears at 370Hz, 250Hz., 160Hz, and 120Hz.	45
Figure 5. 9, the frequency responses of the " symmetric actuators". The first resonance frequency with respect to the 1-layer design, 2-layer design, 3-layer design, 4-layer design separately appears at 820Hz, 280Hz, 200Hz, and 150Hz.	46
Figure 5. 10, the relation between the power input and the platform deflection	47
Figure 5. 11, the influence of individual bender length on different structure designs.....	48
Figure 5. 12, the influence of the glue width on maximum deflection of the platform.	49
Figure 5. 13, the built-up half actuators, from left to right, the 1-layer design, 2-layer design and the 3-layer design.	49
Figure 5. 14 , left) the height difference between the bender (pink) and the reference plane (dark red); right) 2 Dimensional representation of the height difference.	50
Figure 5. 15, the deflection comparisons between the measurement and the previous simulation	50
Figure 5. 16, the dynamic responses from the three actuators, from the top to the bottom are separately the responses from the 1-layer design, 2-layer design and the 3-layer design.	51
Figure B 1, the electric driving circuit for the actuator in Nanite A and B.....	93

List of Tables

Table 4. 1, the magnetic flux density at different coil spirals	31
Table 5. 1, the deflections of the half actuators and symmetric actuators with respect to different layer designs...	44
Table 5. 2, the comparison table	47
Table 5. 3, deflection measurement with respect to different designs under different power inputs.....	50
Table C 1, the pixel shift of different points under different power input.	94
Table C 2, the corresponding deflection calculated based on the pixel shifts in Table B1.....	94
Table D 1, the influence of the power input on the maximum deflection.	95
Table D 2, the influence of the bender length on the maximum deflection.	95
Table D 3, the influence of the overlap/glue width on the maximum deflection	96

Introduction

1.1 State of Art

As a fundamental device in exploring the micro and nano world, the Atomic Force Microscope, acronymed AFM, plays an indispensable role on providing either visible images of topographies of targeted samples or real-time images of some manipulation processes. Among all the components comprising the AFM, the actuator is one of the most critical parts in helping to achieve the scan motion, a process aiming at activating the probe to move along different axes and acquiring the information of the sample topography. In the light of this situation, the properties of an actuator, such as its scan range and achievable resolution, have direct bearings on the quality of the final image.

Different concepts have been conceived for the AFM actuation, from the initial “tripod” structure by using three orthogonal piezo bars to achieve 3 DOFs (Figure 1.1 a), to the subsequent “bimorph” feature with two stacked piezocrystal planes (Figure 1.1b), to the recently emerged piezoelectric tube concept (Figure 1.1c) which is widely used in some of today’s AFMs [1][2]. All of the three actuating mechanisms are based on the piezoelectric effect. However, with the enhancement of the actuator performance, some drawbacks with piezoelectric materials, such as hysteresis, creep and aging [Appendices A.4] [4], are discovered, which, although possible to be attenuated, are difficult to be eliminated.

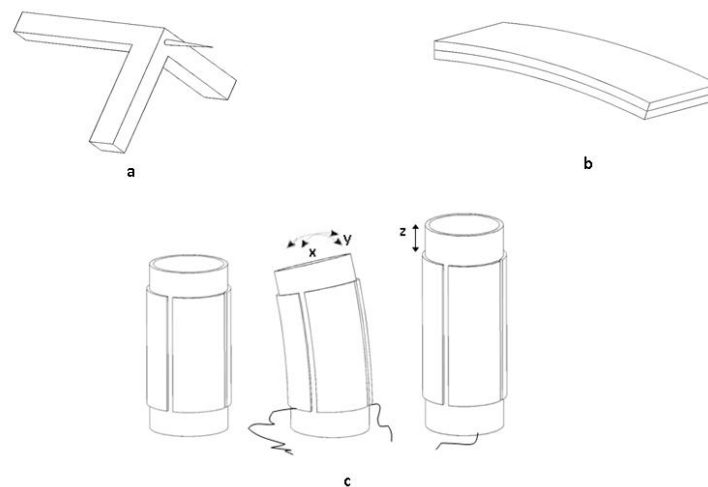


Figure 1. 1, different AFM actuators: a, tripod actuator; b, bimorph actuator; c, piezoelectric tube actuator

Being a leading supplier, Nanosurf provides worldwide researchers and professionals easy-to-use AFMs to measure and analyze surface structures of different samples. Unlike the actuators in Figure 1.1, Nanosurf exploits the

electromagnetic effect as a major technique to develop its actuators. In the course of developing high-performance AFM systems, Nanosurf dedicates itself to the explorations of new techniques and driving mechanisms, and has already innovated and launched several different products to the market.

1.2 Task Description

The idea of this thesis is to investigate the actuators in different Nanite generations. According to the emphases of different tasks, the whole content can be grouped into two parts: the first part is the characterization part, including the measurement of the dynamic response of the old versioned actuator (the actuator used in the Nanite A and Nanite B), as well as the characterizations of the z actuator for the new Nanite generation; the second part would be the design and simulation part, which aims at finding potential piezo actuating concept (on the basis of the ceramic bimorph bender "CMBP02"), such that it can replace the z actuator used in the new Nanite generation. The key consideration of this substitution is that the piezoelectric actuators are normally much lighter in weight than the electromagnetic actuators. As the z actuator in the new Nanite generation needs to be attached on the x-y platform which is activated by the x and y actuators, a light weighted z actuator is therefore preferred to avoid possible impacts. The structure of this thesis and the concrete questions to be answered in each chapter can be found as follows:

To start off the discussion, some theoretical background information is demonstrated in Chapter 2, including the configuration of a general AFM system, the functions of different ingredients, the AFM operating modes, the working principle of the actuator used in Nanite A/B, the concept of current developing actuator, and relevant information about the piezoelectric effect, especially how the piezoelectric bimorph bender works, etc. Reading this chapter helps the readers to know some terminologies, and to have a general understanding of the principles of implemented techniques.

The characterization part

To achieve 3D surface reconstructions, the actuator needs not only to take the cantilever chip to scan in the x-y plane, but also to follow the sample topography at every detecting point to reflect the depth information. The latter motion is normally referred to as the "z-axis actuation". With an uneven sample surface, the z actuator needs to be consecutively adjusted to conform to the sample surface. To accurately reflect the depth information, the cantilever chip should adjust its z coordinate as fast as possible. One of the influencing parameters in determining the scan speed is the actuator's dynamic properties, basically the resonance frequency. In order to obtain this information on the actuator in Nanite A and B, the Laser Doppler Vibrometer "MSA400" is utilized. Chapter 3 explains the working principle of the LDV, the conduction of the measurement (including the input signal, the setup and connection, as well as the measurement strategies), and the test result.

In the new Nanite generation, the actuation concept has been changed greatly. The significant difference is that no motion composition is involved any more, meaning that individual actuators are employed to accomplish the actuations along different axes. In this case, the analyses of the z axis actuation can be simply achieved by charactering the individual z actuator. By using a COMSOL simulation model, section 4.1 answers the question "How much Lorentz force can be generated with this z actuator?". In section 4.2, the relation between the maximum deflection and the power input is investigated to check the linearity of this actuator. In order to compare the dynamic response of this new z actuator with the previous version, section 4.3 describes the calculations of the first resonance frequency and the corresponding measurement assisted with the LDV. Besides, as heat dissipation is a critical factor for the MEMS structures, section 4.4 uses simulations and measurements to address questions like: "How does the temperature distribute along the flexprint? ", " Where does the maximum temperature appear?", " What is the highest temperature? ", "Whether does the size of the bonding pad influences the heat conduction?", etc.

The design and simulation part

Since the z actuator is to be attached on the x-y platform, the weight of this actuator should be light enough. With such consideration, piezo actuating concepts (on the basis of the ceramic bimorph bender) are thus conceived to replace the actuator mentioned in Chapter 4. In this initial trial, different configurations are considered and compared in section 5.1. In section 5.2, two potential concepts are selected and compared with each other from multiple aspects, including the resonance frequency, the actuating stroke, the mass, volume and cost. In chapter 5.3, the selected concept 'half actuator' is further studied with COMSOL simulations to explore the influencing parameters on the maximum deflection, such as the power input, the individual bender length, and the overlap. Eventually, real actuators are built up and measured, with the corresponding results and discussions demonstrated in section 5.4.

Additionally, one may find a literature review on the AFM actuators in Appendix A, which is accomplished ahead of this project. This study aims to obtain the insight of a particular study area - the AFM actuators. To know the state of art and the current problems we are facing now will be definitely beneficial for future researches. Section A.2 describes the actuating concepts that could be adopted in an AFM actuator, which are developed on the basis of either the piezoelectric effect or the electromagnetic effect. In weighing up whether an AFM actuator is good or not, some design criteria are listed out in section A.3, including the scan range, the scan speed, the resolution, and the actuation force. In section A.4, problems with different actuating concepts are illustrated, followed by the possible solutions.

Theoretical Background

2.1 The Configuration of AFM

The AFM is one of the two kinds of Scanning Probe Microscopes (SPM) used to form images of small objects, with their sizes ranging from hundreds of micrometers to the order of a few nanometers, sometimes even counted in angstroms. The alternative is referred to as Scanning Tunneling Microscope (STM), which is first developed in 1981 by Gerd Binnig and Heinrich Rohrer. The STM is built on the principle of the quantum tunneling effect that a small particle, like an electron, can penetrate a thin barrier under potential treatment and shown up on the other side of the barrier as depicted in Figure 2.1. In the real STM configuration, the probe and the sample are the media where the electrons can propagate, and the air gap in between amounts to the barrier. With potential application as depicted in Figure 2.2, the electrons from the probe can tunnel through the air gap to reach the sample domain. In the scanning process, the changes of the gap size will induce current differences, which will be utilized to reconstruct the surface structure. However, the major impedance of this device is that its applications are limited to the conductive samples only, as nonconductive surfaces are incapable of conducting electron streams.

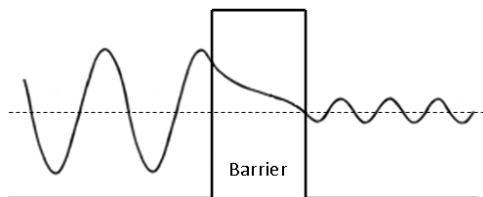


Figure 2. 1, the quantum tunneling effect

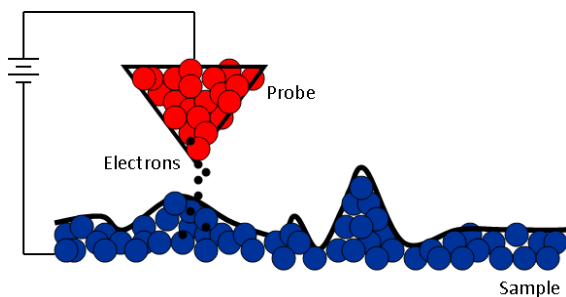


Figure 2. 2, tunneling effect used in STM between the probe and the sample

To resolve this problem, in 1986, Binnig, Quate, and Gerber invented the first AFM, also named as Scanning Force Microscope (SFM). Different from the STM, the AFM instrument is constructed on the basis of the interaction forces between the probe atoms (primary the one on the apex of the probe) and the atoms constituting the sample surface as shown in Figure 2.3. When the interactional atoms are far away from each other, the Van der Waals force plays a dominant role, and the net force appears to be attractive. By approaching the probe to the sample surface, this attractive force will go up until the electron clouds of two atoms start to overlap. When this happens, the Pauli repulsive force prevails, and increases dramatically with the reduction of the intermediate air

gap [5][6]. Such relation can be depicted as shown in Figure 2.4. Theoretically, when having the information of the interaction force, one could easily derive the relative distance between the probe and the sample, and based on this information, the surface structure of the test sample could be represented by special algorithm calculations.

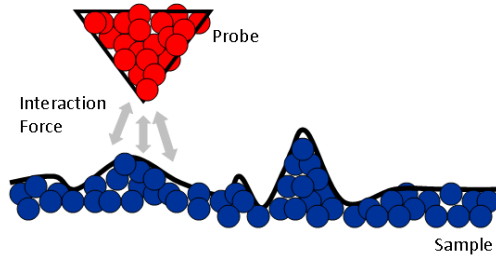


Figure 2. 3, the interaction force between the probe and the sample (the principle of the AFM)

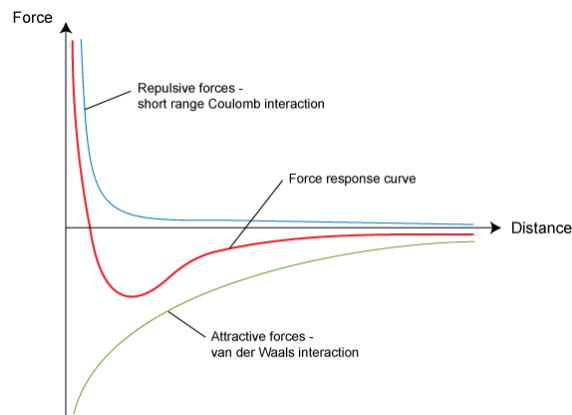


Figure 2. 4, the interaction force between the probe and the sample in the process of approaching one to the other [7]

In reality, the probe can not “float” in the air without any suspension structure as depicted in Figure 2.3, meaning that it should be in virtue of some external suspension structure to be able to hang over the sample surface for the purpose of force detection. To solve this problem, the probe is conceived to be integrated at the end of a free standing cantilever beam. This concept is proved to be quite efficient through the test of practice, and still commonly used in today’s commercial products. However, the design of this beam configuration is under quite stringent requirements, as its dynamic motion will directly influence the performance of the probe. Generally, the activation is operated in low frequency, it is therefore reasonable to design the (beam) resonance frequency as high as possible to avoid unexpected vibrations. This can be realized by giving the cantilever beam a proper mass and a suitable conformation. Considering all these requirements, the beam dimension is expected to be in the order of $300\mu\text{m} \times 80\mu\text{m} \times 1\mu\text{m}$ [8]. The achievement of this cantilever-probe structure depends heavily on the silicon fabrication techniques, including photolithography, different types of etching, etc. With an appropriate flow chart design, individual cantilever chips can be obtained as shown in Figure 2.5. Each chip contains not only the cantilever-probe structure, but also the electrical connections for the signal input and information readout. Such cantilever chip will be subsequently attached on the AFM actuator, which will be elaborated in section 2.3.

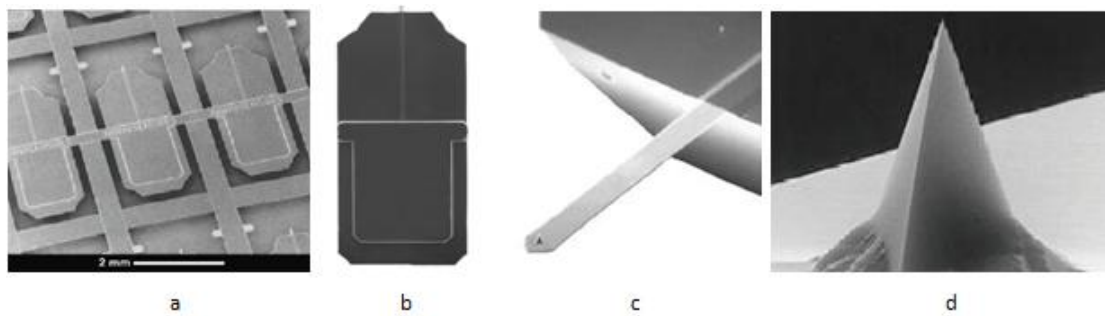


Figure 2. 5, a, the fabricated wafer with cantilever chips on; b, a single cantilever chip; c, magnified picture of the cantilever beam; d, the probe [8]

In practical applications, instead of directly detecting the interaction force, measuring either the cantilever deflection or its dynamic property (depending on different operating modes) is more commonly seen. To obtain this information, methods based on different principles have been developed. Of all these methods, the most convenient way is by focusing a fine laser beam on the backside of the cantilever probe as depicted in Figure 2.6. Normally, to increase the reflectivity, there will be a thin gold layer coated in a predefined area, and the reflected laser beam will irradiate at the plate of the photon detector. At an equilibrium point, that is the moment when no cantilever deflection occurs, the laser point will appear in the center of the plate. Whereas when the cantilever deforms due to the probe-sample interaction, the laser trace will change and result in a different focus point on the decoder plate. Given this causality and by the software calculation, the cantilever deflection and the corresponding interaction force can be derived.

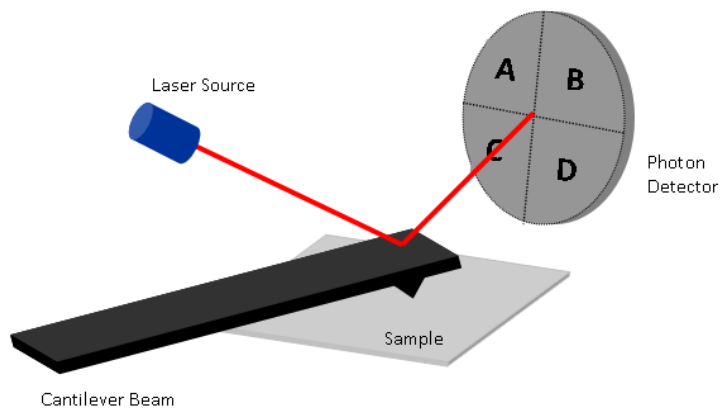


Figure 2. 6, light reflection based signal detection mechanism

Other than the method mentioned above, some other mechanisms are also employed. For example, embedding strain gauges in the cantilever chip can help to detect the beam deformation. Furthermore, by using a Wheatstone bridge, the detected signal will be preceeded and compensated for further image reconstruction. Another way to do this is by using the optical interference effect that a light beam is split into two paths first: one is the object beam that goes to the back side of the cantilever chip, and the other one is the "reference beam", which irradiates on a stationary object. The interference of the two reflected light beam will deliver the information of the beam deflection, and thus provides evidences for image formulation. Detailed information on different detecting techniques can be found in reference [5].

To form an image, there should be relative motions between the cantilever chip and the targeted sample. Only in this way can the interactions at different positions be detected, and processed to reconstruct the surface structure. Of course, for the high resolution purpose, it would be preferred if it is possible to measure the interactions at every single point. However, in reality, this is barely achievable as acquiring data at hundreds of

thousands of points requires high workload. Besides, the number of the measuring points is mostly determined by the resolution of the actuation system. Therefore, to obtain comparable comprehensive information of the surface structure, it is excusable to take measurements in a small sample area in the form of raster scan.

How to shift the position of the cantilever chip from one measuring point to the other? As the size of the cantilever chip is normally in the order of 5mmx3mm, it is difficult to operate with traditional mechanical structures. Therefore, to fulfill the actuation task, it is imperative to make use of the micro actuators. However, to manipulate the cantilever chip to move in a desired trajectory, as a basic requirement, the actuator should achieve at least 3 DOFs, because the actuator needs to accomplish the in-plane motion, recognized as x-y plane movements, and the out-plane motion, normally denoted as the z-axis adjustment. Different eligible actuator concepts are elaborated in section 2.3.

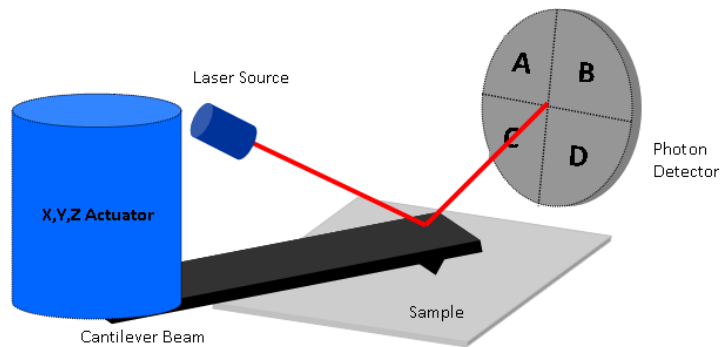


Figure 2. 7, probe scan

With proper configuration design, the cantilever chip can be attached at the end of the micro actuator as shown in Figure 2.7. Given the fact that the scan motion in this case is accomplished by the cantilever chip (with the sample standing still), it is therefore quite frequently referred to as “probe scan”. However, one major drawback of this scan mechanism is that the position of the laser beam needs to be changed all the time to catch up with the probe shift in order to supply the optical decoder timely gained topographical information. Such tracking process might easily induce unexpected deviations. To boost the system performance, in some modern AFM systems, the actuation is devised to be carried out by the sample stage as depicted in Figure 2.8. With such design, the coordinates of the cantilever chip can be maintained constant, and no laser shift is any more needed. As only sample movements are engaged in this process, the scan mechanism is normally mentioned as “sample scan” [9].

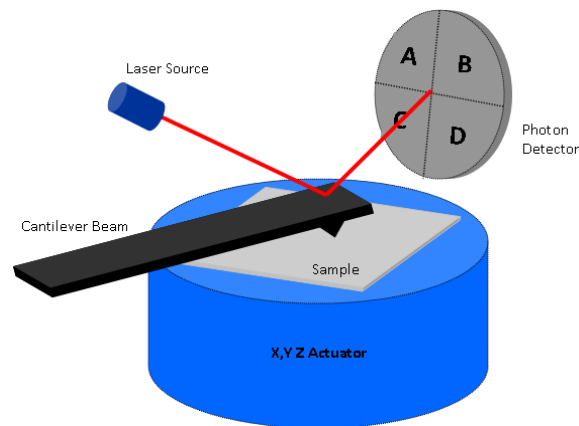


Figure 2. 8, sample scan

Yet, one may ask: even if the actuator can automatically take the cantilever chip to move in the x-y plane with electrical signal inputs, how should it know when to activate the z-axis actuation and how much should be adjusted

in accordance with the sample topography? In fact, here we missed one primary link --the signal processing unit which includes the amplifier, the PID controller, and some other relevant electrical components. In general, when the cantilever beam has relative deformation, the detected signal will be amplified first and then sent to the PID controller. With appropriate gain setting, the controller can generate a compensating signal, and feed it back to the micro actuator to compensate the initial deflection. At the same time, this signal will be transferred to the computer for the purpose of image reconstruction. So far, almost all the AFM constituents have been elaborated, which leads to the idea to properly connect them to form a functional system. As such, a schematic of the basic system configuration is depicted in Figure 2.9.

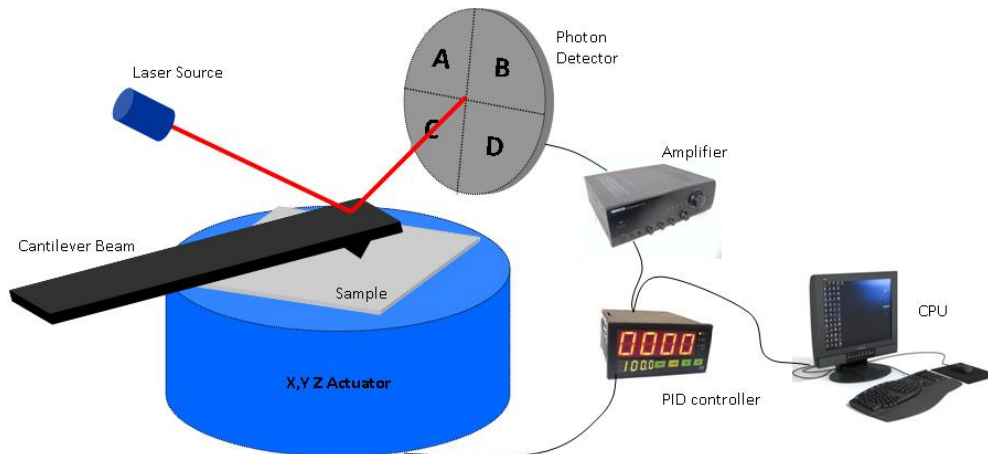


Figure 2. 9, the general configuration of an AFM

2.2 Operating Modes [10]

The interaction force, as have been emphasized in section 2.1, changes significantly in the approaching process, as a result, the beam motion will differ greatly as a function of distance. According to the motion of the cantilever beam and its operating region, the scanning process can be divided into different operating modes: contact mode, non-contact mode and intermittent mode.

In contact mode, the cantilever beam is dragged across the sample surface and maintained in the repulsive force dominated region. Concurrently, the beam deflection is detected and further applied to construct the surface contours. On most occasions, a static tip deflection as shown in Figure 2.10a is expected, meaning that the force between the probe and the sample should be adjusted to be constant. This can be achieved by back feeding the detected signal to maintain the sample-tip distance unchanged. Because of this reason, this operating mode is often referred to as static mode. Contact mode can generally provide the highest resolution among all the operating modes. However, because the tip will have direct contacts with the sample, it may induce damages on the sample, and even influence the sharpness of the tip.

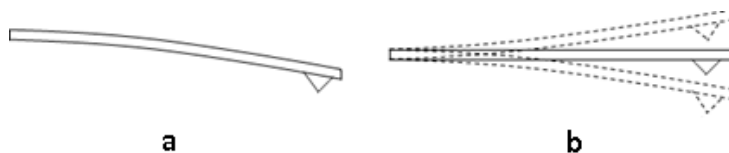


Figure 2. 10, a, the static operating mode; b, the dynamic operating mode

For non-contact mode and intermittent mode, the cantilever is externally excited (usually by a piece of piezo material) to oscillate at or close to its resonance frequency as shown in Figure 2.10 b. Instead of maintaining a constant deflection, the amplitude or phase of the cantilever's dynamic motion is detected and used as feedback signal. The difference between noncontact mode and intermittent mode is that the cantilever in the non-contact

mode oscillates only in the attractive-force dominated region. The amplitude of the oscillation is normally quite small, often of the order of 10nm. The advantage of this operating mode is that no damage can be induced since no contact is formed in this process. In contrast, the cantilever beam in the intermittent mode oscillates in larger amplitude, normally more than 100nm. That means the cantilever will be operated in both the attractive and repulsive region. As a result, the cantilever will touch the sample surface occasionally. Therefore, it is often referred to as tapping mode. Furthermore, based on the detecting parameter for feedback, the dynamic operating mode can be further grouped into two catalogues: the amplitude modulation mode (AM) and the frequency modulation mode (FM). In amplitude modulation mode, changes in the oscillation amplitude or phase provide the feedback signal for imaging. In amplitude modulation, changes in the phase of oscillation can be used to discriminate between different types of materials on the surface. While for the FM mode, changes in the oscillation frequency provide information about tip-sample interactions. Frequency can be measured with very high sensitivity and thus the frequency modulation mode allows for the use of very stiff cantilevers.

2.3 Actuators

As an indispensable part of an AFM system, the micro actuator plays a dominant role in improving the system performance. This small mechanical structure directly determines the quality of the to-be-formed image over different aspects, such as the scan range, the resolution and the scan speed. From the advent of the first AFM, tremendous efforts towards the actuation concept have been made to enhance the AFM performance. Different actuation structures have been conceived, developed and adapted in the AFM system. Initially, most actuators are built on the basis of the piezoelectric effect, and some of the actuation concepts, like the piezoelectric tube actuators, are still widely adopted in today's AFM products. In section 2.3.1, the piezoelectric effect is shortly described, followed by the demonstrations of different piezo concepts. However, as discussed in Appendices A.4, some disadvantages with piezo actuating are gradually exposed, such as the hysteresis, creep, vibration, and the aging problem. A pioneer company, Nanosurf, made groundbreaking progress on the AFM actuation by using the electromagnetic effect. Such application overcomes the drawbacks of the traditional way of actuating the cantilever chip. In section 2.3.2, the basic principle of the electromagnetic effect is concisely explained, associated with the introduction of different actuating concept used in Nanite Family, including the actuator in Nanite A and B, and the one used in the new Nanite generation. Additionally, more actuating concepts can be found in A2 Appendix A.

2.3.1 Piezoelectric actuators in AFM

2.3.1.1 Piezoelectric effect

The piezoelectric effect, first uncovered in 1880 by Jacques and Pierre Curie, has capitalized significant attention in the last few decades, and has been extensively utilized, especially in the area of mechanical engineering and bioengineering. The interpretation of piezoelectric effect includes two aspects: the direct piezoelectric effect and the inverse piezoelectric effect. The former one refers to the occasion when a piezoelectric material (neutral) is subject to mechanical stress, it will generate electric signals. This force-to-electricity transmission can be explained by the illustration shown in Figure 2.11. Without external impacts, all the atoms in the cubic lattice are symmetrically distributed, and this equilibrium state makes the lattice appear neutral. However, when tensile strength is applied on the piezo material, there will be a small deformation formed as shown in Figure 2.11 right. This deformation will result in a new atom-distribution pattern and electrify the lattice structure. It is worth noticing that tension and compression can produce polarities with different signs, and the intensity of the generated electric field is in proportion to the applied force. By such explanation, the converse of this relationship is also confirmed: if one of these voltage-generating lattices is exposed to an electric field, it will elongate or get shortened as effect of the polarity of the electric field, with its deflection proportional to the field strength [11].

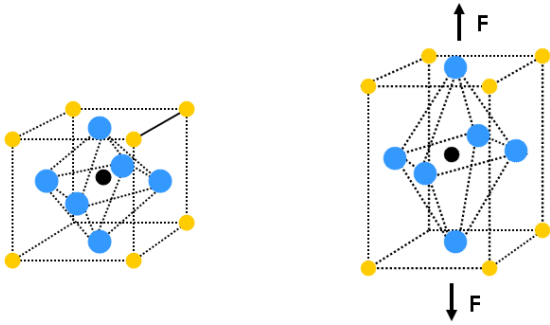


Figure 2. 11, the atom distributions in a piezoelectric cubic lattice: before force treatment (left) and after (right) force treatment.

2.3.1.2 Piezoelectric actuators

a) Tripod

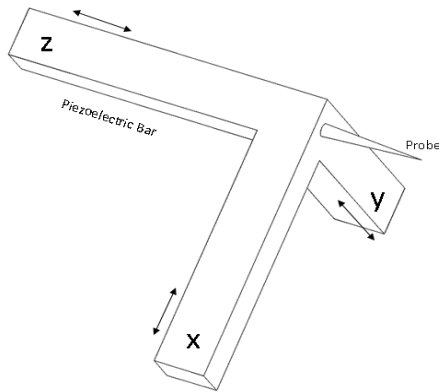


Figure 2. 12, the tripod actuator, constructed with three piezo bars perpendicular connected

The “tripod” actuator is one of the first few concepts that developed on the basis of the piezoelectric effect. The tripod structure is formed by perpendicularly connecting three cuboid piezoelectric bars together as shown in Figure 2.12. Each piezo bar accounts for the actuation along one direction, and the whole structure can therefore achieve 3 DOFs. On each bar, a thin metal layer is separately deposited on two opposite sides working as electrodes, and with power input, the bars will expand and contract to accomplish the corresponding motion. The probe (or the cantilever chip) will be installed at where the bars intersect to implement the scan motion. To estimate the deflections along different axes regarding to an input voltage V , a simple mathematical equation is derived and shown in the following equation.

$$\Delta x = d_{ij} V \frac{L}{h}$$

Where L and h are separately the length and thickness of the piezo bar, and d is the piezoelectric strain coefficient. However, a major problem for this design is that the piezo bars are quite flexible and easily influenced by vibrations, noises and thermal drifts, which could significantly impair the performance of AFM. Moreover, the cross-coupling effect, that the motion interactions between different axes, with this structure is also striking and may lead severe distortions to the scanning images.

b) Bimorph

Other than the tripod structure, “bimorph bender” is also frequently employed for actuations in different applications in order to achieve large scan range. In Figure 2.13, two mechanisms with almost the same configuration (both with two metalized bender plates) but different connections are illustrated. The benders in the

series bimorph (left) are joined with opposite polarizations, and there are only two connections stretched out for power input. While for the parallel bimorph on the right, the polarizations of the benders are positioned in the same direction. Besides, there are three interfaces for electrical connections: the two outer electrodes are generally grounded, while the central one is applied with an electrical potential. With such arrangement, one of the plates will expand, and the other one as given an opposite electric field will contract. Consequently, the achieved actuation force and scan range will be doubled. However, a drawback of the bimorph design is that it gives a few accesses to multi-dimension actuations, because one bender can only achieve 1 DOF. Even if it is possible with combinations, the configuration will be either too complicated for fabrication or too susceptible to external disturbances, which might to be addressed by massive and intricate control algorithms.

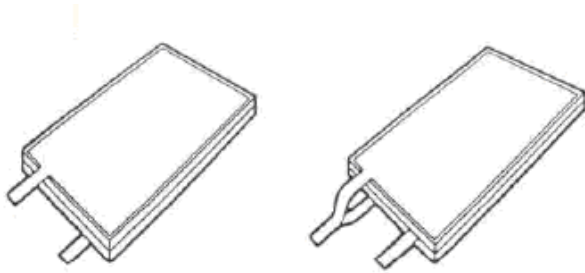


Figure 2. 13, bimorph actuator: left) the series bimorph; right) the parallel bimorph [12]

c) Tube

The emergence of the piezoelectric tube actuator made a breakthrough in boosting the AFM performance. With high accuracy and fast reaction rate, this actuator is extensively used in some of today's AFM systems for various applications. The configuration takes the form of what demonstrated in Figure 2.14 a. The achievement of this configuration is by first fabricating a tubular shaped piezoelectric structure (radially polarized), normally with a thickness of $7\ \mu\text{m}$ to $9\ \mu\text{m}$ [1]. Separately on its internal and external wall deposits a thin metal layer (either in silver or copper) serving as an electrode. The internal wall is covered by an entire metal piece, recognized the z electrode, and the coated external electrode is symmetrically segmented into four quadrants, separately denoted as +x, -x, +y, -y.

With one of the ends fixed, the tube actuator could commit its motion with the other end in all three dimensions. As can be observed from Figure 2.14 b and c, the x- and y-axis actuation is achieved by structure bending, while the z-axis actuation is completed by structure expanding and contracting. In the process of the x- and y-axis actuation, the trajectory of the flexible tube end should be a curve in theory, resulting in a deflection projection along the z axis. Nonetheless, as the motion is quite small, this coupling effect can be ignored, although still generating negative effect on the image formation. For the power input, the actuation along the x (or the y) axis is achieved by applying voltages on the x-x (or the y-y) electrode pair, leaving the inner electrode grounded. Yet, for the z axis actuation, it is often accomplished by giving an electrical potential to the z electrode, with one of the other terminals grounded.

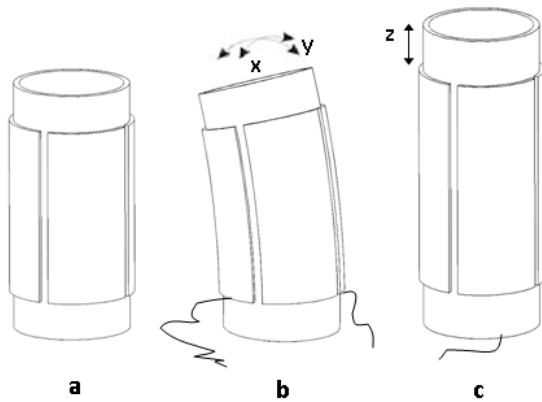


Figure 2. 14, the piezoelectric tube actuator

2.3.2 Electromagnetic actuators in AFM

2.3.2.1 Lorentz Force

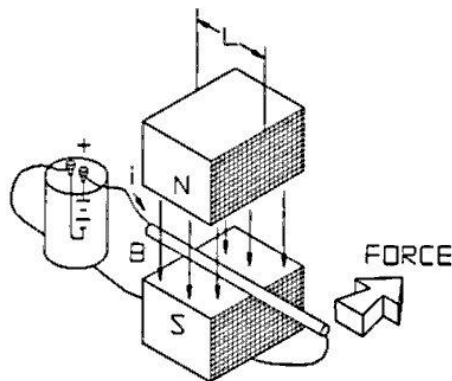


Figure 2. 15, the basic principle of an electromagnetic actuator [13]

Another important actuating category is the electromagnetic actuator, which is developed on the basis of the electromagnetic interactions. Mostly, the implement of the actuation relies on the Laplace-Lorentz force (a force generated on a mobile current-driven coil when placing it in a static magnetic field). This force is proportional to the applied current, and thus controllable in practical applications. Since this actuator is first developed for the usage of the loud-speaker, it is also referred to as “voice-coil actuator”. To explicitly indicate the working principle, a schematic drawing is shown in Figure 2.15, where two pieces of permanent magnets are applied and positioned above and below a thin coil. Given the magnetic flux and the direction of the current, the generated Lorentz force can be inferred as marked in Figure 2.15. By fixing either the magnets or the coil, the other part will move relatively.

2.3.2.2 Actuator in Nanite A and Nanite B

It can be easily discovered that the actuation structure in Figure 2.15 can only achieve 1DOF, whereas for probe actuation in an AFM, all three transitional DOFs are needed. To meet this challenge, Nanosurf pioneered the idea of using three electromagnetic actuators to compose the scanning motions of the cantilever chip. By orientating and appropriately arranging the individual actuators, an effective actuating system was achieved as demonstrated in Figure 2.16. As can be observed from the configuration of this driving mechanism, three coils are rigidly connected to a substrate (not shown) in a triangular form, while the magnet pieces are attached to a flexible spring-suspended platform and hanged right above the coils. The cantilever chip will be installed on the edge of

the flexible platform and positioned almost perpendicularly. Although each actuator can only achieve 1 DOF -- the vertical motion in this case, by activating (or partially activating) one or several of the three magnet-coil combinations, a composed motion can be formed and transferred through the platform to the cantilever chip. The applied suspension structures are responsible for providing restoring forces to balance the generated electromagnetic strengths to achieve reliable actuations [14] [15].

Theoretically, the electromagnetic actuators can be oriented, meaning that the magnets can be fixed underneath to the outside world. Accordingly the coils will be attached to the top platform. However, such configuration is failed to be adopted because supplying current to the coil will charge the platform at the same time, which will influence the performance of the cantilever chip.

Despite that the design (in Figure 2.16) can effectively achieve the desired actuation, there are still some drawbacks. One major issue is that the concept of the motion composition limits the resonance frequency along the cantilever's z axis. This is because the motions of the three actuators are mutually dependent since they are rigidly connected to a same platform; the movement of an individual actuator will lead associated movements to the rest two. Another problem of this design is that the mass the moving parts (magnet + platform) is comparably large, which will again reduce the resonance frequency of the whole structure.

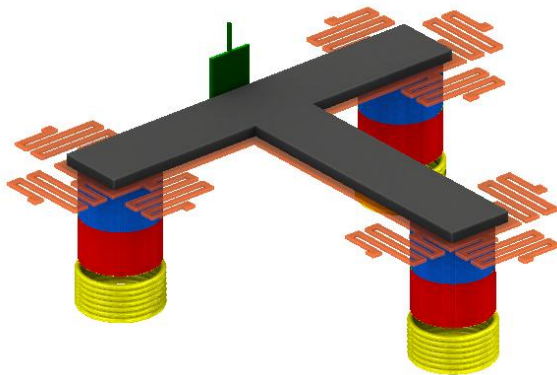


Figure 2. 16, the actuation concept used in Nanite A and B

2.3.2.3 Actuator in the new Nanite generation

In developing the new Nanite generation, Nanosurf dropped the old actuation concept, and originated a different actuating mechanism. In the new configuration, no motion composition is any more needed. Instead, Individual actuators are employed to independently accomplish the actuations along different axes. This not only successfully eliminates the drawbacks of the previous concept, but also increases the design flexibility. In order to achieve a low actuating mass in this design, the coils are altered as the carrier to take the cantilever chip to move. Correspondingly, the magnets will be fixed in order to generate a stable magnetic environment. As one can imagine, metal platforms are not suitable in this case for the coil fixation since they are quite conductive and easily get charged. As a result, polymer materials are considered as they are less conductive which can effectively eliminate current circulations in the platform, and furthermore they can reduce the mass of the moving body. In the following section, the actuation concept is decomposed and discussed with respect to different axes.

a) Lateral actuation

In Figure 2.17, an illustration portrays how the magnet-coil-magnet combination generates lateral forces for the in plane motion, that is the x and y-axis actuation. It can be observed that two pairs of magnets are exploited and placed right above and below the long edges of the annular coil. In each magnet pair which contains two vertically positioned magnets, the magnetizations (the magnetic dipole moments in a magnetic material) of individual magnetic blocks are oriented in the same direction such that the induced magnetic field is longitudinal.

Considering the direction of the current, the two magnet pairs at different edges are positioned with their magnetizations opposite to each other, such that the generated Lorentz force will point to the same (lateral) direction. Eventually, the magnets will be attached to a top and bottom plate for fixation and the coil will be further fabricated in the polymer material for the chip installation and driving.

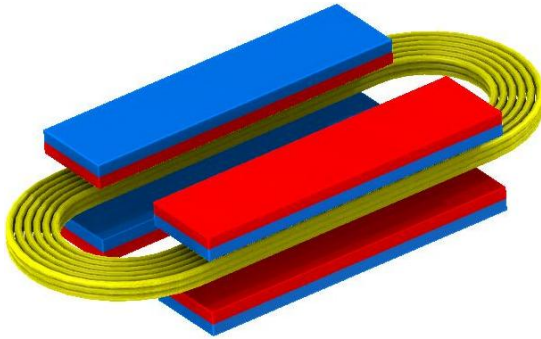


Figure 2. 17, the actuator for x- and y- axis actuating

b) Vertical actuation

To realize the driving force along the vertical direction, namely the z axis, the design of the z actuator is slightly changed on the basis of the configuration in Figure 2.17. The original concept is demonstrated in Figure 2.18. As can be observed, three pairs of magnets are employed, and within each pair, the magnetizations of the two magnetic blocks are arranged in opposite directions. This arrangement aims to achieve horizontally oriented magnetic fields in the cross areas of the horizontal and vertical air gaps. Another significant change is the layout of the coil. Instead of being placed in the interspace of each magnetic pair, the coil is shifted horizontally to the air gap where the horizontal field intensity is the strongest. In this case, the generated Lorentz force will be vertical. Again, the magnets will be rigidly attached to the outside to ensure of a stable field. Given the fact that the curved part of the coil is not into usage, a better concept is conceived to optimize the actuation structure. In the new concept, circular shaped coils and magnets are adopted and disposed as shown in Figure 2.19. One of the advantages of this design compared to the previous concept is that, to achieve the same actuation force, the mass of the adopted coil will be smaller since all the edges are in use, which helps to broaden the operational frequency bandwidth.

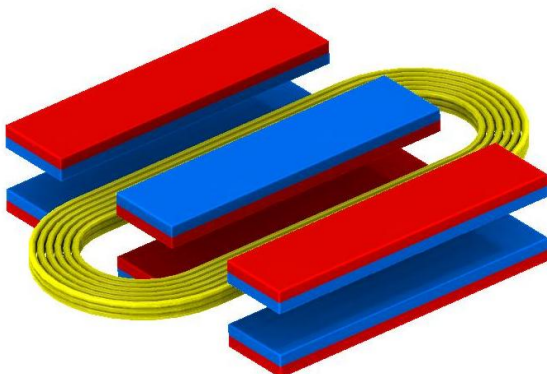


Figure 2. 18, the vertical actuation concept

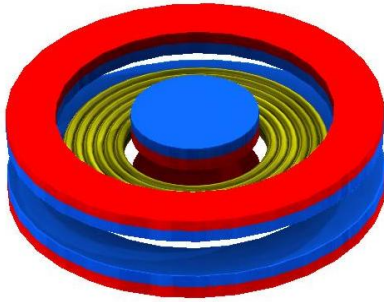


Figure 2. 19, the actuation concept for z axis actuating

c) The whole actuation concept

By understanding the actuation principles along individual axes, a compositional concept which is capable of 3-DOF scanning can be thus formed and is demonstrated in Figure 2.20. In this configuration, the actuation coils are fabricated in a piece of polyimide material, which is employed as a flexible platform to install the cantilever chip and take it to move. In correspondence with the coil arrangement, pairs of bar magnets are orthogonally disposed on both sides of the flexprint to realize the in-plane motion, namely the x- and y-axis actuation, and for the out of plane motion, a pair of circular magnet is displaced at the end of the flexprint ramification as depicted in Figure 2.20. Additionally, to balance the generated electromagnetic force, the flexprint is devised to be connected to the outside world with spring hinges which provides the reacting force in the process of actuating.

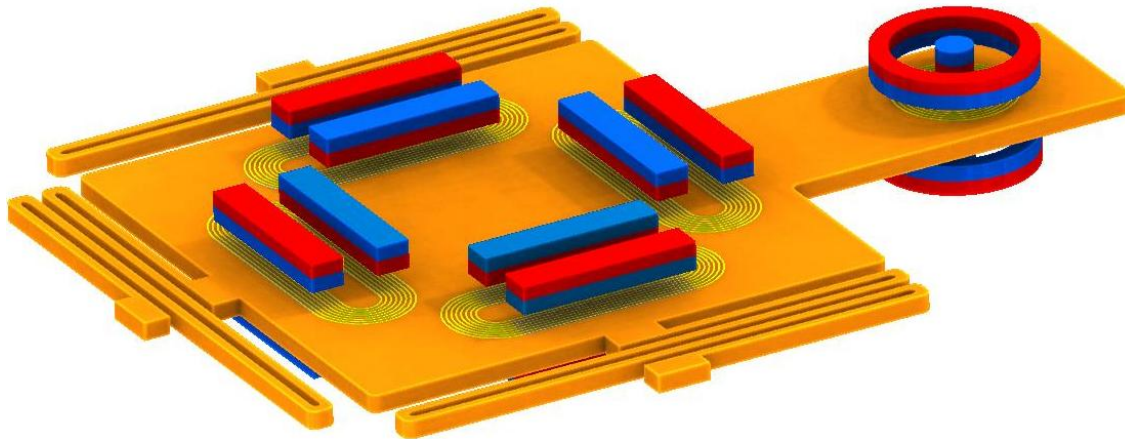


Figure 2. 20, the compositional concept of 3D scanning

Characterization of the Dynamics of the Actuator in Nanite A and Nanite B

As both Nanite A and B employ the “probe scan” method (a scan principle elaborated in section 2.1), the adopted electromagnetic actuators should cooperatively work to accomplish the cantilever chip's 3D scanning. This makes the reconstructed scanning image lean heavily on the actuator's performance, including the scan speed, the achievable resolution and the reliability. Yet, as indicated in reference [4], most of these criteria are directly or indirectly determined, or at least influenced by the dynamics of an actuator, especially the distribution of its first resonance frequency.

Considering the configuration of the actuator and the information of interest to know, only the characterization of the z-axis actuation resonance frequency is involved in this chapter. The reason is: In the scanning process, the cantilever chip should not only accomplish the raster scan form in the x-y plane, namely the plane where the sample locates; in order to provide the depth information, it should be capable of moving perpendicular to the sample surface. Therefore, in order to deliver reliable and high-quality images, the z-axis actuation should respond as fast as possible to catch up the x, y coordinate shift. This means a high scan speed is needed. In this sense, it is vital to be aware of impacts of the actuation resonance frequency along the z axis in developing a fast scan system.

How to measure this actuation resonance frequency, what device to use, how to make the right connections and how much the characterized value is, are the major problems to be solved in this chapter. Of course, for simple mechanical structures, it is possible to obtain the theoretical resonance frequency by simple mathematical calculations. Whereas how to deal with real objects with complex mechanisms becomes an intractable issue. To achieve this task, a sophisticated device, Laser Doppler Vibrometer (LDV), is utilized. By using superior techniques, this device is capable of measuring both the in-plane and out-of-plane motions of a micro object and is able to intuitively deliver the test results in terms of Bode plots, or Nyquist plots. Section 3.1 describes the working principle of this device. In section 3.2, the measurement setup and strategy are demonstrated, followed by the results and discussions in section 3.3.

3.1 Principle of Laser Doppler Vibrometer

3.1.1 Out-of-plane motion detection

The Laser Doppler Vibrometer uses the Doppler Effect for non-contact out-of-plane optical vibration measurement, and it detects how light shifts its frequency after being scattered from a moving object. In other word, the feature of the backscattered light reveals the dynamic motions of an object.

How does it work exactly? Within the LDV, a high precision interferometer is employed as a critical element to accomplish the signal processing and detecting processes. For better comprehension, a schematic of its working principle is illustrated in Figure 3.1, where initially the incident laser beam is split by the beam splitter 1 into two beams: one works as a reference beam, being reflected at the prism, and eventually reaching the beam splitter 3;

Synchronously, the other beam, referred to as object beam, travels through the beam splitter 2 and projects itself on the test object. Depending on the velocity and displacement of the object, the backscattered light will be modulated in terms of frequency and phase. Following that, the reflected beam is successively scattered at the splitter 2 and 3, and supposes with the reference beam to create an interference pattern. Eventually, this frequency pattern will get demodulated by the signal processor and analyzer to reveal the object's dynamic information. Considering the situation that the object movements towards the laser source generate the same interference pattern as the object movements away from the laser source, a Bragg Cell is utilized in the reference beam to shift the light frequency, such that the sign of the velocity can be determined: If the object moves towards the laser source, the modulation frequency is lower than the Bragg Cell shift frequency, and if it moves away from the laser source, the detector receives a frequency higher than the Bragg Cell shift frequency [16].

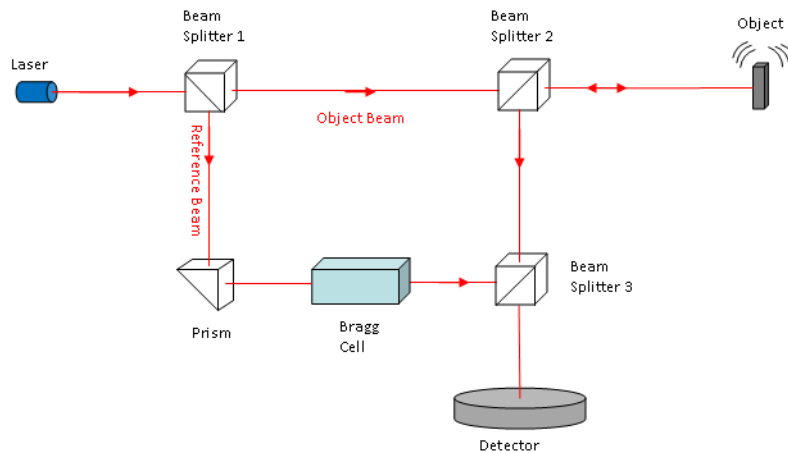


Figure 3. 1, the general working principle of a laser vibrometer

How to identify the relation of the object's velocity (displacement) and the frequency (phase) shift between the reference and object beam? The key technique here is the Doppler Effect. To appropriately express this relation, it is vital to separate the whole light reflection process into two parts. The first part is the light incoming process (before reflection happens). Assuming that the laser source emits electromagnetic wave with the frequency f , and the object moves at a velocity v . Based on the Doppler effect, one can express the object received frequency f' as a function of f and v . And the second part starts from the point when the light leaves the object. During this process, the object is regarded as a frequency source, moving at a speed of v towards the laser source, which is now considered as a receiver [17]. Again, It is easy to derive the relation between v , f' and f'' . Combining the two equations, the frequency shift can be expressed as follows:

$$\Delta f = \frac{2v}{\lambda}$$

This Doppler frequency shift will be transformed to a voltage signal first and then demodulated with the decoder. On the other hand, a moving object in a time interval will create a certain displacement, which will result in a phase difference between the object beam and the reference beam. Based on mathematical calculations, the phase shift can be written as:

$$\Delta\phi = \frac{2\pi\Delta x}{\lambda}$$

Where Δx is the path difference between the object and reference beam. By counting the bright-dark fringes with special techniques, the analyzer can demodulate the phase shift information to the amplitude of the object's deflection.

Through the two equations above, one may easily observe that the frequency (phase) shift is only related to the

velocity (displacement) of the moving object and the wavelength of the laser beam. These two equations are the mathematical explanations of how the out-of-plane dynamic motions are modulated into a backscattered wave.

3.1.2 In-plane motion detection

To use the out-of-plane measurement to characterize the dynamic motions of an object along a specific axis, it is important to ensure the laser beam is parallel to the measuring axis and at the same time perpendicular to the other two. For example, if one wants to measure motions along x axis using the out-of-plane measurement, the laser beam should shoot perpendicular to the y and z axis. As such, it is inevitable to change orientations of the test structure to execute all three axes dynamic analyses, which will definitely increase the workload of the measurements.

With this situation, a new approach -- the in-plan motion analysis -- is invented to avoid the orientation readjustments. Instead of using laser source to implement the Doppler Effect, the planar motion analyzer uses a video stroboscope to precisely record states of the micro component at different phases of the movement. Afterwards, one can define a structure pattern within the obtained visual impression of the movement, and the software will automatically trace the movements of this structure. Simultaneously, the analyzer will gain the displacement information of this structure at every moment, and proceed it to the corresponding dynamic response.

3. 2 Measurement Setup

3.2.1 Test sample

An unsealed Nanite B scan head is demonstrated in Figure 3.2. On the left side of the structure surface, three electromagnetic actuators (marked with A, B and C) are arranged at the endpoints of the three ramifications to comprise a complete actuation system. Although each actuator is only with 1 DOF (out of plane motion), the combined structure is capable of composing motions and driving the cantilever chip scan along its x, y and z axis (defined in Figure 3.2). This actuation system is our targeted sample.

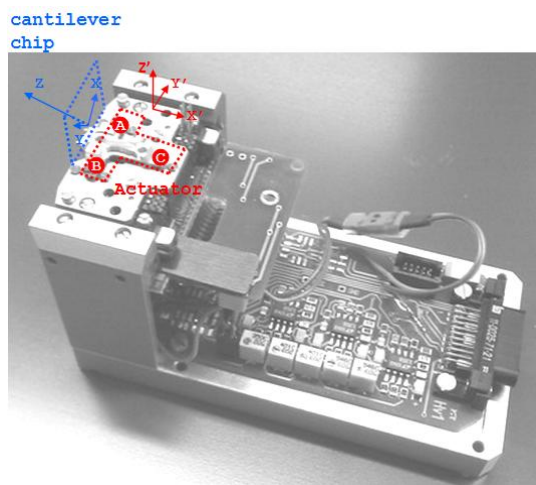


Figure 3. 2, the test sample, marked with the actuator's coordinate system and the cantilever chip's coordinate system.

However, there is one thing to be explicitly indicated: the coordinate system of the cantilever chip is not equivalent to that of the actuation system, because, as expressed in Figure 3.2, the planes where the two objects are lying are perpendicular to each other. Therefore, to clearly distinguish the actuator's coordinate system, hereby we set it as x' , y' and z' .

3.2.2 Input signal

Since the measurement aims at testing the actuation resonance frequency, the actuator ought to be working at every different frequency or some of the frequencies at least, as to construct a comparable complete frequency spectrum. This therefore asks for a frequency changing signal. In reality, there are different signals applicable for this case, such as the pseudo random excitation signal, the sine sweep signal and the periodic chirp signal. In this measurement, the pseudo random excitation signal is chosen to fulfill the actuation task, with its frequency altering from 1 to 500Hz.

3.2.3 Measurement setup

In a general Nanite A and B system, the signal detecting and processing mechanism can be simplified as shown in Figure 3.3. At different scan positions, the interactions between the probe and sample surface could be different. Depending on different operating modes, these variations could be embodied by either the deflections of the cantilever beam or its dynamic motions. Such signal will be sensed by some detection systems, and further compared with a predefined setoff value. This difference will be processed in the PID controller, and compensated by the actuator to maintain the cantilever beam at a constant state.

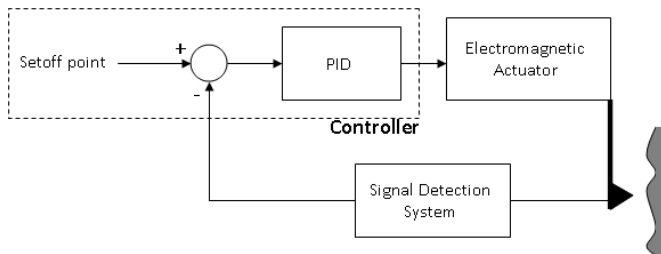


Figure 3. 3, the signal processing mechanism used in a general Nanite system

Based on the sample introduced in section 3.1.2.1, and for the purpose of inputting the frequency varying signal, the measuring mechanism is developed as given in Figure 3.4. According to what indicated in the Nanite B Manual, the input signal through the breakout box channel will be compensated by the PID controller, which is similar to how the detected signal is processed in a real AFM system. Therefore, the frequency changing signal from the internal function generator is given through the breakout box to examine the performance of the actuator.

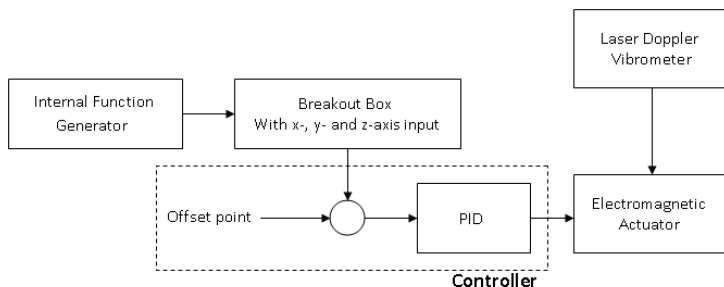


Figure 3. 4, the measuring mechanism with the frequency changing signal

For the laser Doppler Vibrometer, the MSA-400 MICRO SYSTEM ANALYSER system (developed by Polytec) is utilized to meet the challenge. The whole measurement setup is demonstrated in Figure 3.5, where the actuation system is disposed connected through the controller to the BNC breakout box (shown in Figure 3.6). As this box is a part of the Nanite B system, its input ports “x axis”, “y axis” and “z axis” naturally target the scan motions of the cantilever chip, rather than the motions of the actuators. To be more specific, if one applies voltage to the “x axis” port through the breakout box, the cantilever chip will scan along its x axis, while as the electromagnetic actuators can be only driven up and down, only one or several of them would probably be activated or partially activated to compose the cantilever’s x-axis motion.

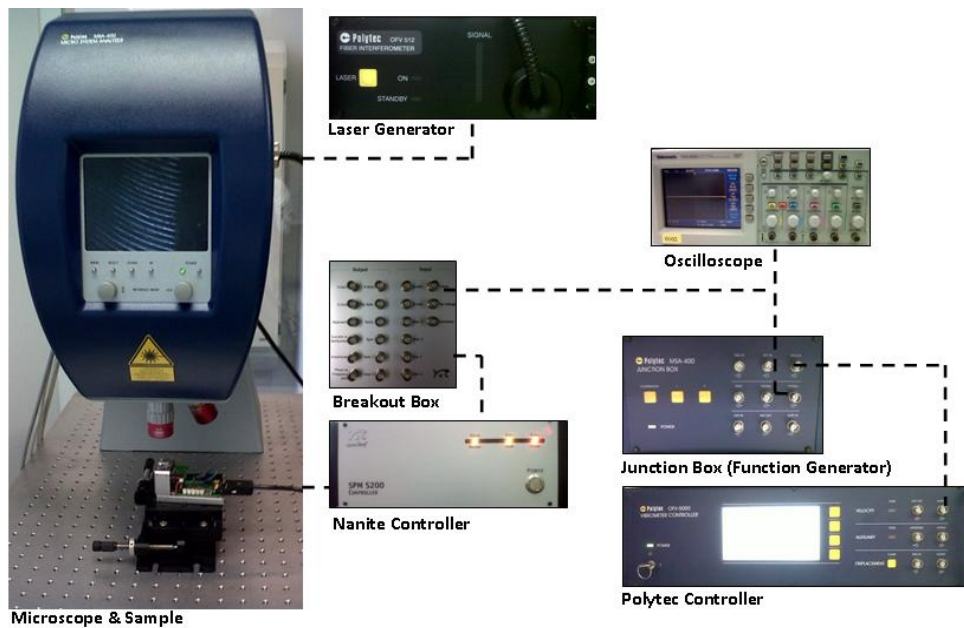


Figure 3. 5, the configuration of the measurement setup

According to the product brochure, the maximum input for each axis is ± 10 V. Thanks to the internal function generator, which is initially assembled inside the junction box (a part of the MSA-400 micro system analyser), and is capable of generating a desired sine sweep signal with the maximum amplitude of 10V at the offset of 0V, there is no necessary to draw supports from external function generators for the power issue. In the end, the cable used to join the internal function generator and the BNC breakout box is branched out and connected to an oscilloscope to timely display the frequency changing signal.



Figure 3. 6, the BNC breakout box from Nanite B

3.2.4 Measuring strategies

a) Measurement along the z' axis

Because the motions of the three actuators are the basic elements to compose the probe's z axis motion, before measuring the actuation resonances along the z axis, we would like to know the resonance frequencies of the electromagnetic actuators along their axial directions. Since the actuators are designed with only 1 DOF -- the translational DOF along the z' axis, the sample should be positioned as shown in Figure 3.7 left), such that the laser could radiate perpendicular to the x' - y' plane.

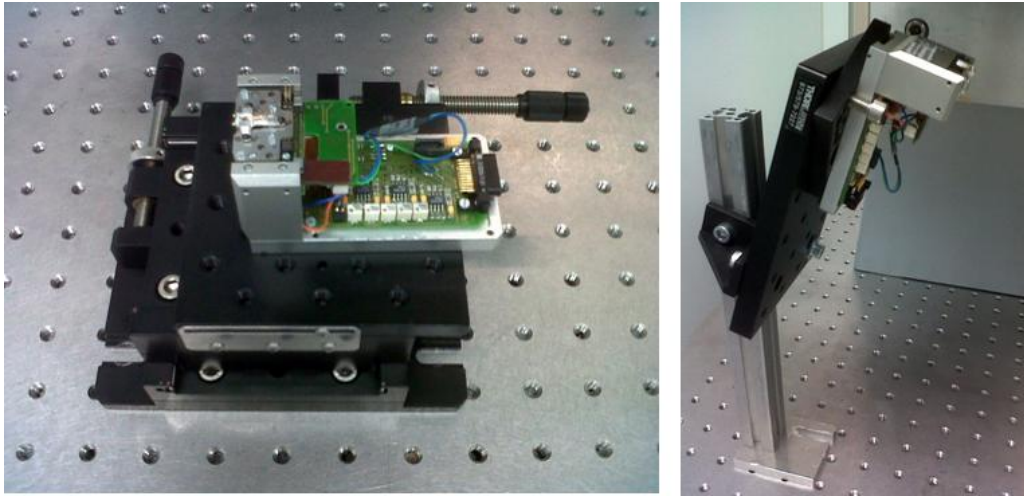


Figure 3. 7, the orientations of the sample: left) for measurement along the z' axis, right) for measurement along the cantilever chip's z axis

To examine how the actuator A, B, and C perform with respect to different inputs, the power supply from the internal function generator is successively given to the “ z axis”, “ x axis” and “ y axis” ports. To ensure the reliability of the results, measurements are done on different areas of the sample surface with almost the same initial conditions. For this particular case, measurement points are chosen at the surface of the actuator A, B and C, and the reason for such choice relies on the fact that the measurement results can not only reveal the actuators’ dynamic motions, but also provide information of how each actuator contributes to the probe’s motion.

b) Measurement along the z axis

In order to measure the actuation resonance frequency along the cantilever chip’s z axis, the sample is tilted approximately 90 degrees in reference to the sample position in previous case. Adjustments as such aim to make the laser beam reflect perpendicularly to where the cantilever chip is mounted. The oriented sample is shown in Figure 3.7 right). Again, three random positions are chosen to ensure the reliability of the measurement results.

3.3 Result and Discussion

3.3.1 Measurements along the z' axis

3.3.1.1 With “ z axis” input

With an input of 8V through the “ z axis” port, the measurement results pertaining to the displacement and the velocity are obtained and separately shown in Figure 3.8 and Figure 3.9. In each plot, three curves are contained, representing the performance of the actuator A, B and C. It can be observed from both of the plots that the resonance peaks of all the three actuators appear at one explicit frequency, 205Hz. Ahead of this frequency, the displacement responses reveal to be almost horizontal, indicating the actuators give stable amplitudes in the low frequency domain. In contrast, with the increase of the frequency, the velocity responses as shown in Figure 3.9 climb almost linearly to the resonance peaks.

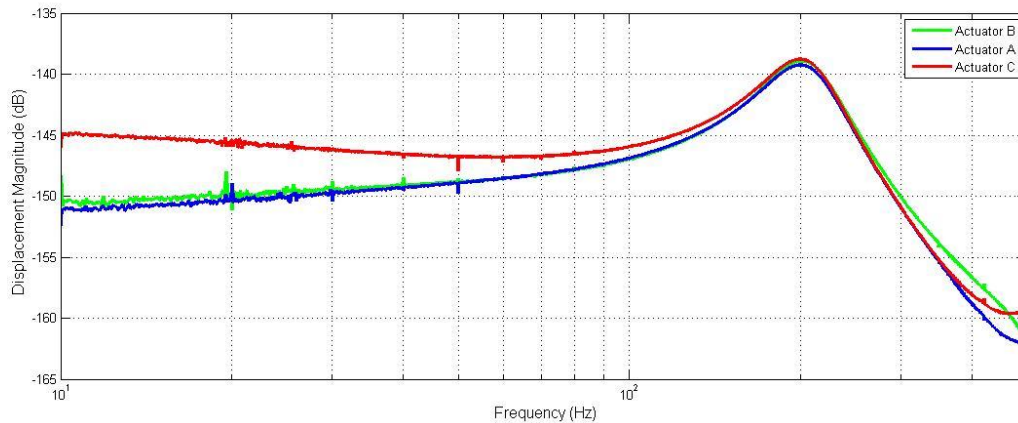


Figure 3. 8, the displacement response of the actuator A, B, and C with 8V z-axis input

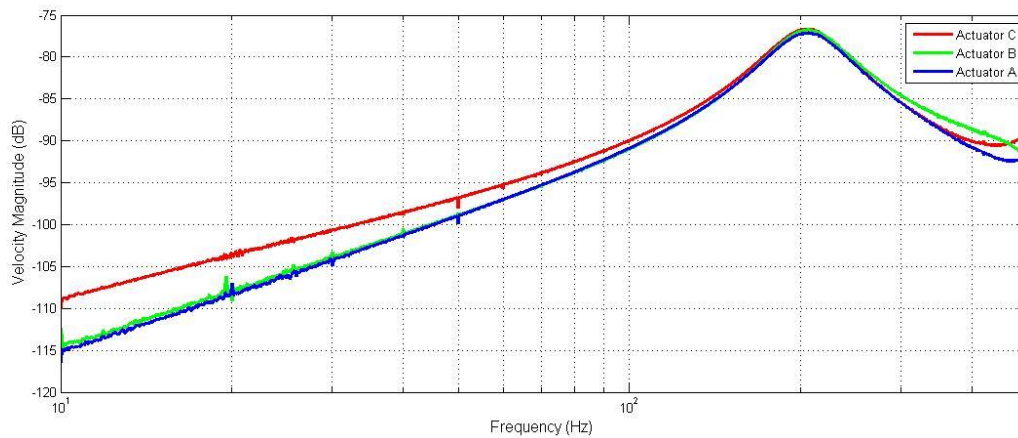


Figure 3. 9, the velocity response of the actuator A, B, and C with 8V z-axis input

Such phenomena can be accounted for as follows: since the displacement response reveals the deflection amplitude in terms of frequency and the velocity response gives the corresponding maximum velocity, the relation in between can be mathematically described as:

$$A \cdot 2\pi f = v$$

Where A stands for the amplitude of the deflection, v is the maximum velocity and f refers to the corresponding frequency. Revealed by the formula, if the deflection is maintained at a constant level within a domain where the frequency linearly increases, the velocity response should appear to be ascending as a result.

With careful observations, one may also discover that, before the appearances of the resonance peaks, actuator C, in comparison with the other two actuators, gives a higher performance in both the displacement and the velocity response. Furthermore, the extents to which the actuator A and B are activated are almost identical, meaning that these two actuators are synchronized in cantilever's z-axis actuation process. In eliminating the occasionality and coincidence of drawing such conclusions, another experiment with 3V input through the "z axis" port is conducted. The corresponding result is shown in Figure 3.10.

Compare Figure 3.8 and Figure 3.10: except for the magnitude difference, the two dynamic responses show almost the same trend. Therefore, for the z-axis actuation, the performance relation can be concluded as C>A≈B. Furthermore, according to the electrical driving circuit given in Figure B1 Appendix B and by simply following the

“V-Z” input, one could enclose that all the three actuators are activated during the z-axis actuation. Why the performance is different relies on the fact that the adopted resistances in different branches differ from each other, and these resistances directly control the extent to which the signals are amplified and thus determine the corresponding deflections. For example, the fact that the actuator A and B are synchronized is because their signals pass through the circuit branches with the same initial impedance of $68k\ \Omega$. This impedance is higher than $39k\ \Omega$ - the impedance placed in the other circuit branch where the signal for the actuator C will go through. It therefore results in a higher deflection on actuator C, which corresponds with our measurement results.

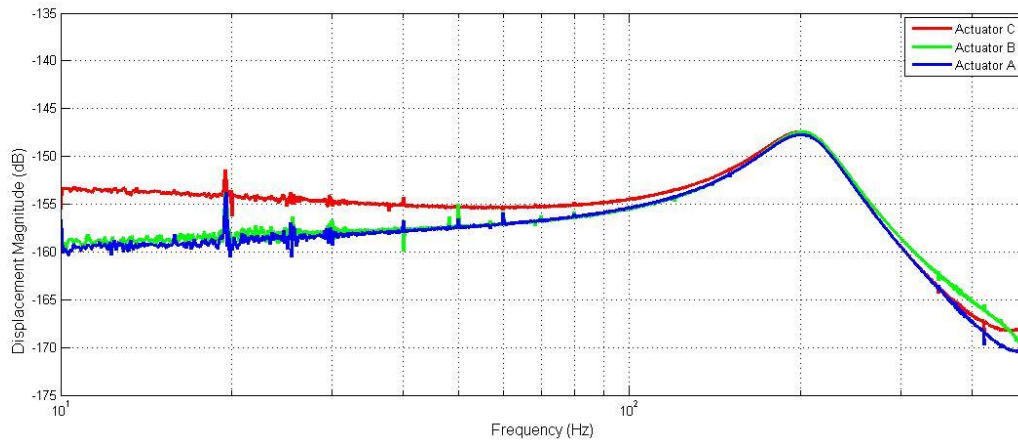


Figure 3.10, the displacement response of the actuator A, B, and C with 3V z-axis input

As can be observed in Figure 3.4, beside the input signal, there is an offset value predefined through the Nanite software on the controller. To check whether this unknown value generates any influence on the actuator performance, experiments without input signal and without the controller are separately executed, with the measuring mechanism shown in Figure 3.11 and 3.12. It can be easily discovered that the diagram in Figure 3.11 measures the impact of the offset point, and the purpose of designing of the mechanism in Figure 3.12 is in fact to measure the influences from the environment.

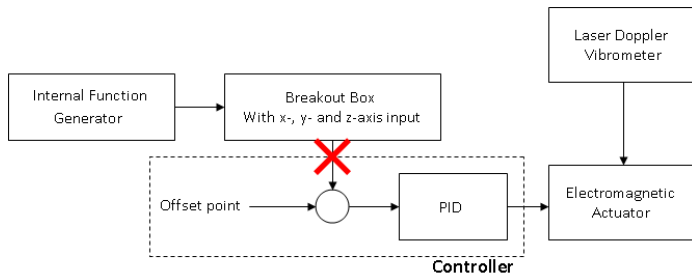


Figure 3.11, measuring mechanism without input

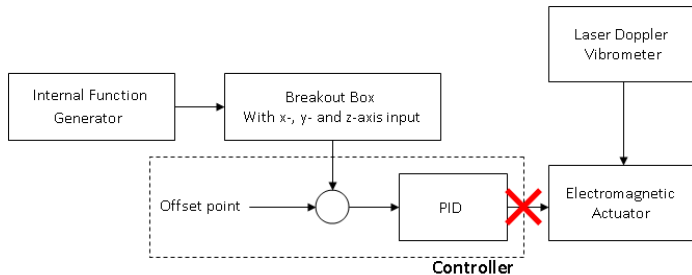


Figure 3.12, measuring mechanism without controller

The results together with the previous measurement are shown and compared in Figure 3.13. The result corresponding to the measurement without input signal shapes almost the same as the result measured without the controller, both more than 35 dB away from the red curve (measured with all elements). This indicates the offset point barely has any impact on the previous measurements.

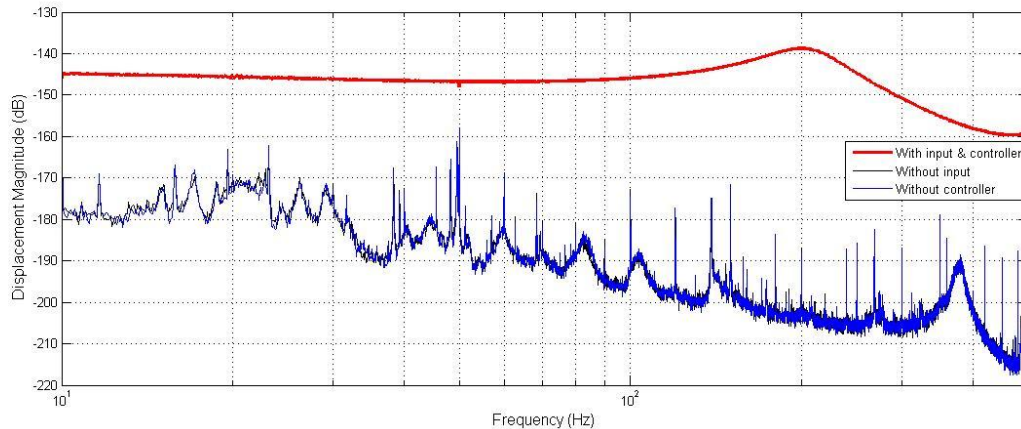


Figure 3.13, measurement with and without input/ controller

3.3.1.2 With “x axis” and “y axis” input

With the same methodology, measurements with “x axis” and “y axis” inputs are separately done at the locations of the three actuators. To interpret how the electromagnetic actuators contribute to the probe’s x- and y-axis motion, the respective displacement responses are shown in Figure 3.14 and Figure 3.15.

a) For the “x axis” input, the performance relation among the three actuators can be expressed as $B > C > A$, and $A > C > B$ for the situation with “y axis” input, meaning that at least two actuators are in motion in the process of x- and y-axis actuation. However, it is worth noticing that the actuator A in x-axis actuation performs different from the other two, as no stable deflections can be found in its low frequency domain, same situation for the actuator B in the y-axis actuation. This can be explained by the driving circuit provided in Appendix B, where one could easily find the actuator A is inactive in the branch marked with “V_X”, and the actuator B is inactive in the “V_Y” branch. The account for the detected deflections is probably due to the coupling effect that actuations of two actuators will induce deflections on the third one since they are rigidly connected on one platform.

b) Compare the magnitudes in the two Figures; one would notice that the corresponding values are almost the same. In other words, if we superpose the two figures, the curves would overlap, which proves the actuation along x- and y-axis are symmetric. This can be again verified by the electric circuit.

c) Regardless of the input port (whether it is “x axis” or “y axis”) and where the measurement is taken (whether it is at point A, B or C), all the resonance peaks all appear at around 205Hz, which from another perspective, proves that the ratios of the actuators’ stiffness to their masses are almost the same. This conclusion is drawn on the basis of the discussion that the cantilever’s x- or y- axis motion is achieved with at least two actuators. If the actuators possess different stiffness-mass proportions, their resonance frequencies can not be the same.

Therefore, it is evidential to say that the resonance frequencies of the three electromagnetic actuators respect to their own axial direction are all around 205Hz.

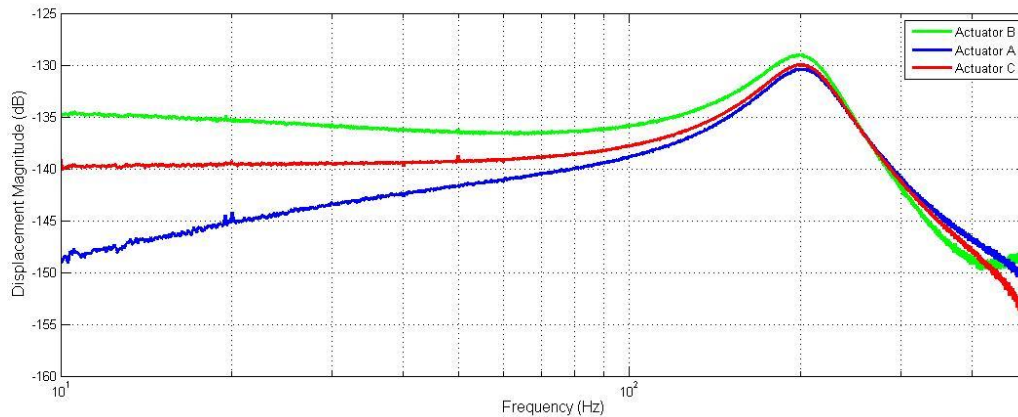


Figure 3. 14, the displacement response of the actuator A, B, and C with 8 V x-axis input.

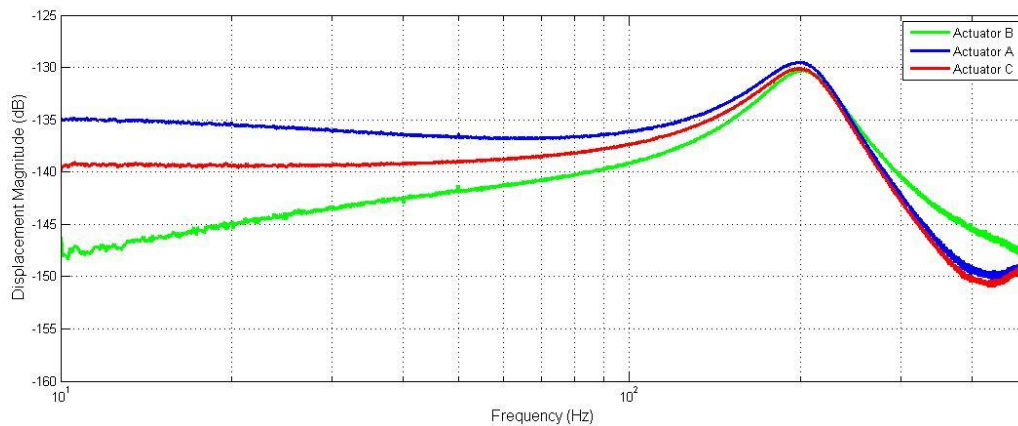


Figure 3. 15, the displacement response of the actuator A, B, and C with 8V y-axis input

Based on the plots, the inferences can be as follows:

3.3.2 Measurements along the z axis

After the orientation rectification, measurements are done along the cantilever's z axis in order to test the actuation resonance frequency. The results concerning to the three measurement points are demonstrated in Figure 3.16. It can be observed that all three plots show significant resonance peaks at about 205 Hz. However, for different curves, some visible "bumps" turn up synchronously in the low frequency domain (mainly in the range of 10-50Hz). Whether these are actuation resonance frequencies, is a problem to be tackled. According to the similar situations described in reference [18], the "bumps" are accounted for by the "phase noise". To investigate whether the bumps are caused by the actuation or the environmental influences, an additional measurement is done with a condition of no power supply. That is to say the actuation system does not function in the measuring process. The corresponding result associated with one of the previous results (tested with the z axis input) is illustrated in Figure 3.17.

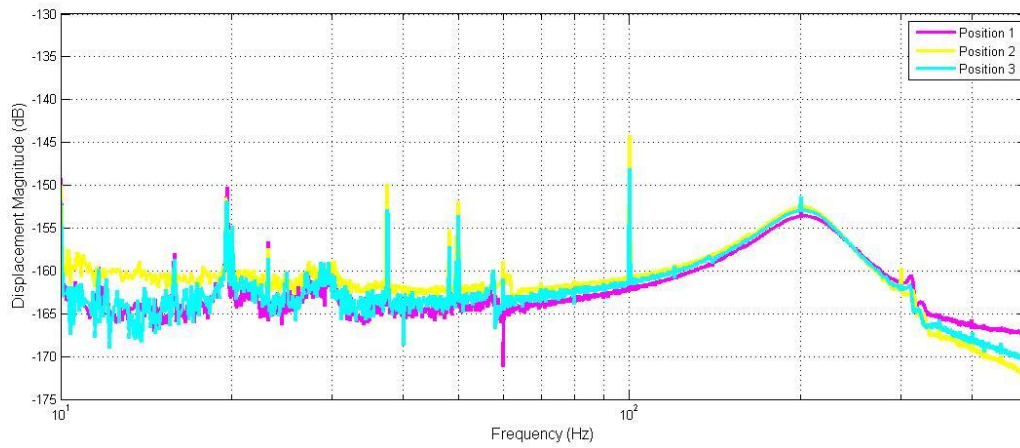


Figure 3. 16, the actuation frequency responses with respect to the three measurement points

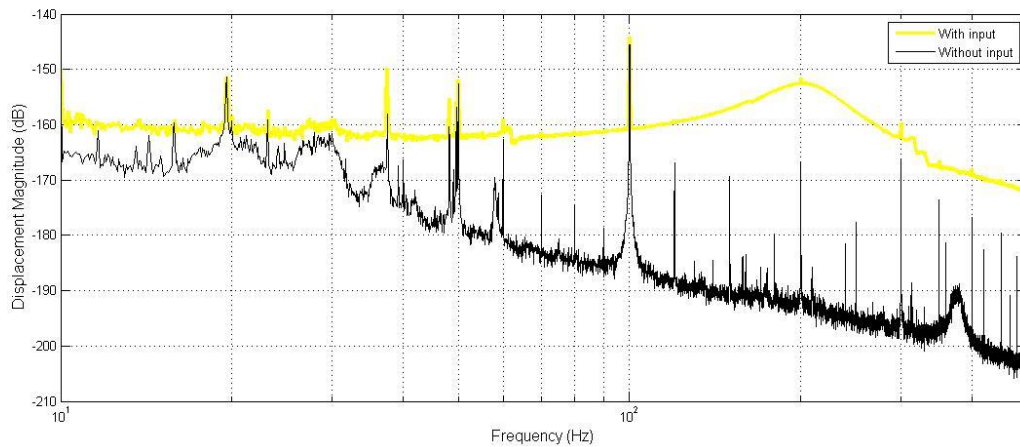


Figure 3. 17, the actuation responses with input signal (pink) and without input signal

By contrast, it is noticeable that the two curves feature extremely similar in the low frequency domain, meaning that the bumps are caused by the environments instead of the actuation resonance frequencies. With such explanation, it is reasonable to draw the conclusion that the actuation resonance frequency along the cantilever chip's z axis is also 205Hz.

Characterizations of the z Actuator in the New Nanite Generation

As given in section 2.3.2.1, the z actuation in Nanite A and B is fulfilled by motion compositions of the three actuators. However, the “triangular” formed layout has drawbacks as well. For example, it limits the resonance frequency of the actuations along specific directions, mainly the z direction. In the new Nanite generation as have been introduced in section 2.3.2.3, the actuators for different axes are devised to be mutually independent, meaning that individual actuators can independently accomplish the actuating task. This makes the characterization process much easier than the previous case, as one could simply analyze a single actuator for a specific axis actuation.

Since the motion of the z actuator is vital for the image reconstruction, it is paramount to know some of its properties, such as the driving force, the maximum driving stroke, the actuation resonance frequency and the heat conduction. For the convenience of the characterizations, Nanosurf rebuilt the z actuator as demonstrated in Figure 4.1, where the coil-embedded flexprint is clamped on a stable stage, leaving the rest part free standing in the air; while in the orthogonal direction, the magnets are disposed right above the coil through two suspension plates up and down in providing a stable magnetic atmosphere. As have been explained in the section 3.2.3.2 b), to achieve the vertical actuation, the embedded coil is arranged to be lying between the magnetic shadows on the flexprint.



Figure 4. 1, left) the test sample: the flexprint with coil inside was suspended through a fabricated frame (black) which is additionally utilized to hold the magnets from an orthogonal direction; right) the corresponding driving mechanism.

In this chapter, simulations and measurements are conducted to fulfill characterizations of different parameters. To have a feeling about how much Lorentz force can be generated, a COMSOL simulation model is established and discussed in section 4.1. In section 4.2, a high resolution imaging system is utilized to characterize the linearity (an important characteristic for AFM actuators) of this new actuator, which is achieved by investigating the relation between the maximum deflection and the power input. Section 4.3 gives the mathematical calculations of the actuator’s resonance frequency, associated with a practical measurement of its dynamic response with the help of the Laser Doppler Vibrometer. In the end, simulations and measurements pertaining to the heat conduction in the flexprint are discussed.

4.1 Simulation of the Lorentz force

To estimate how much Lorentz force can be generated with the z-axis actuator, a 3D COMSOL model was established. To ease the COMSOL simulation, especially the meshing process, some simplifications based on the model shown in Figure 4.1 were made and expounded below.

a) In practical, the coil is fabricated within the poly material which is used as a carrier for the cantilever chip. However, as the polymer part does not contribute to the force generation, it was not included in our simulation model. In addition, as we can apply fixed constraint through the COMSOL software, the suspension structure was also omitted.

b) A 3D model of the real embedded coil is demonstrated in Figure 4.2. The illustration consists of 12 ring-shaped coils in each layer and 10 layers in total. The cross section of the coil is in the order of 0.015mmx0.0035mm, which is quite small and makes the meshing process quite difficult. For the sake of ease, a simplification is made: the 10-layer coil is simplified to be one layer, with its original height unchanged. This means the simulated height not only contains the real coil layers, but also takes the air gaps in between into account. However, as the objective is to obtain the field intensity B at different circles and further apply the Lorentz and Laplace equation ($F = LI \times B$) to calculate the exerted force, It is not difficult to image that this simplification does not influence the simulation too much, although the impact does exist.

c) Another simplification is made on the basis of the structural characteristic. Since the coils are almost symmetric, it is reasonable and sufficient to have a quarter of the real structure to analyze and address the problem.

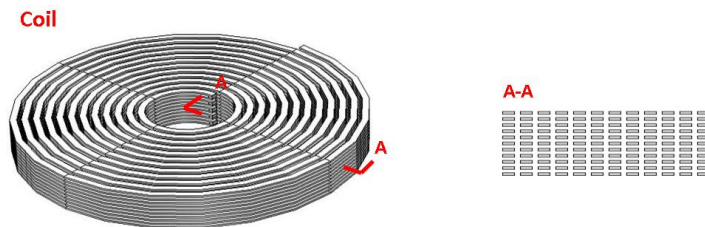


Figure 4. 2, the real coil structure with its cross section

With explanations above, a simplified concept is formed and the concrete model configuration is shown in Figure 4.3. As can be observed, the model is composed of three parts: the Magnets, the coil segments and the surrounding air.

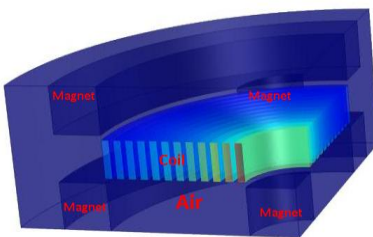


Figure 4. 3, the simulation model for the Lorentz Force

By appropriately defining the domains, materials, and the boundary conditions, the magnetic flux distribution can be obtained and is further represented in Figure 4.4 (left). The image reveals that the density of the flux is not identical for arbitrary locations, which from another perspective indicates the variations of the field strength with respect to the diameters of the coils. As expected: close to the magnets, the flux density is high, and away from the magnets, the flux density is low. For further verification, the distribution of the magnetic field intensity B is depicted and represented in Figure 4.4 (right). From the illustration, it can be explicitly observed that the intensity

vectors close to the inner and outer magnets are with larger modulus than the vectors between the two magnets. Besides, one may also discover that the field intensity in the vicinity of the inner magnets appears to be much stronger than the field intensity near the outer magnets. This can be explained by the fact that the magnetic flux lines are always closed loops, and for a given magnetic field, the total amount of the flux line should be rationally constant regardless of the counting position. However, the volumes of the rings do differ from each other as they have different inner and outer diameters. This accounts for the field density difference.

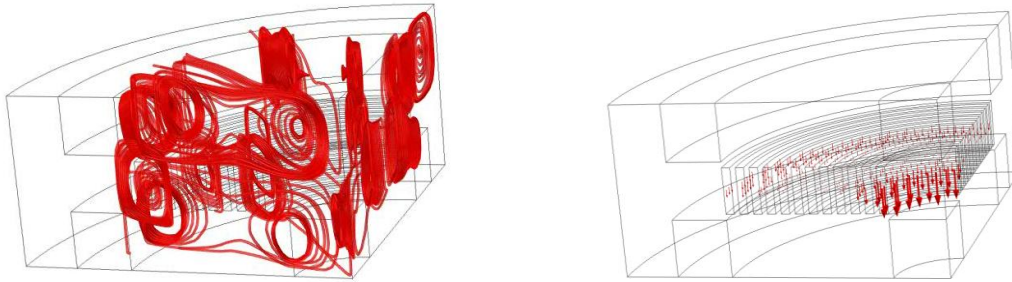


Figure 4. 4, left) magnetic flux density; right) the force distribution.

To quantitatively identify the difference and for the subsequent calculation, the minimum and maximum magnetic field intensity concerning the ring diameters were obtained from the COMSOL model, and listed from the inner circle (the 1st circle) to the outer one (the 12th circle) in Table 4.1 .

Coil number	Minimum B (T)	Maximum B (T)
The 1st circle	0.4162	0.7382
The 2nd circle	0.2853	0.4114
The 3rd circle	0.152	0.2443
The 4th circle	0.0908	0.1558
The 5th circle	0.0651	0.1054
The 6th circle	0.0605	0.0858
The 7th circle	0.0636	0.1026
The 8th circle	0.0831	0.1437
The 9th circle	0.1269	0.2112
The 10th circle	0.2064	0.3086
The 11th circle	0.348	0.4851
The 12th circle	0.4073	0.7125

Table 4. 1, the magnetic flux density at different coil spirals

The total length of the coil is calculated to be ranging from 1.7902m to 1.9038m, in consideration of the inner and outer diameter of each ring. Based on that, the Lorentz force exerted at every ring structure can be computed according to the formula $F = LI \times B$. With a current supply of 0.1A, the accumulated Force, that is the sum of force generated on the individual ring, is estimated to be in the range of 0.0353N ~0.0597N. Compared to the weight of the flexprint which is about 0.0036N, the actuator is conceived to be eligible to achieve a reliable actuation.

4.2 Characterization of the deflection

One of the important criteria in weighing up an actuator is the maximum deflection it can achieve, which is directly related to the scan range of an AFM. In general, a high index means a good capability of scanning a large area (for the x-y plane) and a high depth point (along the z axis). Since the actuator in Figure 4.1 is devised for the z-axis actuation, the maximum deflection of this actuator determines the scan range along the cantilever's z axis. To characterize this parameter, we used the microscope from the LDV to capture the image of the end of the flexprint as shown in Figure 4.5. By counting the pixel shift between the original position and the position under a static working current, one could easily derive the achieved deflection. On the other hand, the linearity of an AFM

actuator is also very important, the characterization of which can be realized by investigating the relationship between the power input and the maximum deflection. Therefore, signals with different amplitudes are conceived to supply to the structure. In addition, for the ease of image acquisitions, a "Square Wave" is selected as a power function as it can produce a temporally stable single (with a low frequency setting). Given the resistance of the inbuilt coil (9 Ohm) and its maximum dynamic working current (300mA), the amplitude of the input voltage is chosen to be in a range of 0.2V to 1.4V. For example, from -1.4V to 1.4V, the flexprint will move from the upper extreme point to the lower one, and result in a pixel shift between the corresponding images. Based on the thickness of the flexprint (1mm) and the pixels it takes (455 pixels), one could easily calculate the deflection.

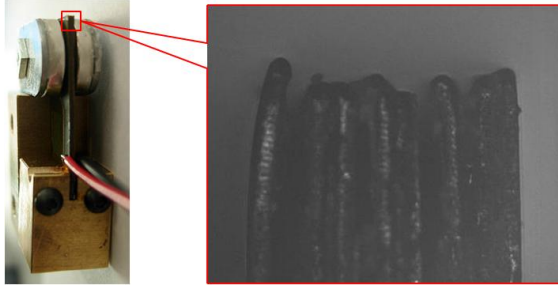


Figure 4.5. the side view image of the flexprint's end

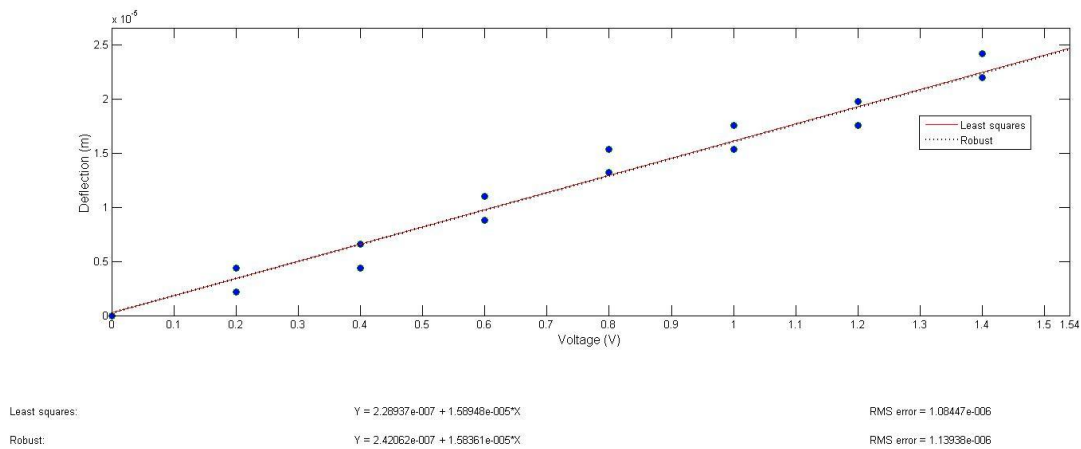


Figure 4.6. power input vs. maximum deflection.

Following this strategy, the images under different power inputs were captured, and in the obtained pictures, several significant points were traced in checking the deflection of the flexprint. In total, there are 96 measurement points involved, with the concrete information revealed in Appendix C Table C1 (pixel shift) and C2 (corresponding deflection). Due to the fact that some points overlay each other, fewer points can be reviewed from Figure 4.5. From the plot, it can be discovered that the maximum deflection increases almost linearly in the wake of the augment of the power input. To find out the mathematical description, linear regression is used. As shown in Figure 4.6, two solutions, "least squares" and "robust" are included. It can be observed that the two linear lines have more or less the same slope ($1.58 \mu\text{m}/\text{V}$) and an almost equivalent standard deviation (1.2nm). Given the fact that the most deviated point is 2.66nm apart from the regression line, it can be concluded that the linearity is maintained within the 0.1% range. With such context, it can be estimated that the actuator can generate a deflection of about $10.67 \mu\text{m}$ under a static working current of 150mA.

4.3 Characterization of the resonance frequency

The study on the actuator's dynamic properties is another direction one needs to place a particular emphasis. This is because they normally determines the scan speed and the reliability of the actuating system, and thus directly affect the qualities of the obtained images. Therefore, the resonance frequency of the z actuator is discussed and characterized in this section.

4.3.1 Calculations

Before the experimental test, estimation is made on the basis of the mathematical calculations. One could easily read from Figure 4.1 that the essence of the actuation is the flexiprint (beam) bending. It is therefore reasonable to simplify this model to be a free standing beam for the benefit of the calculation. The concrete explanations are demonstrated as follows:

According to section 3.2.1 where the total length of the coil is derived to be approximately 1.85m, and considering a cross section of 0.15mmX0.04mm, the volume and mass of the coil part can be calculated as:

$$V_c = l_c S_c = 1.85 \times 0.15 \times 10^{-3} \times 0.04 \times 10^{-3} \approx 1.1 \times 10^{-8} m^3$$

$$M_c = \rho_c V_c = 19.3 \times 10^3 \times 1.1 \times 10^{-8} = 2.12 \times 10^{-4} kg$$

Where:

- V_c = the total volume of the coil
- M_c = the total mass of the coil
- l_c = the length of the coil
- S_c = the area of the coil's cross section
- ρ_c = the density of the coil

Since there is about 4 mm flexiprint clamped by the suspension structure, only 17mm is taken into account in as the functional length of the bending beam. The volume of the polyimide can be interpreted as the subtraction between the volumes of the whole flexiprint and the coil part, which can be written as:

$$V_p = V_f - V_c = l_f w_f h_f - V_c = 17 \times 10^{-3} \times 9 \times 10^{-3} \times 1 \times 10^{-3} - 1.1 \times 10^{-8} = 14.2 \times 10^{-8} m^3$$

And the mass of the polyimide can be expressed as:

$$M_p = \rho_p V_p = 1.1 \times 10^3 \times 14.2 \times 10^{-8} \approx 15.62 \times 10^{-5} kg$$

In which:

- V_p = the volume of the polyimide
- V_f = the total volume of the flexiprint
- l_f = the length of the flexiprint
- w_f = the width of the flexiprint
- h_f = the height of the flexiprint
- M_p = the mass of the polyimide
- ρ_p = the density of the polyimide

The mass of the flexiprint M_f should be the sum of the masses of the two objects, written as:

$$M_f = M_p + M_c = 36.8 \times 10^{-5} kg$$

To calculate the second moment of inertia of the flexiprint, one could follow the general formula for a rectangular cross section as demonstrated in equation 4.1

$$I = \frac{1}{12}bh^3 \quad (4.1)$$

Where:

I = the moment inertia about the reference axis

b = the side parallel to the reference axis

h = the height of the cross section

In this specific case, $b = w_f = 9 \times 10^{-3} m$; $h = h_f = 1 \times 10^{-3} m$. By substituting the corresponding values into equation 4.1, the moment of inertia of the suspension beam can be expressed as

$$I = \frac{1}{12}w_f h_f^3$$

According to the vibration resonance frequency of a bending beam, the first vibration resonance frequency of the flexprint can be derived as:

$$f = \frac{(1.875)^2}{2\pi} \sqrt{\frac{3EI}{mL^3}} = \frac{(1.875)^2}{2\pi} \sqrt{\frac{Ew_f h_f^3}{4M_f l_f^3}} = \frac{(1.875)^2}{2\pi} \sqrt{\frac{3.2 \times 10^9 \times 9 \times 10^{-3} \times (1 \times 10^{-3})^3}{4 \times 36.8 \times 10^{-5} \times (17 \times 10^{-3})^3}} \approx 1117 Hz$$

$$k = \frac{3EI}{l_f^3} = \frac{Ew_f h_f^3}{4l_f^3} = \frac{3.2 \times 10^9 \times 9 \times 10^{-3} \times (1 \times 10^{-3})^3}{4 \times (17 \times 10^{-3})^3} = 1465.5 N/m$$

4.3.2 Measurement and result

Since the flexiprint of the new z actuator only moves along the vertical direction (with an orientation shown in Figure 4.1), it is convenient to use the Laser Doppler Vibrometer (introduced in section 3.1) to implement the out-of-plane measurement to characterize the corresponding resonance frequency. Considering the design has a coil resistance of approximately 9 Ohm and a preferable static working current of 150mA, measurements with power input of 0.4V, 0.8V, 1.0V and no input were separated executed for the purpose of comparisons.

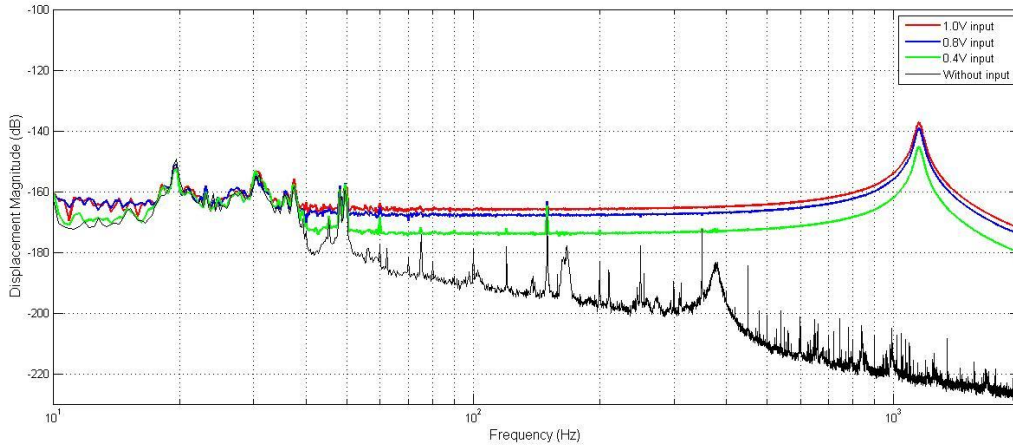


Figure 4. 7, the dynamic response of the new z actuator under treatment of 0.4V(green), 0.8 V(blue), 1.0V(red) and no input (black)

From the measurement results shown in Figure 4.7, one may easily discover that the displacement magnitude increases with the augment of the power input (from 0.4V to 1.0 V), which answers the expectation that a high power input will lead to a large deflection. On the other hand, the measurements with power inputs show some significant peaks at 1150 Hz. However, with careful observations, one may find multiple small bumps appear in the low frequency domain, mainly in the range of 10 to 50 Hz. In characterizing what the bumps are, an additional experiment which is accomplished under the condition of no input is conducted, with its corresponding result plotted in black in Figure 4.7. It is to see that, from 10 to 50 Hz, the bumps measured with power inputs feature

almost the same as how the black curve (measured without any input signal) shapes. This happens because the z actuator in this design can only achieve small deflections, normally in the order of a few micrometers; when working with low frequency signals, the induced vibrations might have larger amplitudes compared to the real deflection the actuator can achieve, which leads to the phenomenon we observed in Figure 4.7.

Besides, another measurement was executed to check the dynamic response of the (flexprint) clamper, namely the part to hold the flexprint (the black structure in Figure 4.1). The obtained data was further processed and plotted in Figure 4.8, associated with the response of the flexprint measured with and without input signal. With comparisons, one could observe that the clamp structure does not behave too much until the resonance peak of the flexprint appears. The account for this is that the flexprint is suspended on this mechanical clamper and any big movement on the flexprint will be transferred to the clamper and induce associate motions. With such explanation, It is sufficient to draw the conclusion the significant peak in the graph is the resonance frequency of the z actuator for the new Nanite generation, which is approximately 1150Hz.

In comparison with the old versioned actuator, the resonance frequency of the electromagnetic actuator is much higher. This means that this actuator can be operated with a comparable high frequency and thus a high scan speed can be achieved.

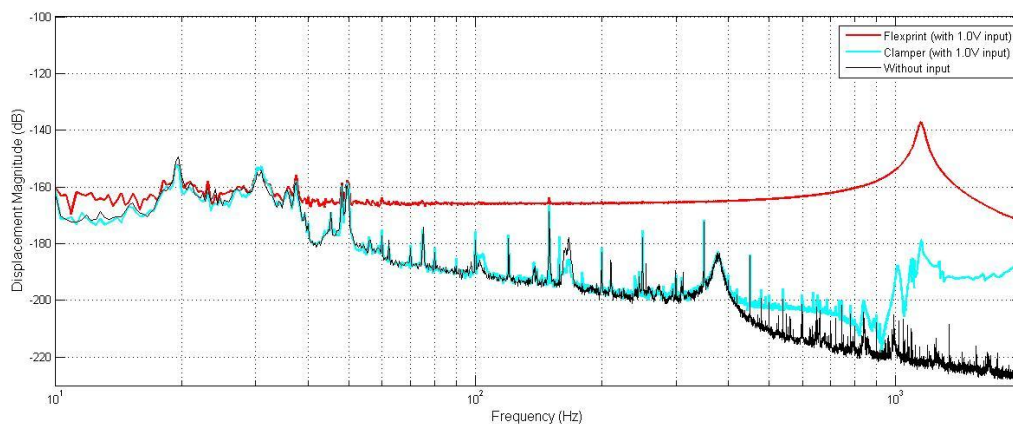


Figure 4. 8, the dynamic response of the new z actuator under a treatment of 1.0V (red), no input (black) and the dynamic response of the clamp structure (cyan)

4.4 Characterization of the heat conduction

It is generally recognized that thermal problems encountered in unexpected occasions, are very obstinate, such as heat accumulations and unexpected convections. Of course, for the new z actuator, it is of no exception. Therefore, to eliminate, or at least to reduce the thermal influences, such as thermal drift, high temperate induced melting, and even damages, it is valuable to check how heat is dissipated through the structure.

As a rule of thumb, doping a high conductive material to less conductive substrate will increase the conductivity of the latter substrate. This is also the concept used in fabricating this flexprint. However, how temperature distributes over the sample, which part is the hottest, whether it is good enough for the heat dissipation are still problems deserving of study. Currently, there are two different designs for the flexprint, one is with small bonding pad (shown in Figure 4.9 left) and the other is with big bonding pad (shown in Figure 4.9 right). To check the efficiency of the two designs, some simulations and characterizations are done in this section. Hopefully, this could provide valuable information for further improvements.

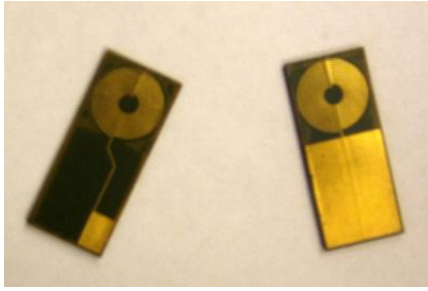


Figure 4. 9, flexprint with different sized bonding pads.

4.4.1 Simulations

Prior to the measurement, simulations are first done to roughly estimate the temperature distributions on the two samples. With a same power input, the results regarding the small and big bonding pad design are obtained and separately shown in Figure 4.10 left and right. From the results, one may discover that no matter how large the bonding pad is, there is always more heat accumulating in the center of the coils, which results in a high temperature there. One of the differences is that the highest temperature in the small-bonding-pad design is about 14.8 degree Celsius higher than that in the big-bonding-pad design. Besides, it can be also found that the temperature span in the former case is much larger (47.2°C) in comparison with the latter case (23.8°C). In Figure 10 left, one can clearly observe that temperature in some areas approaches the room temperature, meaning that those areas are not useful for the heat dissipation. By contrast, the temperature in the big-bonding-pad design is more evenly distributed. Both effects indicate a big bonding pad is helpful for the heat transfer and system cooling.

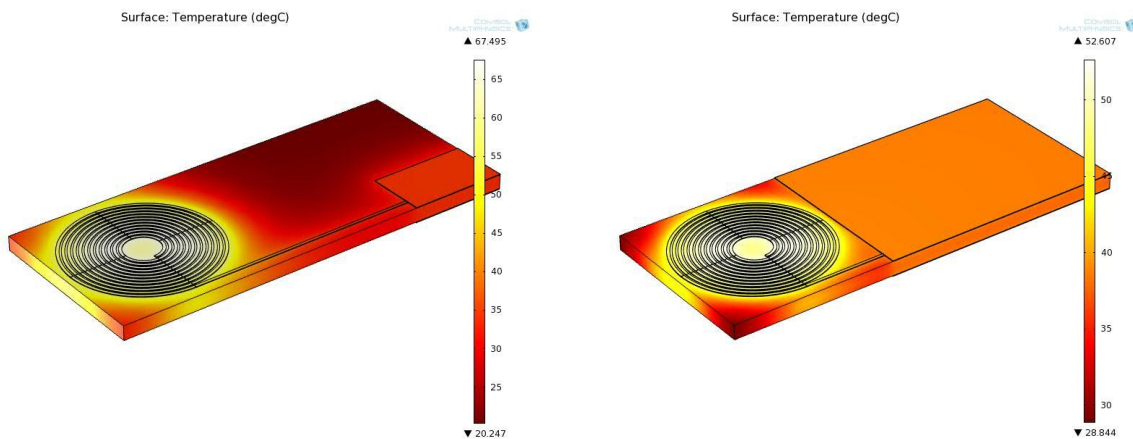


Figure 4. 10, temperature distribution on the flexprint: left) with small bonding pad; right) with big bonding pad

To estimate the heat conductivity of the bonding pad area, we first use a small calculation to do a rough estimation. According to Newton's law of cooling that the rate of heat transfer is approximately proportional to the surface temperature difference, the mathematical description can be expressed as shown in equation 4.2:

$$q_s = h_c \Delta T \quad (4.2)$$

Where

q_s = heat flux from one surface to the other, [W / m^2];

h_c = heat transfer coefficient, [$W / m^2 K$];

ΔT = the temperature difference between two surfaces, [K].

To calculate the heat conductivity of a combined material with a "sandwich" form, just like the model shown in Figure 4.11, the overall heat flux can be written as given in equation 4.3:

$$Q = \frac{T_i - T_0}{L_i / \kappa_1 A_1} + \frac{T_i - T_0}{L_2 / \kappa_2 A_2} + \frac{T_i - T_0}{L_3 / \kappa_3 A_3} + \dots \quad (4.3)$$

Where:

Q = the total amount of heat, [W];

$T_i - T_0$ = the temperature difference between the two surfaces [K];

L_i ($i = 1, 2, 3, \dots$) = length of different materials [m];

κ_i ($i = 1, 2, 3, \dots$) = heat transfer coefficient of different materials, [W/mK];

A_i ($i = 1, 2, 3, \dots$) = cross section perpendicular to the heat flux, [m²].

On the other hand, the total amount of heat can be expressed as shown in equation 4.4.

$$Q = hA(T_i - T_0) \quad (4.4)$$

In which,

h = overall heat transfer coefficient, [W/m²K].

With such explanation, the heat transfer coefficient for the metal pad area can be calculated as:

$$h = \frac{\kappa_m A_m}{LA} + \frac{\kappa_p A_p}{LA} + \frac{\kappa_m A_m}{LA}$$

Hence, the overall thermal conductivity can be therefore obtained and written as:

$$\kappa = \frac{h}{L} = \frac{\kappa_m A_m}{A} + \frac{\kappa_p A_p}{A} + \frac{\kappa_m A_m}{A}$$

Where:

κ_m = the thermal conductivity of the metal part, ≈ 318 W/mK [20];

κ_p = the thermal conductivity of the polymer material, ≈ 0.4 W/mK

A_m = the cross section of the metal pad; $\approx 0.315 \times 10^{-6}$ m²

A_p = the cross section of the polymer material; $\approx 9 \times 10^{-6}$ m²

The overall thermal conductivity can be calculated as:

$$\kappa = \frac{\kappa_m A_m}{A} + \frac{\kappa_p A_p}{A} + \frac{\kappa_m A_m}{A} = \frac{318 \times 0.315 \times 10^{-6}}{9.63 \times 10^{-6}} + \frac{0.4 \times 9 \times 10^{-6}}{9.63 \times 10^{-6}} + \frac{318 \times 0.315 \times 10^{-6}}{9.63 \times 10^{-6}} = 21.2 \text{ W/mK}$$

It should be noted that the calculation above is based on an ideal situation that no thermal interaction between different materials is involved. This never happens in real life. To find a more accurate way to describe the thermal conductivity of this material, a simulation model is built up as shown in Figure 4.11. By inducing a temperature difference of about 12K between two surfaces, the conductive heat flux is approximately 176110W/m², which means a total heat of 1.696W. Therefore, the heat conductivity can be calculated as:

$$\kappa = \frac{HL}{A\Delta T} = \frac{1.696 \times 11 \times 10^{-3}}{1.07 \times 10^{-3} \times 9 \times 10^{-3} \times 12} = 16.2 \text{ W/(m} \cdot \text{K)}$$

Where:

κ = thermal conductivity

H = power input

As the thermal conductivity of the combined material is much higher than the pure polymer material, it from another perspective proves that the metal pads do help to improve the heat conduction in the flexprint.

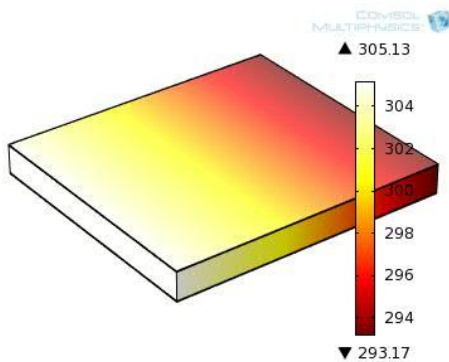


Figure 4. 11 a simulation on the metal pad area.

4.4.2 Measurement and result

Initially, we tried to use the device in Figure 4.12 left) (developed by Rene Poelma) to check the efficiency of the heat conduction in the flexprint. The working principle is as follows: two copper pillars are adopted in this design and arranged above and beneath the test sample for heat conduction. On each pillar, there are four sensors (the yellow structures) integrated to detect the local temperatures. During the measurement, the upper interface of the top pillar will get heated by the predesigned resistors (represented by the black box, with two input junctions sticking out), and the generated heat will transfer from the top pillar to the bottom. Knowing the information from individual sensors, the temperature drop over the the test sample can be derived, which delivers the information of the sample's thermal conductivity along the vertical direction. To reduce the heat convections at the structural interface, the whole measurement setup can be placed in a vacuum chamber as shown in Figure 4.12 right).

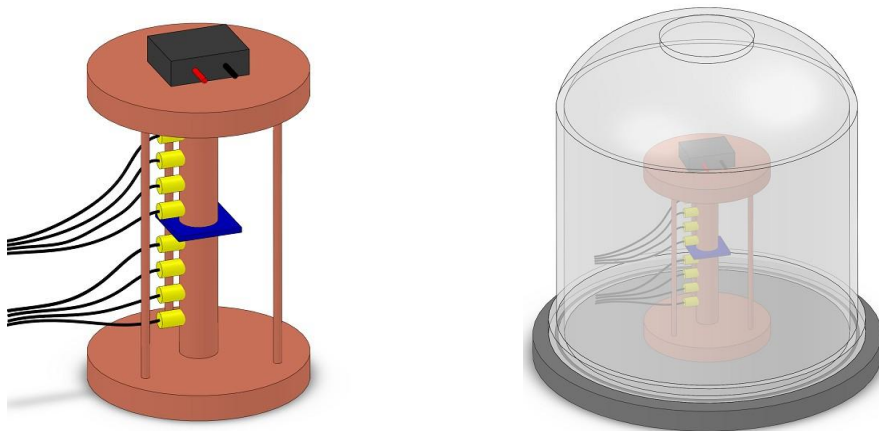


Figure 4. 12, left) the device for heat conduction measurement; right) the device in a vacuum chamber.

During the implementation, some problems are found:

- 1) To characterize the heat conduction along the length direction, the sample in Figure 4.10 should be orientated 90° and inserted between the two pillars. However, the current device has no clamping structures at the pillar ends, it is therefore difficult to free support the sample.
- 2) With some tests, we found that the sample (about 1mm) is too thick for the device to characterize. This conclusion is based on the measurement along the thickness direction. According to what presents in the measurement result, only the top four sensors show temperature changes due to the heating effect, the bottom four sensors staying at the room temperature.

Assuming condition 1) and 2) are resolvable, a big issue is the sample composition. Since they are inhomogeneous compounds, the test result can only deliver the heat conduction over the sample length. It means that the temperature distribution between the two edges is not derivable like what we can do with homogenous material. In this sense, this device is not competent to accomplish the desired task.

In seeking other methods, Thermal camera "FLIR A315" is conceived to be eligible and utilized here to accomplish the task. By detecting the Infrared radiated from an object, the camera is able to deliver the thermal topography. Considering the actuator is to be adopted in a normal situation, the experiment is therefore executed at the room temperature and a standard pressure. Moreover, because the camera collects not only radiations from the targeted object, but also radiations reflected by the sample surface [21], a dark environment is set up to eliminate possible impacts from the ambient. Other than that, as the manual suggests, the obtained image from this camera is not only related to the temperature distribution, but also as a function of the material emissivity. In general, a material with a low emissivity factor is relatively poor at radiations and absorptions, but on the other hand has a high reflectivity index, mirrors and polished metals for instance. For this reason, the temperature distributions on these materials are barely visible under the thermal camera. For improvement in this specific case, a thin soot layer is coated on the surface of the flexprint by a flaming candle. Although this coated layer can not change the radiation of the metal pads, it can be used as a media to reflect the temperature distribution of the flexprint. In other words, what we measure here is the temperature of the coated soot. With the same current input (150mA), the images corresponding to the two designs are obtained and in Figure 4.13.

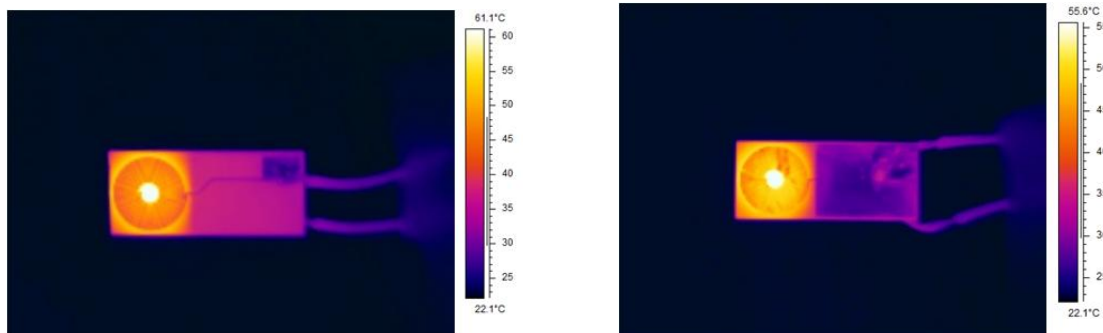


Figure 4. 13, thermal topography images of the flexprint: left) with small bonding pad; right) with big bonding pad.

The temperature gradient in either of the images indicates that the maximum temperature happens in the middle of the coils, which is conformity with the simulations in Figure 4.10. Apart from that, one could also read that the maximum temperature with the small-bonding-pad design is 5.5°C higher than the other one. Although with small deviations which can be either caused by the slight difference between the simulation model and the real sample or caused by the difference between simulated environment and the real one, both results suggest that the a larger bonding pad is helpful for the heat conduction in the flexprint. One may notice that the temperature at the pad area is still kind of dark. This is due to the fact that the soot layer is coated unevenly, which is difficult to improve based on the current situation. But it is worth mentioning that the images here already have big improvements at exhibiting the temperature of the pad area in comparison with the images taken without soot, where the metal pads present to be dark blue and almost approach the room temperature.

Bimorph Actuator for the Next Nanite Generation

As discussed in section 2.3.2.3, the z actuation in the new Nanite generation is accomplished by a single electromagnetic actuator, which eliminates the drawbacks brought about by the triangular formed actuator in Nanite A and B and improves the design flexibility. Although with so many advantages, a key issue here is the mass problem. Such consideration is based on the fact that this z-actuator will be further attached on an x-y platform which is activated by the x- and y- actuators, attaching a big massed actuator in this case will affect the performance of the whole actuator. With this context, piezoelectric actuators (on the basis of the ceramic bimorph benders) are considered for substitution as they are normally light weighted and have many superior properties in actuating, such as high actuation resolution and large generated forces. To check the feasibility of such replacement, some simulations and measurements are involved in this chapter. To start off, different actuating concepts are initialized and discussed in section 5.1. With careful considerations, two potential concepts "half actuator" and "symmetric actuator" are selected out and compared in section 5.2. With an absolute predominance, the half actuators are conceived to be promising at substitution and therefore further studied. In section 5.3, the influencing parameters on the achievable maximum deflection are investigated, including the individual bender length, the power input and the overlap. Eventually, real bimorph actuators were built up to check the difference between the simulations and the practical performances, with the discussions given in section 5.4.

5.1 Concepts of the Bimorph Actuator

The actuation concept is based on the bimorph structure introduced in section 2.3.1. With one end of the bender fixed, the other end can bend up and down to achieve the actuation purpose. At this attempt, we choose to use a standard ceramic bimorph bender CMBP02 (from NOLIAC, shown in Figure 5.1) as a basic element to develop our piezoelectric actuator. In seeking a suitable configuration, different concepts were considered.



Figure 5. 1, ceramic bimorph bender "CMBP02"

The first idea is to use a single bimorph bender. As the developing actuator will be eventually adopted in AFM, low power consumption is always preferred. In this situation, using one bender can not generate a sufficient large deflection. Another drawback of this concept is that, under electrical treatments, the end of the bending beam will be always at a certain angle to the horizontal position as depicted in Figure 5.2 a. This is inconvenient for the vertical (z axis) actuation and very likely to induce distortions on the scan images. On the other hand, in pursuing a large stroke, the concept by stacking benders together might be needed. The configurations are simply illustrated in Figure 5.2 b and c. As can be observed, due to the angle at the end of the first (top) bender, the second bender will bend along the formed bending surface and give few improvements on the maximum deflection. Analogously, stacking more benders together can only make their generated deflections compensate each other, leaving the accumulated deflection almost equivalent to the deflection of a single bender.

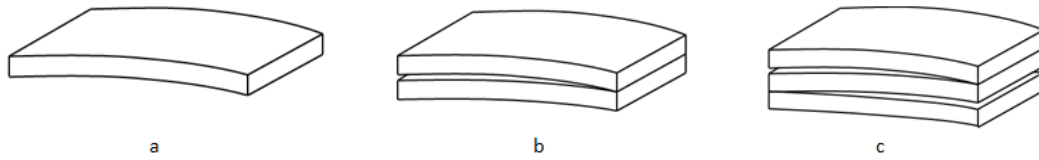


Figure 5. 2, a, single beam deflection, , with a generated angle θ at the beam end with respect to the horizontal line ; b, structure with two bimorph benders; c, structure with three bimorph benders.

To tackle this issue, two benders joint “end to end” are conceived and depicted in Figure 5.3. With opposite polarizations, this assembly could not only achieve a doubled actuation stroke, but also form an almost horizontal surface at the end, which to a great extent eliminates the angular deviation caused by the single beam actuation.

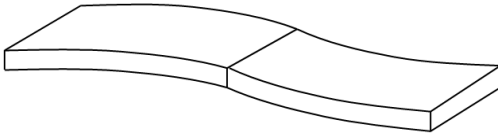


Figure 5. 3, two benders connected endto end, with their polarization positioned in different direction.

Based on the configuration in Figure 5.3, we also considered to use a symmetric structure to boost the actuator performance. An illustration is shown in Figure 5.4, where a small platform is applied to join the symmetric benders and can be further used for the chip installation.

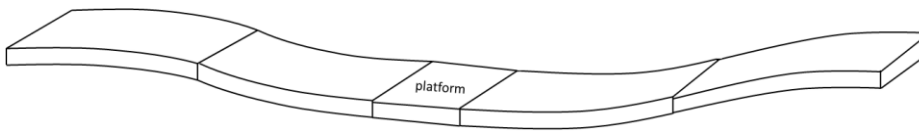


Figure 5. 4, the symmetric actuator

One important aspect to be considered is how to join the benders. Rationally, different mechanisms can be adopted, such as mechanical clampers, soldering and glue. For firm connections, mechanical clamping is not a bad solution. However, the achievement of such connection is normally associated with additional components, screws for example. This will make the bender stacking very difficult, not to mention the increase of the actuating mass. On the other hand, as the number of the bender in stock is limited, disassembling might be needed in the future. To avoid damages during the separation, permanent connections are not preferred. In this sense, soldering is not recommended. Knowing these points, superglue is considered to be the best choice as it can be easily dissolved by acetone solution.

With glue as a joint media, there are still different ways to achieve the connections. However, gluing the sidewalls as shown in 5.3 is not preferred as such connection is quite instable during the actuation [22]. If one has to use this method, auxiliary structures are needed for fixation. However, as "simplicity" and "light weight" are two important criteria for this design, no additional mass and complicated assembling process is wanted. Therefore, to achieve stable connections, gluing with overlaps as shown in Figure 5.5 is a good solution.

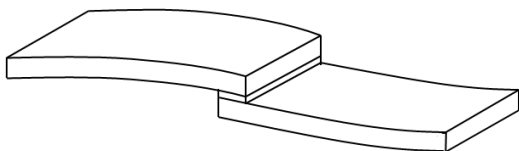


Figure 5. 5, benders joint with overlap

5.2 Concept Comparisons

For the convenience of descriptions in the ensuing sections, hereby we render some structures specific names. For actuators with only half structures, such as the configuration shown in Figure 5.3, we name them as "half actuators", and for actuators with symmetric structures, the configuration in Figure 5.4 for instance, we refer them as "symmetric actuators". In addition, to increase the actuating stroke, it is possible to stack several of the structures together as shown in Figure 5.6. Since there are several repetitive structures involved, the configuration shown either in Figure 5.3 or Figure 5.4 is called one actuating layer. With such context, we can easily specify a structure. For example, the structure in Figure 5.6 (left) can be referred to as "half actuator with 4-layer design" and the right one is named as "symmetric actuator with 3-layer design". In the following sections, we are going to use COMSOL to simulate and compare the two concepts from different aspects.

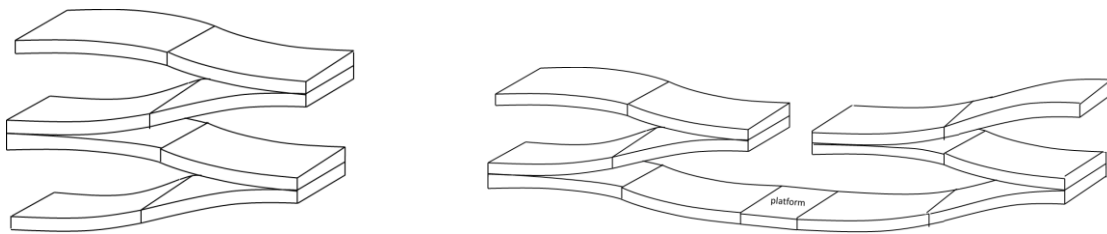


Figure 5. 6, left) half actuator with 4-layer design; right) symmetric actuator with 3-layer design

5.2.1 Comparison of the Deflection

Since the benders are designed for the cantilever's z-axis actuation, the achievable scan range is an important parameter in weighing up whether the actuators are good or not. In general, the more actuating layers an actuator has, the larger deflection it can achieve. However, let it be emphasized, adding actuating layers will at the same time increase the total of the whole structure, which is likely to lead to a low resonance frequency. Considering this, designs with maximum four layers are considered and simulated.

To alleviate the impacts from the other parameters, we keep almost everything almost the same for both actuator classes, including the platform (integrated at the end for the half actuators, and in the middle for the symmetric actuators). In practical applications, the power supply for the AFM actuator is normally maintained within 10V. Hereby we applied a voltage of 10 V to all the benders. The corresponding deformations and deflections are compared in Table 5.1.

The first and obvious information one could have from the simulation is that the maximum deflection increases with the augment of the actuating layers no matter whether it is half actuators or the symmetric ones. For the same layer design, both actuator classes give almost the same deflection, with the deflections of the half actuators slightly higher.

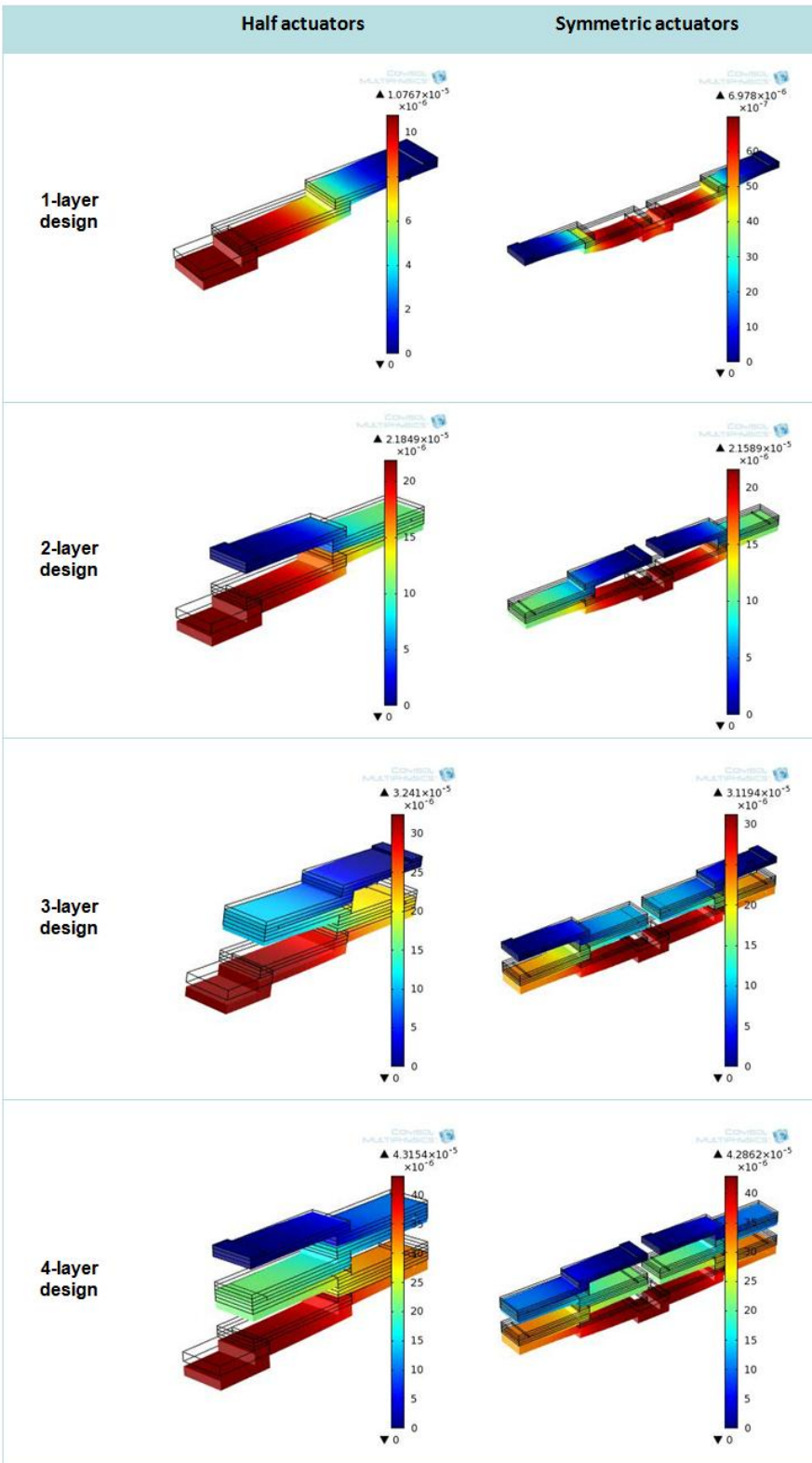


Table 5. 1, the deflections of the half actuators and symmetric actuators with respect to different layer designs

Another thing one could infer from the simulation is that the symmetry is extremely vital for the symmetric actuators. The thickness of the glue, the bender overlap, and the horizontality of the bender orientation are all related parameters. A small assembling deviation on any of these aspects may lead to an asymmetric structure and induce a large torsion on the platform and therefore influence the accuracy of the scanning process. In such cases, the assembly of the symmetric actuators can not be simply accomplished by manual work. The implement of this concept must be in virtue of high precision devices, which, just like the devices used in IC packing, should be able to achieve both position accuracy and a well controlled dose of glue.

5.2.2 Comparison of the Resonance Frequency

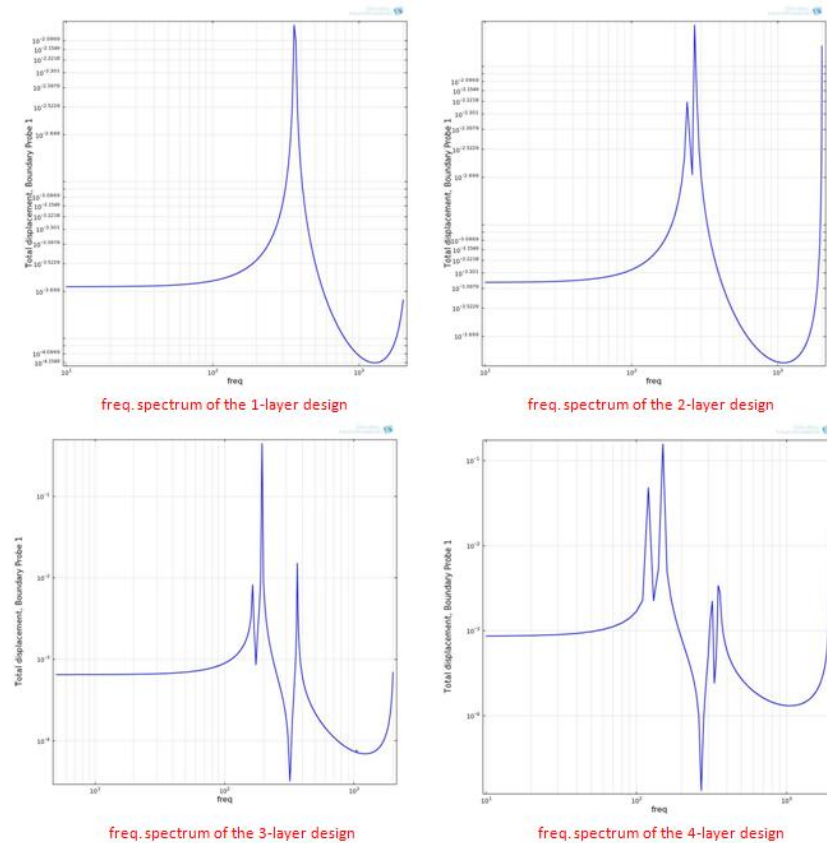


Figure 5. 7, the frequency responses of the "half actuators". the first resonance frequency with respect to the 1-layer design, 2-layer design, 3-layer design, 4-layer design separately appears at 370Hz, 250Hz., 160Hz, and 120Hz.

The dynamic analyses are also done to find out the, corresponding eignfrequencies of different models. Such information will do great contributions to the frequency definition of the power input, as well as the control algorithm design for a higher operating bandwidth. Figure 5.8 delivers the frequency responses of the half actuators with respect to different actuation layers, and Figure 5.9 exhibits the corresponding results from the symmetric designs.

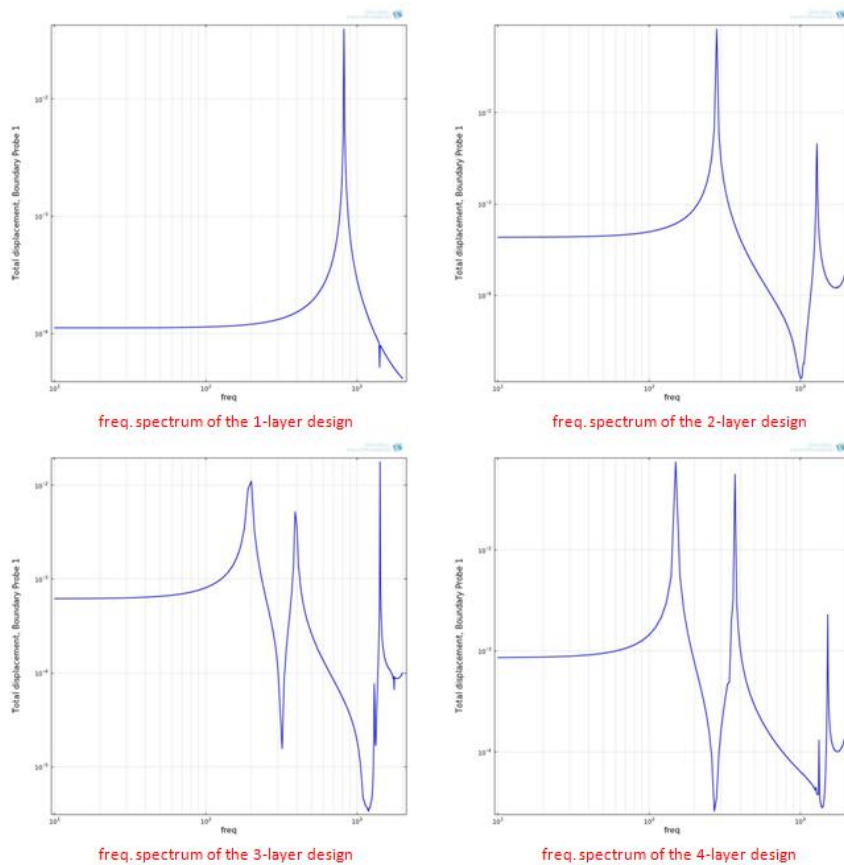


Figure 5. 8, the frequency responses of the " symmetric actuators". The first resonance frequency with respect to the 1-layer design, 2-layer design, 3-layer design, 4-layer design separately appears at 820Hz, 280Hz, 200Hz, and 150Hz.

For the same actuator class, either the half actuators or the symmetric actuators, it is apparent that the first resonance frequency reduces with the increase of the actuation layer. The main reason leading to this phenomenon is that the increase of the actuation layer will add mass to the flexible structure, which, according to the formula $\omega = \sqrt{k/m}$, will reduce the first resonance frequency.

When it comes to the comparisons between the half and symmetric actuators, one may discover that the first resonance frequencies of the symmetric designs are slightly higher than those of the half actuators, except for the 1 layer designs with 450Hz difference. This can be explained by the fact that the platform in the symmetric design to a certain extent restrains the movements of the symmetric structures, and thus limited the freedom of the individual benders. However, the differences are not very noticeable. One principal reason is that the mass of a symmetric structure is almost twice of the corresponding half actuator. Therefore, the combination effect of the structure stiffness and its mass lead us to the simulation results. Another effect one may also observe is that with the increase of the actuation layer, more eigenmodes appear in the frequency spectrum. This is because the glue-bender combinations can be considered as spring-mass systems, integrating more units in a system will result in a complicated dynamic motion.

5.2.3 Other comparisons

In this section, the half actuator and the symmetric actuator are further compared roughly rated in Table 5.2. It is worth noticing that the stars are given relatively, without any absolute reference. Besides the items discussed in section 5.2.2, several other criteria are also involved. One thing we need to consider is the actuating mass. This is because the z actuator will be further attached on a base platform, just like the configuration shown in Figure 2.20, and a light mass is always expected. The other element to consider is the cost of integrated benders. In general,

the symmetric actuator costs twice of its corresponding half actuator. In addition, the volume of the actuator also impacts the design as light and handy are always the design criteria. From the comparison, it is easy to find that the half actuator has more advantages in this application. Therefore, in the following section, we are going to focus on the half actuator.

	Half Actuator	Symmetric Actuator
Deflection	★ ★ ★	★ ★
Resonance Frequency	★ ★	★ ★ ★
Assembly Simplicity	★ ★ ★ ★	★
Mass	★ ★ ★ ★	★ ★
Cost (benders)	★ ★ ★ ★	★
Dimension	★ ★ ★ ★	★ ★

Table 5. 2, the comparison table

5.3 Simulations of the Influencing Parameters

In general, there are several parameters influencing the deflection of the platform, including the power input, the number of the actuation layer, the length of the individual bimorph bender, the horizontal air gap and the glue width. To investigate the impacts of these parameters, COMSOL simulation models are utilized.

5.3.1 Power input

The first parameter we checked is the power input. As the bearing voltage for an individual bimorph bender is 200V. A sweep voltage ranging from 0 to 200V is applied to all four designs. In order to have an intuitive feeling on the general trend between the power input and the deflection, we plotted the discrete data as shown in Figure 5.10. The concrete data can be found in Table D1 in Appendix D. It can be easily observed from the plot that, for each single case, the deflection ascends linearly with the increase of the power input. When comparing the four different designs, one could find that the deflection is almost in proportion with the actuating layers adopted. Therefore, depending on the deflection needed in practical applications, alternatives of the actuating layer-input power array can be selected according to this diagram.

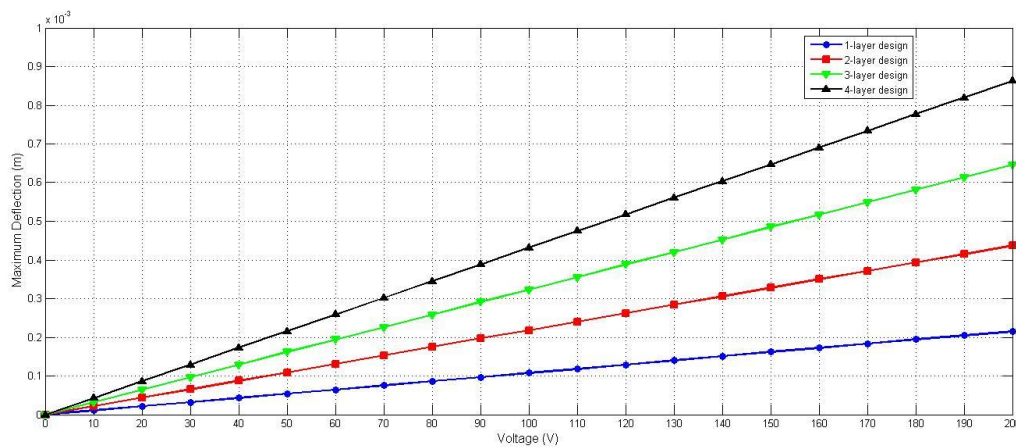


Figure 5. 9, the relation between the power input and the platform deflection

5.3.2 Individual bender length

Although the CMBP02 product has a standard dimension of 21mmx7.8mmx1.25mm, in practical applications, the length of the bender can be trimmed shorter in order to accommodate to the space requirement of specific designs. Nonetheless, such treatment will cause a reduction on the bender's maximum deflection. For such reason, we simulated the influence of the individual bender length with respect to different actuators. The results are shown in Figure 5.11 and Table D2 in Appendix D. The simulations were conducted under a condition of 10V power input and 3mm glue width. In the simulation result, the maximum deflection has a parabolic increasing trend to the increase of the bender length. Therefore, trimming benders in shorter lengths is another way to get a desired deflection. This is a potential method as it can help to restrain the mass and volume of the actuator to fit in a small space.

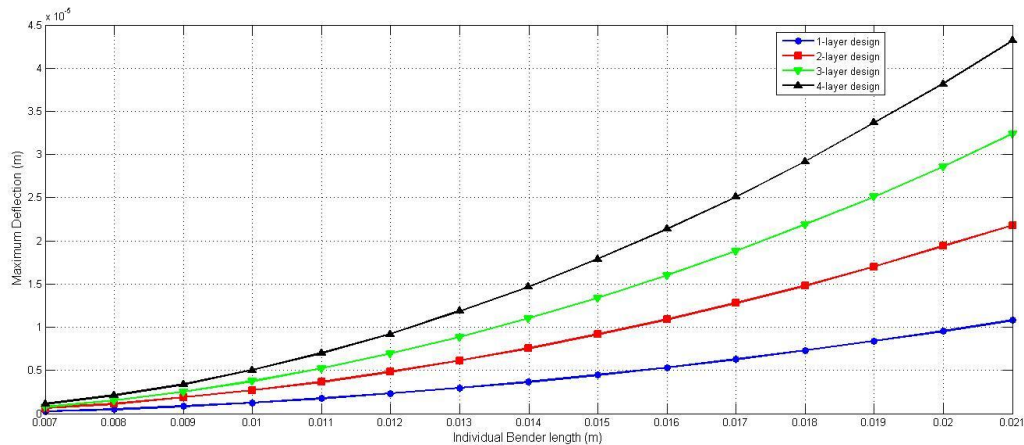


Figure 5. 10, the influence of individual bender length on different structure designs

5.3.3 Glue width/overlap

Another influencing parameter might be the glue width. By choosing different indexes, the total length of the bending structure will change and therefore cause variations on the maximum deflection. To simulate this effect, we shift the glue width from 1 to 10mm to see the corresponding effect. It is worth mentioning that the simulation is under boundary settings of a 10V power input and a 21mm bender length. The simulation result is plotted in Figure 5.12 with the concrete database listed in Appendix D Table D3. It is noticeable that with the increase of the glue width, the achievable deflection gets decreased as the overlap makes the whole actuating bender shorter. One advantage is that a higher glue-width can make the whole bender stiffer and result in a higher dynamic bandwidth.

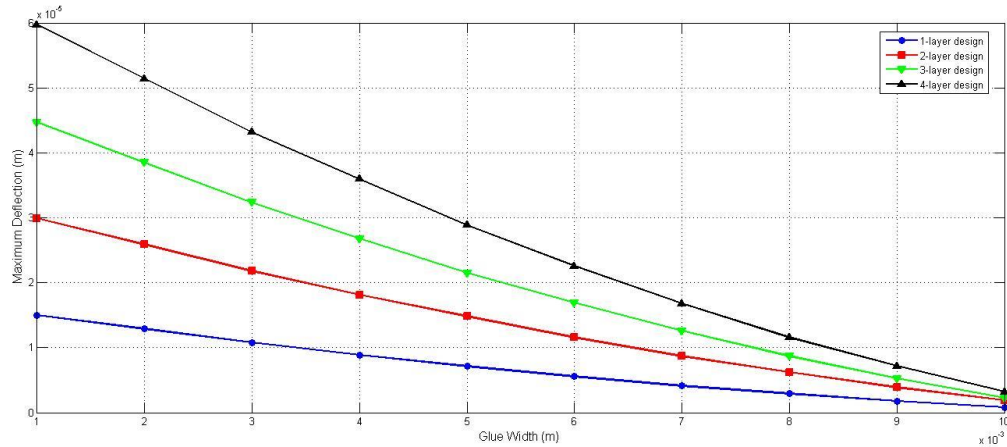


Figure 5.11, the influence of the glue width on maximum deflection of the platform.

5.4 Built-up Actuators

With CMBP02 as a basic structural unit, real piezo actuators were constructed according to the configurations shown in Table 5.1. The connections of the adjacent benders are achieved with superglue, which can be dissolved in the acetone solution. However, a drawback of this application is that the formed interspaces between two benders are quite small, which makes the permeation of the acetone solution quite difficult. Taking this into account, a long term "solution bath" might be needed. On the other hand, to eliminate potential vibrations in subsequent tests, the benders are devised to be built on a piece of metal substrate. Nonetheless, a direct connection between these two objects will cause unexpected charging problems when powering up the bimorph benders. For the insulation purpose, an additional polypropylene layer is applied between the metal plate and the benders. Choosing polypropylene as an ideal material relies on three effects: nonconductive, glueable and resistant to acetone. Although the 4-layer design is possible to deliver a large deflection (section 5.3), its bandwidth is quite low. With such consideration, only the 1-layer, 2-layer and 3-layer actuator were built and shown in Figure 5.13.

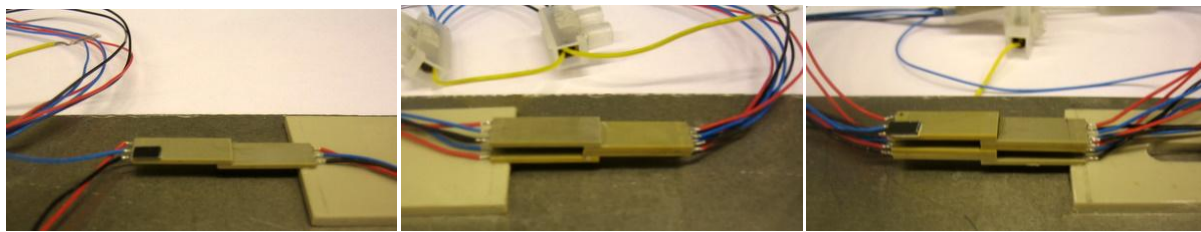


Figure 5.12, the built-up half actuators, from left to right, the 1-layer design, 2-layer design and the 3-layer design.

5.5 Measurement

5.5.1 Deflection measurement

With the established models shown in Figure 5.13, Measurement pertaining to the deflection is executed with the help of the White Light Interferometer. Additionally, we adopted reference planes for different samples in order to obtain the absolute deflection as shown in Figure 5.14. By giving different voltages, the relative distance between the bender end and the reference plane will change. As low energy consumption is always preferred for MEMS, hereby we only investigate the variations of the deflection within a voltage range of 0 to 30V. The obtained data are shown in Table 5.3 and further represented in Figure 5.15 to compare with the previous simulation.

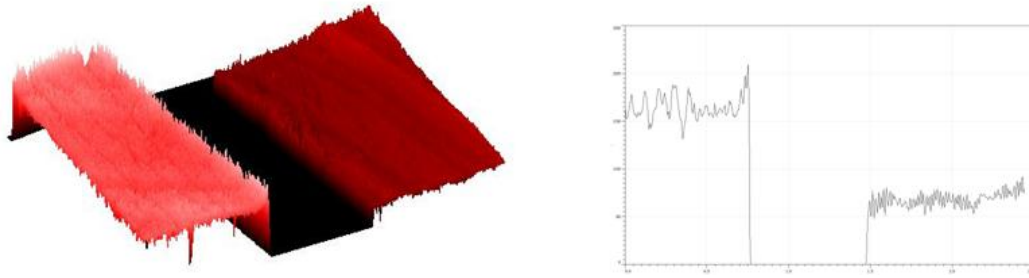


Figure 5.13, left) the height difference between the bender (pink) and the reference plane (dark red); right) 2 Dimensional representation of the height difference.

1-layer design		2-layer design		3-layer design	
voltage (V)	deflection(μm)	voltage (V)	deflection(μm)	voltage (V)	deflection(μm)
5.3	4.79	4	6.01	4.5	13.11
10.1	9.91	8.5	15.56	10.5	34.38
15.1	16.83	10.4	23.88	15.0	50.76
20.0	22.04	15.2	34.83	21.3	68.83
25.5	26.76	20.8	43.41	30.2	91.61
30.2	32.32	25.0	55.03	34.6	119.45

Table 5.3, deflection measurement with respect to different designs under different power inputs

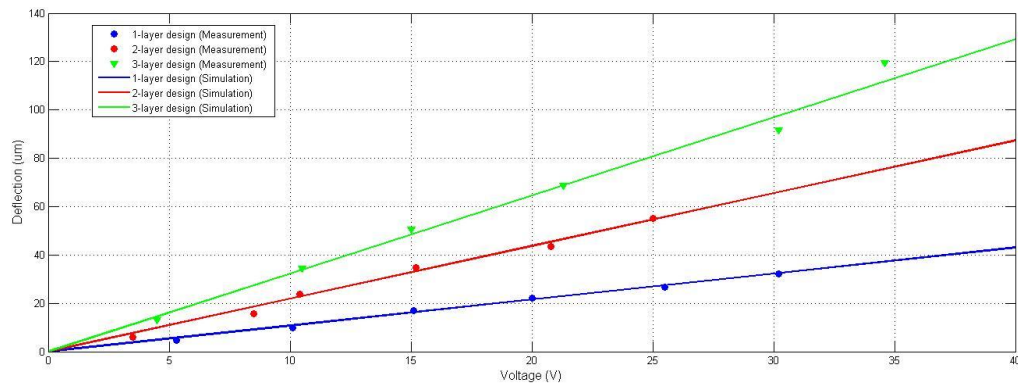


Figure 5.14, the deflection comparisons between the measurement and the previous simulation

From Figure 5.15, one could discover that although with small deviations, the measurement result shows almost the same trend as what is obtained from the simulation. This, on the other hand, proves that the voltage-deflection simulation in section 5.3.1 can be used as a reference for further actuator development.

5.5.2 Frequency Measurement

Additionally, dynamic analyses are also done by using the Laser Doppler Vibrometer introduced in Chapter 3. The obtained results with respect to different designs are exhibited in Figure 5.16. It can be read that the first resonance frequency with respect to the 1-layer, 2-layer and 3-layer design separately appears at 350Hz, 265Hz and 145Hz. This is more or less the same as the simulations in section 5.2.2. Furthermore, one could also notice that shapes of the dynamic responses and the corresponding frequency indexes are also similar to what we have in Figure 5.5, which confirms the accuracy of our simulations.

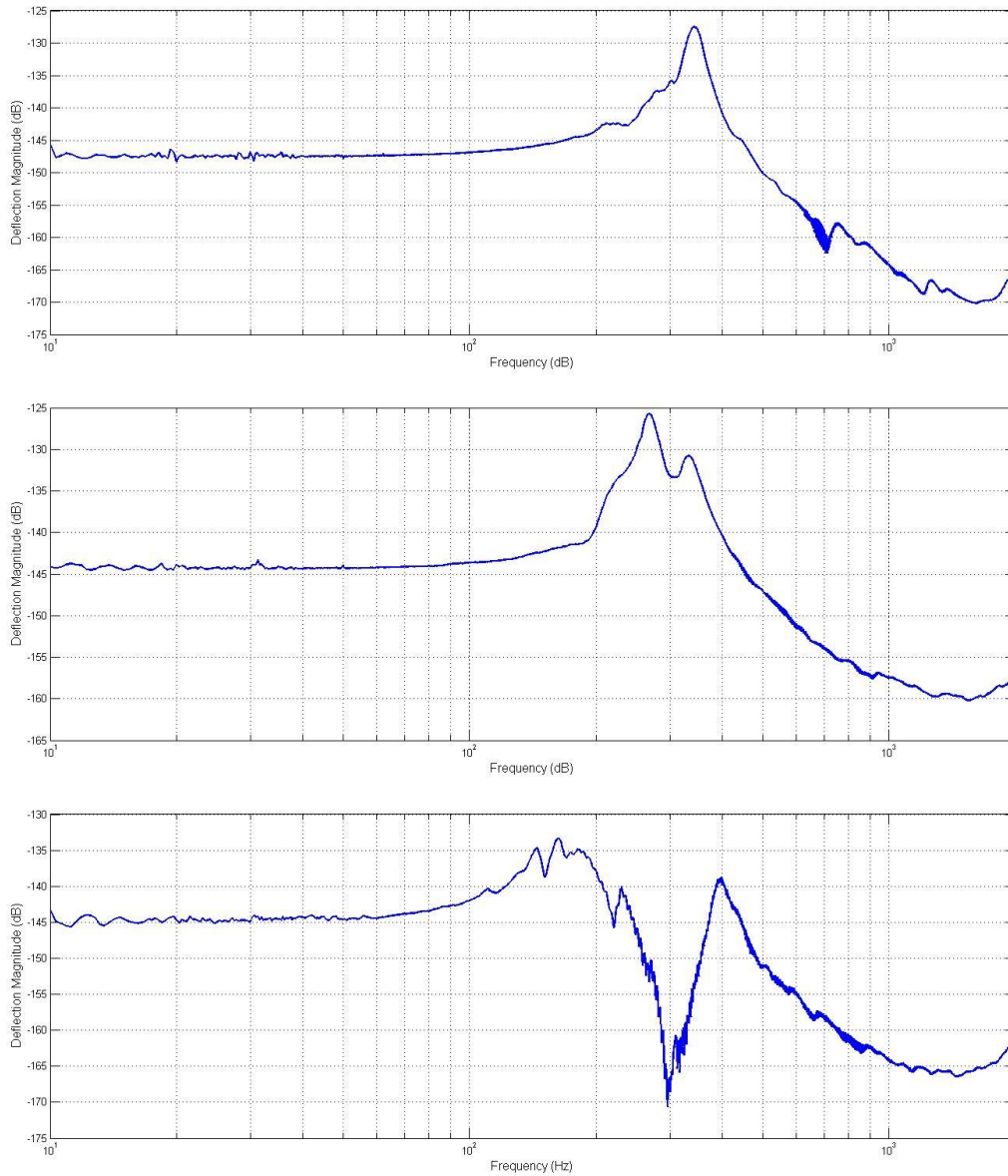


Figure 5. 15, the dynamic responses from the three actuators, from the top to the bottom are separately the responses from the 1-layer design, 2-layer design and the 3-layer design.

Conclusions and Recommendations

Intrigued by the MEMS device, the contents involved in this thesis concentrated on investigations of the actuators for different Nanite generations. It can be generally divided into two parts: the first part is focusing on the characterizations, including the dynamic analyses of the actuator in Nanite A and B, and the characterizations of the z actuator for the new Nanite generation. The second part lays particular stress on design, which aims at finding potential piezo actuation concept for the further generation development.

The characterization part

For the actuator in Nanite A and B, we managed to check how the three individual actuators react with respect to different axis inputs with the help of Laser Doppler Vibrometer. The obtained results comply with the electrical circuit provided by Nanosurf: for the x- and y-axis actuation, there are two actuators in motion, but with different amplitudes. For the z-axis actuation, all three actuators are activated, with two of them synchronized to achieve a small rotating movement. Furthermore, as the actuation along the cantilever's z axis is critical in providing depth information and its reliability directly influence the quality of the scan image, another experiment was conducted (perpendicular to the cantilever installation plane) to characterize its dynamic response. The obtained frequency spectrum exhibits a resonance frequency of about 205Hz.

For the z actuator used in the new Nanite generation, the magnetic field is non-uniformly distributed at coils with different diameters. We therefore simulated and obtained the intensity of the magnetic field at different coil locations to achieve a more precise estimation. Given the length of each individual coil ring, the net Lorentz force is calculated to be in the range of 0.0353N ~0.0597N. This is approximately 10 to 15 times larger than its own weights, which indicates that the z actuator has a good capability to actuate structure. Since linear actuators are highly expected for the chip driving, the deflection of the flexprint is measured as a function of the power input (given with an offset of 0V, the amplitude ranging from 0V to 1.4V) with the help of a high-resolution imaging system. The result shows that the deflection increases almost linearly to the power input, with an increase rate of about 15.8 $\mu\text{m}/\text{V}$. As a result, for a static current input (150mA), the generated deflection should be around 10.67 μm , which is more or less what the old actuator can achieve. Furthermore, assisted with the Laser Doppler Vibrometer, the dynamic response of the new z actuator is obtained, where the first resonance frequency presents to be approximately 1150 Hz. This value is much higher than the resonance frequency of the previous actuator, meaning that in the same situation, the z electromagnetic actuator can be operated with a high frequency signal and thus can achieve a high operating speed. On the other hand, to check the heat dissipation and compare the two flexprint designs (one with big bonding pads and the other is with small ones), we used the FLIR 315 thermal camera to identify their temperature distributions under a same static current input. The measurement shows that the maximum temperature always appears in the middle of the coils, and this maximum value for the design with small bonding pads is 5.5°C higher than the maximum temperature in the big-bonding-pad design (55.6°C). Considering the case that the actuator has functioned well during the deflection-voltage measurement, we would consider 60°C is a safe temperature. Furthermore, as the simulations suggest, the temperature span in the

small-pad case is much larger than the other design. All these phenomena indicate the size of the bonding pads does influence the temperature distribution over the flexprint. Big bonding pads are definitely beneficial for the system cooling and therefore recommended for practical applications.

The design and simulation part

Besides the characterizations mentioned above, some design activities are also involved. As piezoelectric materials have superior properties in MEMs actuating, we build a bimorph actuator, which should be capable of replacing the z electromagnetic actuator and can be applied for the further Nanite development. With simulations, the two potential concepts "half actuator" and "symmetric actuator" with different actuating layers are compared from different aspects, including the actuating stroke, the resonance frequency, the mass and volume, as well as the cost. From the comparisons, we know that the maximum stroke of the half actuator is always slightly higher than that of the corresponding symmetric design. This is because the integrated platform follows how the adjacent bender orientates, and because the bender end is not perfectly level during the actuation, it will induce an angular orientation on the platform as well. This eventually results in the slightly higher stroke value in comparison with the symmetric structures. Whereas it is worth noticing that the angle between the platform and the horizontal line is very small, only with a deflection difference of 68nm. For the symmetric actuators, a severe problem would be the platform deformation. During the actuation, the benders will exert forces on the edges of the platform, which not only activates the platform to move along the vertical direction, but also cause a stress along the horizontal direction. The resultant force makes the edges of the platform higher than the middle in the actuating process, and the whole platform appear in a "bowl" shape. For the 1-layer actuator design, this difference is about 860nm, meaning that if the cantilever chip is installed in the center, the platform edges might touch the sample first. This is not acceptable for a good actuating system, and is also the main reason for us to rule out this concept. Another problem for the symmetric actuator is that it is extremely difficult to ensure of the structure's "symmetry". Any unexpected deviations in the assembling process, such as the glue width and the control of the bender-bender overlap, may cause a big difference. Additionally, the half actuators also show significant advantages on the other aspects. For example, the mass, volume and even the cost, they all take half of what the symmetric actuators use. Therefore, we consider the half actuator as a potential concept to develop.

For the half actuator concept, we use COMSOL simulation to characterize the influencing factors on the maximum deflection with respect to different actuating layer designs. The deflection is found to be in proportion to the power input and proportional to the length squared, but inversely proportional to the overlap. To further verify the simulations, we built the actuators up and tested with experimental setups. The deflection was measured through a White Light Interferometer and by using the LDV, the dynamic responses were obtained. The resonance frequency with respect to the 1-layer, 2-layer and 3-layer design separately appears at 345Hz, 270Hz, and 150Hz. This is consistent with our expectation as increasing the actuating layer will simultaneously add mass to the actuating structure and thus reduce the resonance frequency. Besides, the measured frequency spectrums are more or less the same as our simulations, including the appearances of different eignemodes. Therefore, the simulations gave in this thesis can be used as a good reference for parameter selections in a further step. Based on a specified requirement, a good combination of different parameters (actuating layer, power input, bender length, overlap) can help achieve a large actuating stroke, a high resonance frequency, reliable actuating, a small mass, a condensed volume and a low cost. However, the influences from different parameters are not compatible, meaning that choosing one criterion in high index might scarify the other. Therefore, for practical applications, a careful consideration and good balance might be needed.

Compared to the electromagnetic actuator, the resonance frequencies of the bimorph actuators are low. However, since trimming the individual bender is possible and miniaturization is needed for further development, the resonance frequency will change in correspondence. Consider the case of cutting the bending beams shorter, 15mm for instance. The resonance frequency of the 1-layer design will go from 345Hz up to about 800Hz. This is because the stiffness of the actuating structure is enhanced, the mass on the other side goes low and the combination effect makes a higher resonance frequency. Considering this, the resonance frequency is not really a

problem for the piezo actuators. On the other hand, the maximum deflection can be achieved by choosing the right power input and bender overlap (according to the simulation diagram). One of the advantages of using piezo materials for actuation is because they normally possess low masses. This is one of the most important criteria for this application as the z actuator needs to be attached in the x-y platform, where a big mass will generate a huge influence on x- and y-axis scanning. Besides, the amount of heat generated with the piezo actuator is much less than that with the electromagnetic actuator. Stated thus, we conceive the half piezo actuator is a potential concept for the further development.

Challenges and recommendations

1. From the assembling point of view, it is important to control the overlaps between every two benders uniform such that the actuator can deliver an expected actuating stroke and resonance frequency. On the other hand, in the process of assembling, the benders and platform needs to be maintained horizontal, and parallel to each other, otherwise there will be an angular deviation imposed on the cantilever chip. Furthermore, to achieve a uniformed stress at every connection, it is highly suggested to keep the amount of glue the same everywhere.
2. 1. Since the buildup actuators in this thesis are only based on the original bender length. It is suggested to trim benders shorter, reassemble them, test and compare with Figure 5.11 to ensure the accuracy of the simulation. It is a necessary step for minimization.
3. As the wires for electrical connections coming from the side wall of each bender and they are pretty stiff, it is possible that these wires impose forces to the corresponding bender. To avoid this, it is vital to ensure that the wires are loss enough.

Bibliography

- [1] C. Bai, "Scanning Tunneling Microscopy and its Application", Springer Series in Surface Science, Berlin, pp. 62-77. 1994.
- [2] "Principle of Scanning Probe Microscope", http://www.physics.leidenuniv.nl/sections/cm/ip/group/Principle_of_SPM.htm.
- [3] C. Zhong, "A study of micro actuators for Scanning Probe Microscope applications", 2010.
- [4] S. Devasia, E. Eleftheriou, and S. O. R. Moheimani, "A survey of control issues in nanopositioning", IEEE Transactions on Control Systems Technology, vol. 15, no. 5, pp. 802–823, September 2007.
- [5] C. W. Shong, S. C. Haur and A. T. Wee, "Science at the Nanoscale - An Introductory Textbook", 2010.
- [6] R.A.Wilson and H.A. Bullen, "Introduction to Scanning Probe Microscopy (SPM)-Basic Theory ", July,2006
- [7] "Tip Surface Interaction", http://www.doitpoms.ac.uk/tlplib/afm/tip_surface_interaction.php.
- [8] "operating instrument Nanite B version 1.8".
- [9] "Crosstalk Eliminated (XE) Atomic Force Microscopy - New Generation AFM with Improved Scan Accuracy, Speed and Optics by Park Systems", Oct 26, 2009, http://www.parkafm.com/AFM_technology/technology.php.
- [10] "the common AFM modes", <http://www.chembio.uoguelph.ca/educmat/chm729/afm/details.htm>.
- [11] Piezoelectric Effect, PC in control, http://www.pc-control.co.uk/piezoelectric_effect.htm.
- [12] Piezoelectric effect, <http://www.physics.leidenuniv.nl/sections/cm/ip/Onderwijs/Scanning-Probe-Microscopy/Chapters/CHEN%20Chapter%20Piezoelectric%20scanner%20213-235.pdf>.
- [13] "Voice coil actuators in adaptive optics", <http://www.mvkonnik.info/2011/01/voice-coil-actuators-in-adaptive-optics.html>.
- [14] D. Parrat, "Atomic Force Microscopy for Characterizing Dust Particles of the Martian Arctic Soils", 2008.
- [15] D. Parrat, S. Gautsch, L. Howald, D. Brändlin-Müller, N. F. De Rooij and U. Staufer , "design and evaluation of a polyimide system for the scanning force microscope of the phoenix mars mission 2007", In Proceedings of the 11th European Space Mechanisms and Tribology Symposium, Lucerne, Switzerland, p 281–287. 2005.
- [16] "MSA-500 Micro System Analyzer- Measuring 3-D Dynamics and Topography of MEMS and Microstructures", Ploytec, <http://www.polytec.com>.
- [17] "basic principle of Vibrometry", Polytec, <http://www.polytec.com/eu/solutions/vibration-measurement/basic-principles-of-vibrometry/>.
- [18] "HF Transceiver Phase Noise", http://www.febo.com/pages/hf_phase_noise/.
- [19] A.F.Mills, "Basic heat and mass transfer ", second edition, 1999.
- [20] "Thermal conductivity", <http://hyperphysics.phy-astr.gsu.edu/hbase/tables/thrcn.html>.

<http://en.wikipedia.org/wiki/Gold>.

[21]"*FLIR IR Monitor-User's manual*", Chapter 13 the measurement formula, pp.75.

[22]"Technical support-CBMP-mount and connect", Noliac, 2008, www.noliac.com.

Appendices

Appendix A: Literature Review on the AFM Actuators

Abstract: *This appendix contains a study on the AFM actuators. It basically involves several different parts: First, it describes the actuating concepts that could be adopted for the cantilever chip driven. These concepts are formed on the basis of either piezoelectric effect or the electromagnetic effect. The combined concept is found to be quite intriguing for further development. Second, in weighing up whether an AFM actuator is good or not, some design criteria are listed, including the scan range, the scan speed, the resolution, and the actuation force. Additionally, problems and the corresponding solutions are summarized with respect to different actuating concepts.*

A.1 Introduction

A.1.1 Scanning Probe Microscope and Its Application

With extraordinary characteristics, Scanning Probe Microscope (SPM) is deemed as one of the foremost devices for industrial production and researches pertaining to small scale particles, and it is quite frequently utilized for observations of tiny objects and small range operations. Additionally, as found in previous researches, SPM can be brought into further applications aiming to manipulate micro and nano particles, because its probe can be used as a micro/nano manipulator (i.e. tweezers), rather than just being used for imaging, to establish contact with the targeted particles through adhesion forces that are strong enough to keep them stick together. Generally, SPMs can be grouped into two categories according to their working principles: one is the Scanning Tunneling Microscope, acronym for STM, which forms images by measuring the tunneling current between the probe and samples (thanks to the quantum effect) in order to infer the surface information; and the other one is Atomic Force Microscope (AFM), sometimes called Scanning Force Microscope(SFM), developed on the basis of the interactive forces--mainly the Van der Waals forces-- between atoms of the probe and the sample.

Because of the different principles they are working with, STM and AFM differ slightly in their practical usages. The general applications for STMs are listed below:

- (1) Image formation of surface structures with atomic resolution. Some examples are given in reference [1], including the images of Silicon, Aluminum, and Silicon Carbon.
- (2) Atomic manipulation and/or surface modification of the sample. Reference [2] demonstrates examples where STMs are used in vertical, lateral and combined ways to manipulate atoms or molecules.

One of the main impediments for STM is that it is only available to image or manipulate samples that are conductive as to form tunneling current for measurements, leaving those nonconductive samples undoable. On the other hand, as the AFM is built on the basis of the interactive forces, rather than the quantum tunneling currents, it opens the possibility to form images of non-conduct surfaces. For this reason, the applications of the AFMs are successfully extended to further areas like molecular biology in order to perform specific tasks, such as DNA and RNA analysis, cellular membranes manipulation, or handling of molecular crystals [3]. Although the STM is discarded for certain materials, its resolution however is quite high, with an approximation of 0.1 nm at x, y axis and 0.01nm at z axis in contrast with AFM's 2 to 10 nm at x-y plane and 0.1 nm in z direction [4].

A.1.2 SPM Actuator/Scanner

In general, there are two different scanning mechanisms that are mostly employed in today's commercial microscope designs: the sample stage based scanning (as seen in figure 1.1, left) and the tip/cantilever based

scanning (as seen in figure 1.1, right) [5]. The design of the scanning motion in the left is performed by a sample stage that is fixed on a 3-DOF actuator, which can timely gain scanning information from the image device, make adjustments according to the feedback signal and move to the next scanning point for scanning dimension expansion. In this case, the tip almost maintains its x and y coordinate as constants, while it is still possible to execute oscillations along z direction based on different operation modes, such as noncontact mode, intermediate mode. This scanning mechanism is more preferred in the AFM systems to measure the relative displacement between the cantilever and the reference surface in practical applications. The reason behind this scene relies on the fact that the mechanism shown in the right of figure 1.1 may easily cause unexpected vibrations of the cantilever, as it is somehow bounded onto the XYZ actuator and together moves in the process of scanning [6]. The scanning approach showed in Figure 1.1 right is normally utilized in STM applications, where the scan motions are only fulfilled by the cantilever which is further attached on and activated by a xyz actuator, leaving the sample stage stably fixed at the bottom without any movement. In other words, the cantilever needs to move in all three dimensions to obtain sufficient information from the sample surface for spatial image reconstructions.

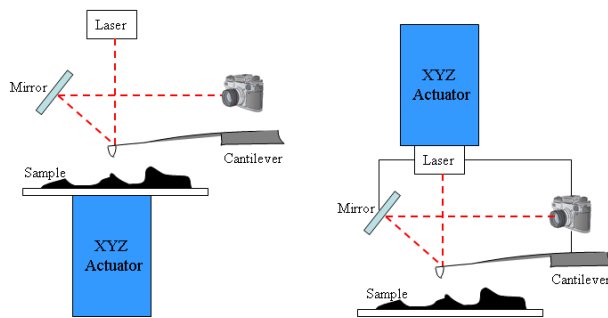


Figure 1. 1, scanning mechanisms: sample stage based scanning (left) and tip/cantilever based scanning (right)

However, it can be easily observed that no matter what mechanism is chosen, the actuator is always an indispensable part to achieve scan motions for imaging purposes or for manipulations, and in fact, the characteristics of an actuator are critical elements to determine how well a SPM can perform in a certain circumstance and what kind of compensating control algorithms are needed, as well as to confine the limitations of the SPMs applications.

It is important to mention that there are two different governing effects that contribute to the construction of the SPM actuators: the piezoelectric effect and the electromagnetic effect. Since the appearance of the first piezo actuator, various SPM actuator concepts have been and being tried to consummate the actuation process. As will be seen in chapter 2, some of these concepts will be demonstrated, in particular for the two SPM actuators previously mentioned: piezoelectric tube actuator and voice coil actuator, which have been admitted and widely employed in today's commercial products. Therein, one can find explanations regarding the piezoelectric and electromagnetic effect, lists of piezoelectric materials, and principles of how these two different concepts work.

In order to evaluate the performances of the different SPM actuators, Chapter 3 will illustrate some general criteria, including the scan speed, scan range and resolution, among others, to quantitatively indicate the compatibilities of a SPM actuator. Understanding the meanings of the different criteria and comprehending the relationships that exist in between, represent the key points for an improved assistance for designer, in order to ensure the pivot of his design and help users to select a high performance SPM according to the specific requirements.

Although the current SPM actuators can already provide comparable convincing results, various problems of SPM actuators are still gradually exposed, which is not acceptable for high accurate demanding cases. Based on this situation, problems respect to the piezoelectric tube actuator and the voice coil actuator are separately demonstrated in Chapter 4, combined with the possible solutions that could be found in recently published papers.

A.2 Actuator Concepts

A.2.1 Piezoelectric tube actuator

A.2.1.1 Piezoelectric effect

As introduced in several amounts of papers and reports, the piezoelectric effect, developed in 1880 by Jacques and Pierre Curie, has drawn significant attention in the past few decades for its actuator applications, and has been extensively utilized in multiple areas, such as mechanical engineering, biosciences, etc. The interpretations of the piezoelectric effect include two parts: the direct piezoelectric effect and the inverse piezoelectric effect. The former effect happens when a piece of piezo material (neutral) is subject to mechanical stresses, giving as a result the generation of an electric signal. This force-to-electricity transmission can be explained by the illustrations shown in Figure 2.1 where the red and gray spheres represent the different atoms carrying either a positive or a negative charge. Before any tensile force is applied, all the atoms in the cubic lattice are symmetrically distributed (as depicted in Figure 2.1 left), and the whole structure is in an equilibrium state and manifests to be neutral. However, when an external force pair is imposed on the lattice structure (as shown in Figure 2.1 right), the relative distances between the different atoms will change correspondingly, resulting in an asymmetric distribution of the atoms, which makes the lattice structure electrified. It is worth noticing that the tension and compression produce polarities with different signs, with their values proportional to the applied forces. By such explanation, the opposite of this relationship could be also confirmed: if one of these voltage-generating lattices is exposed to an electric field, it will elongate or get shortened as an effect of the polarity of the electric field, with its deflection proportional to the field strength [7].

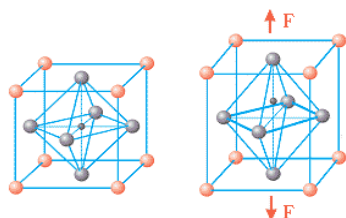


Figure 2.1. atom distributions in a piezoelectric cubic lattice, before (left) and after (right) force treatment

A.2.1.2 Piezoelectric materials

No matter if it is the case of a direct or inverse piezoelectric effect, the application of piezoelectric materials is a fundamental condition. In nature, there are some materials that already contain piezoelectric properties such as quartz, topaz and some biological materials like bones and silks. However, these materials are barely used as their piezoelectricities are quite weak and insufficient to provide enough signals for detections and processing. Consequently, many efforts have been made to investigate new piezoelectric materials which can not only give good performances in practical usages against nonlinear effects, such as hysteresis, creep, but also possess other qualities like low cost or ease-for-manufacturing. In this course, the emergences of metal oxide-based piezoelectric ceramics and other man - made materials enable the employment of the piezoelectric effect in many new engineering fields, and these materials can be normally classified into two groups: crystals and ceramics. The available crystals in today's market include quartz (SiO_2), Berlinite (AlPO_4), gallium orthophosphate (GaPO_4) and Turmaline. For ceramics, barium Titanate (BaTiO_3) and lead Zirconate Titanate (PZT) are more commonly used in practical applications. Therein, the PZT is the most preferable piezo materials so far for both commercial developments and academic researches as it exhibits greater sensitivity and higher operating temperatures compared to ceramics of other compositions. Additionally, some other materials, such as zinc oxide (ZnO) or polyvinylidene fluoride (PVDF) are also engaged in some specific applications [8].

The intrinsic difference between ceramics and other piezoelectric materials is that a ceramic must undergo a poling procedure [9] to have its piezoelectric characteristic activated before putting it into practice, as dipoles in a ceramic piece are initially randomly located as showed in Figure 2.2 (a). The piezoelectric effect presents only if all

the dipoles in the lattice are aligned in the same direction, roughly at least. The poling process is to help realign the orientations of the dipoles inside, and it is fulfilled by heating the ceramic just below its Curie temperature, applying an electric field to orient the dipoles as shown in Figure 2.2 (b), and finally followed by a short term cooling process. With such treatments, the survived dipoles will roughly align in the same direction as depicted in Figure 2.2 (c) and the material will eventually exhibit piezoelectricity. However, if at this point a strong electric field is imposed in the direction reversed to the poling direction; this piezoelectric property will be altered, and even dismissed depending on the intensity of the electric field [10].

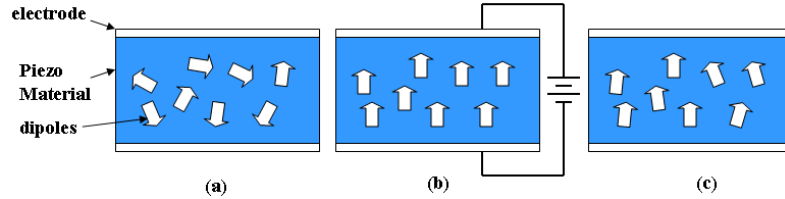


Figure 2.2, the poling process: (a) ceramics before treatment with random aligned dipoles; (b) ceramics in poling procedure (heating and electric field); (c) ceramics after treatment with its dipoles roughly aligned.

A.2.1.3 Constitutive equations for PZT material

Although the descriptions in section 2.1.1 literally explain how mechanical stresses generates electrical signals and its reverse effect, it is, however quite difficult to get any quantitative information to predict how much mechanical force can be exerted under the control of a certain electrical signal and how much deflection can be obtained at the same time; all these information are imperative for the design process. Hereby, mathematic calculations, known as material constitutive equations are presented to describe the relations among different parameters that are related to the piezoelectric effect, and how they interact with each other [11] [12]. The concrete descriptions in the **strain charge form** are listed below.

$$\begin{cases} S = s_E \cdot T - d^t \cdot E \\ D = d \cdot T + \epsilon_T \cdot E \end{cases} \quad (1)$$

The equations above can be further transformed and expressed in the **stress charge form**:

$$\begin{cases} T = c_E \cdot S - e^T \cdot E \\ D = e \cdot S + \epsilon_s \cdot E \end{cases} \quad (2)$$

Where T and S are sets of the material stress and the strain components separately, and both are 6x1 matrixes; D and E stand for the electric displacement and the field intensity, both being 3x1 matrixes; s_E (6x6 matrix) is the compliance coefficient of the piezoelectric material and c_E (6x6 matrix) is the mechanical stiffness coefficient under constant electric filed; ϵ , a 3x3 matrix, represents the electric permittivity; d and e are piezoelectric coupling coefficients, with the former one being correspond to the strain charge form and often referred to as piezoelectric stain coefficient, and the latter one for Stress-Charge form and also mentioned as piezoelectric stress coefficient. As parameters in above equations are all vectors and matrix constructed, it is important to figure out the orientation of every vector in order to properly calculate the targeted element, and for the sake of ease, the Cartesian coordinate system is brought in and different orientations in the standard convention are marked in Figure 2.3. Detailed information about Cartesian coordinate system can be found in reference [13].

The constitutive equations (1), (2) are sufficient to tackle the problems in complicated situations, such as multiple inputs or coupling effects. However, for simple cases, one could actually use a simplified formula as given in equation (3) to approximately appraise the corresponding deflections.

$$\Delta L = Ed_{ij}L \quad (3)$$

Where E is the intensity of the electric field, L stands for the original length of material, d_{ij} is the piezoelectric stress coefficient, the subscript i indicates the direction of the applied voltage and j is the elongation direction of material according to the Cartesian coordinate system.

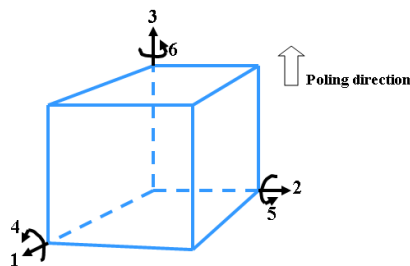


Figure 2.3. the Cartesian coordinate system

A.2.1.4 Configurations

Since the advent of the first SPM actuator, different concepts, mostly based on the piezoelectric effect, have been conceived and developed. Initially, the scan motions in SPM instruments are predominantly achieved by the tripod actuator, which is simply constructed with three independent cuboid piezoelectric bars perpendicularly connected to each other as shown in figure 2.4. On every signal bar, there are metal layers deposited on a pair of opposite side to act as electrodes for electrical signal input, and the tip is fixed at the point where the three bars intersect with each other. As the bars are available to fulfill expansions and contractions as in the case that they work separately; this concept can eventually yield 3 translation degrees of freedom [10].

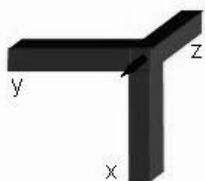


Figure 2.4. general configuration of a tripod actuator with three piezo bars mutually perpendicularly aligned

To estimate the deflections along different axes regarding an input voltage V , a simple mathematic equation is developed in equation (4), with L being the length of the bar, h the thickness and d the piezoelectric strain coefficient. The subscript i still indicates the direction of the applied voltage, and j indicates the material elongation direction, both of which can be cleared up by checking the Cartesian coordinate system. With the obtained subscripts, one can easily find the index of the corresponding strain coefficient from the material property database.

$$\Delta x = d_{ij} V \frac{L}{h} \quad (4)$$

However, one of the problems with this design is that the piezo bars are quite flexible and can easily get interfered by signals from outside, such as mechanical vibrations or noises, which are critical detrimental elements that could impair the performances of SPMs. Moreover, the cross-coupling effect, namely the motion interactions between different axes (detailed in section 4.1.6), is also striking with this structure and hence can probably lead to devastating distortions in the scanning images.

On top of the tripod structure, bimorph actuators, as depicted in Figure 2.5, are proceeded to achieve a larger scan range. As shown in the illustration, there are two concepts sharing almost the same configuration--two metalized piezo plates glued together--except for the electrical connections. The series bimorph on the left can be interpreted as one piezo plate with double thickness since it has only two outer electrodes as input. The parallel bimorph showed on the right is more commonly used in various researches, and it has three interfaces for electrical connections: the two outer electrodes are in general grounded, while the central metal is supplied with an electrical potential. With such arrangement, one of the plates will expand owing to the piezoelectric effect, while the other plate as given an opposite voltage will get contracted. As such, the actuation force and scanning range can be doubled. However, a drawback of this bimorph design is that it gives few accesses for multidimensional actuations. Even if that is possible as indicated in some papers, the designs are either too complicated for fabrication or too susceptible to noises, which are normally addressed by massive and intricate

control algorithms.

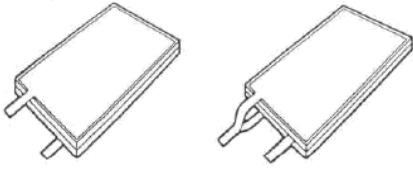


Figure 2.5, bimorph actuator: series bimorph (left) and parallel bimorph (right) [10]

After that, the piezoelectric tube actuator, with high position accuracy and large bandwidth, is investigated, and it is still extensively employed in today's SPM systems for various applications related to Nano positioning as reported in reference [10][11][14][15] and [16]. The tube configuration normally takes the same form as the one shown in Figure 2.6, where the piezoelectric material is fabricated in a tubular shape, usually with 7 to 9um thickness. This tube is radially polarized and deposited with thin metal (either silver or copper) layers on its internal and external walls to serve as electrodes for electrical signal inputs, with the internal wall covered by an entire piece of metal layer, denoted as z, and the external wall coated and symmetrically segmented into four quadrants, separately noted as +x, -x, +y, -y.

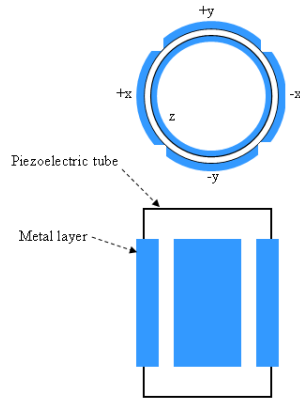


Figure 2.6, general configuration of a piezoelectric tube.

With one of the ends fixed, the tube scanner commits its motions in the x, y plane by producing a structure bending. In fact, the trajectory of the flexible end should in principle form an arc. However, since the motions are quite small, usually ranging from a few angstroms to at most 100nm, the small deflections along z axis can be neglected, which leads to linear approximations about the motions along x and y axis. As shown in figure 2.7, the actuation along x (or y) axis can be simply achieved by applying voltage on the x-x (or y-y) electrode pair, leaving the inner electrode grounded. However, for motions along z axis, it is often accomplished by connecting one terminal of a voltage source to the internal electrode, and the other terminal to one of the external electrodes.

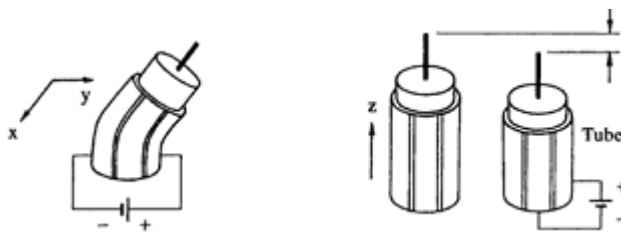


Figure 2.7, actuation methods along x (or y) axis (left) and along z axis (right) [9]

For experimental setups, a jig, which functionalizes as the SPM frame, is usually employed to stably hold one side of the piezoelectric tube, with the other end flexible, and banded with a small aluminum cub (shown in figure 2.8),

which could represent either the platform where the cantilever/tip should be mounted or the seat for sample alignment depending on the scan mechanisms. To timely gain the information of the tube deflection, a capacitive sensor head is deployed facing to the aluminum cube to measure the cube deflections at the corresponding direction as shown in Figure 2.8. In this situation, whenever a deflection occurs, the distance between the cube and the capacitive sensor will change and induce a variation of the capacitance, which can be measured and sent to the outside signal processing unit for further treatments. Note that it is still possible to measure the deflections along its perpendicular direction by simply fixing another external sensor along that axis.

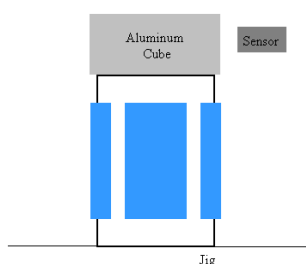


Figure 2.8, piezo tube with Aluminum cube banded on its top and sensors to measure the deflections

When performing a raster scan, the actuator traces back and forth in the x-direction repeatedly, while slowly increasing its position in the y-direction (as shown in Figure 2.9), which is slightly different from the rational principle described above. A common experience to form such a trajectory is by applying a triangular waveform to the x electrode, and at the same time imposing a “very slowly” increasing ramp signal to the y electrode. Quite frequently, this ramp signal for y+ electrode is either replaced by a dc signal or assumed to be earthed or open circuited [11][15][16][17].

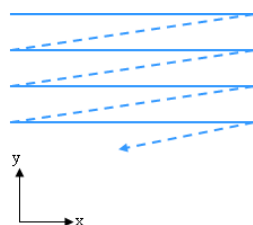


Figure 2.9, raster scan pattern

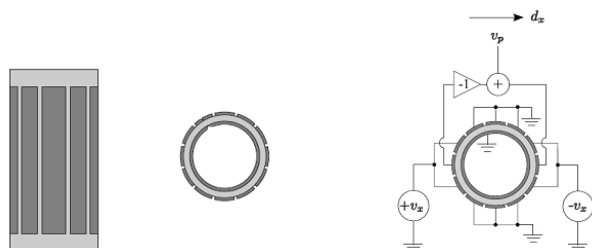


Figure 2.10, tube scanner with new segment pattern (left) and electric connection (right) [18]

Other than the general configuration, there are some similar designs that have been developed to optimize the tube performances. As explained in reference [18], a new segment pattern is considered in order to have symmetric stresses on the bending structure, and to amplify signals in order to have a large scan signal. This new tube configuration is shown in Figure 2.10. As can be observed, the outer electrode in this design is segmented into 12 equal sectors of 30° each, and three pairs of opposite electrodes are applied for actuations, with the voltage on the opposite sides equal in magnitude, but 180° out of phase. The testing result manifests the effectiveness of this new structure with a larger displacement range and a strain-induced voltage when compared to the 4-sector solution (under same conditions).

In general, for a single piezo slice, the maximum elongation or contraction is approximately one tenth of its original height [19], which eliminates its applications from large-scan-range demanding processes. To improve this situation and to reduce the power consumption, a multilayer concept developed by gluing thin layers of piezo units together to form a stack is shown in figure 2.11 left, where the circuit is arranged as three paralleled bimorphs serially connected to each other. There is no doubt that this kind of design could perform a larger scan range, as the displacement of the stack is an accumulation of the deflection generated on every single piezo slice. Depending on the desired scan range, numbers of slices can be appropriately chosen and glued to accomplish a specific task. However, the control of such a structure is not as easy as it appears, especially for cases that call for fast scanning and high precision. Consequently, very complicated op amp systems are needed. Reference [19] provides three different control algorithms to tackle this problem, including the drive circuit, bridge connected circuit and high speed drive circuit.

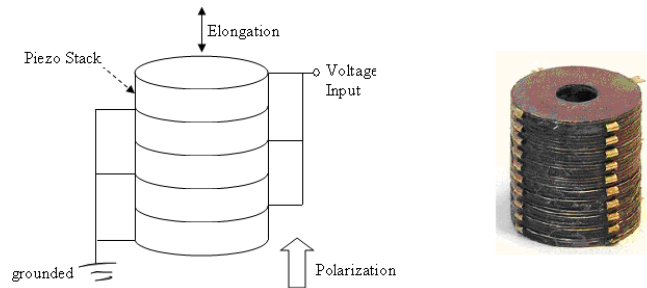


Figure 2.11, the concept of piezo stack (left) and an example of commercial products (right)

Despite that a piezoelectric tube actuator is capable of providing a rather high resolution and a wide servo bandwidth, its application is hindered due to the fact that it can not render a sufficient scan range for some particular cases. Besides that, the designs of the controllers for piezoelectric tubes with different dimensions usually differ from each other on the parameter selections, which might lead to ascensions of the actuator price. Additionally, dozens of problems, as discussed in section 4, have been encountered in forepassed applications. To open new perspectives and new directions, an actuation technique by using electromagnetic effect has captivated a great deal of attention in recent years, and has been well conceived and exploited in SPM developments. Therein, the most successful commercial products are produced by Nanosurf AG and their outstanding performances have been widely recognized. As this kind of actuator shares the same working principle as loudspeakers, it is quite frequently referred to as Voice Coil actuator or Voice Coil Motor (VCM), with its detailed information demonstrated in section 2.2.

A.2.2. Voice coil actuators

A.2.2.1 Basic principle

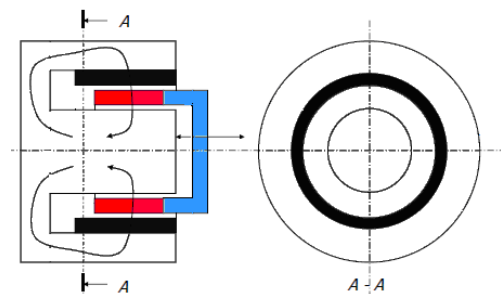


Figure 2.12, one of the configuration designs for the Voice Coil Actuator [20]

As one of the four fundamental interactions in nature, electromagnetism, describes the relations between electric fields and magnetic fields: a changing electric field generates a magnetic field, and analogously, a changing magnetic field will inversely generate an electric field. As a consequence, when placing a live conducting wire in

the field of a magnet, one can observe that the wire actually moves, instead of standing still, which is caused by the exerted Lorentz force. This is exactly the working principle for the voice coil actuator. On the other hand, as for different applications, the structures of VCMs can take various forms, among which the most well-known configuration is the one for loudspeakers as depicted in Figure 2.12.

In the sketch shown in figure 2.1.2, the black part represents a tubular permanent magnet that can generate a stable magnetic field, and the white structure symbolizes the frame used to fasten the magnet and is usually made of ferromagnetic materials for the purpose of collecting flux lines. To have the electromagnetic effect, coils (red) are applied and wound around a blue support. Considering different requirements and designs, one of the support structures--either the white one or the blue-- should be fixed in general conditions, with the other part flexible enough to implement locomotion. Once the coils are electrified, Lorentz force will be immediately generated and act in between, which will facilitate the flexible structure moving relatively along the axial direction. More information about different forms of VCMs and the course of their evolutions can be found in reference [20].

A.2.2.2 VCM scanning principle

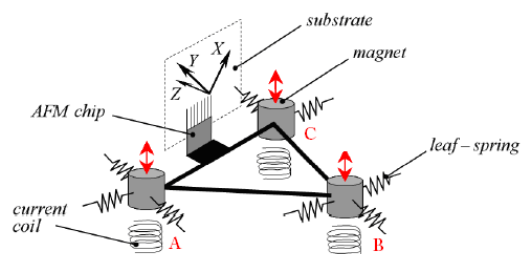


Figure 2.13. the 3 DOF Voice Coil actuator concept for SPM application [21] [22]

To expand the use of voice coil actuator into the field of SPM application, three magnet-coil pairs (as shown in Figure 2.12) are employed to realize 3-DOF actuations and arranged in a triangle shape as illustrated in Figure 2.13. As can be observed from the sketch, three permanent magnets are attached to a spring suspended platform which acts as the movable structure, and underneath of each magnet, a group of windings is rigidly attached to the outside structure. By driving current through, electromagnetic forces will be exerted and prompt motions of the magnets. The exerted forces will further balance with the resorting force of the lead springs to achieve stable performances [21] [22]. By actuating single or multiple of the coil-magnet pairs (A, B and C), one can achieve corresponding motions along axes of the coordinate system denoted in Figure 2.13.

A.2.3 Other concepts

Besides the two popular configurations mentioned above, other concepts have also been developed in the last decade to seek for better actuation performances of the SPMs. In this section, several concepts constructed pertaining to either the piezoelectric effect or the electromagnetic effect, are to be demonstrated to show the configuration possibilities of SPM actuators.

One of the successful concepts on the basis of piezoelectric actuation is first brought forward by Schitter et al. in 2007 by making use of five piezoelectric blocks to realize 3 dimensional motions. The arrangement of the blocks in company with a simplified feedback scheme is depicted in Figure 2.14, where one can easily discover that two pairs of piezo blocks are separately mounted in cavities of the platform to fulfill the in-plane motions, and a small piece of piezoelectric material is employed and allocated on top of the middle structure to proceed z-axis movements by expansions and contractions under controls of the feedback algorithm. Care should be taken to indicate that series of paralleled hinges, also referred to as flexures or compliant structures, are furnished between the actuation blocks and the central platform along both x and y axis. Employing such structures endows the system with great abilities to perform stable as the generated elastic deformations can provide sufficient stiffness to eliminate unexpected nonlinear effects.

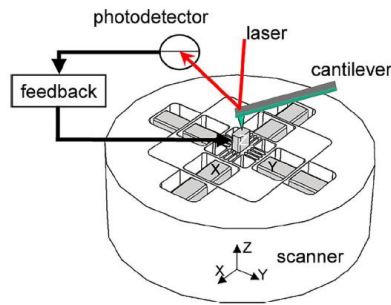


Figure 2.14, actuator concept developed with 5 piezo blocks for SPM application [23]

Similarly, Yong et al. recommended a 2 DOF (x-axis and y-axis translation) design with inverse piezoelectric effect to optimize actuations at high operation speed. The design model is given in Figure 2.15, with two piezoelectric blocks (marked with PZT) perpendicularly aligned to yield actuations along both x and y axis. The highlight of this design is that a special constructed platform consisting of four pairs of paralleled flexures along each axis are adopted. The symmetrically located flexures make the actuation structure quite rigid in the direction of actuation, but flexible at its perpendicular direction [24]. This will eventually lead to a high resonance frequency in system dynamic response, and allows the actuator executing tasks in high speed demanding cases without initiating problems like vibrations, cross-couplings that most tube actuators need to confront with.

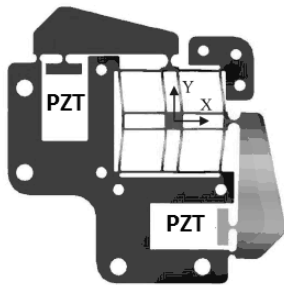


Figure 2.15, a 2-DOF piezo actuator for high speed scanning [24]

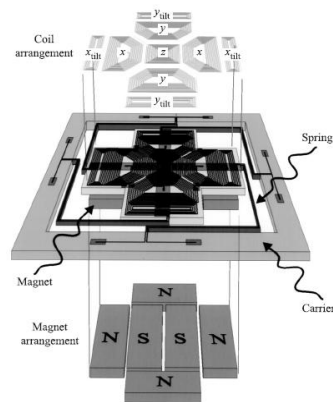


Figure 2.16, actuator for "millipede" for AFM data storage [25]

Exploiting the electromagnetic effect gives other accesses to achieve multidimensional actuations in SPM systems. In 2000, Vettiger et al. came up with the concept of "Millipede" for further AFM data storage, with its actuations achieved by VCMs in all three dimensions. A scheme of this actuation system is given in Figure 2.16, where the arrangements of the coils and magnets are expressed separately above and below the main structure. In this design, the coils are attached to a flexible platform which is further connected through lead springs to the carrier

[25] [26]. By power supply to different coil- magnetic pairs, motions along different axes can be performed.

In practical applications, one of the issues for voice coil actuators is the insufficient damping, which makes the structure quite susceptible to the environments, therefore things like vibrations may easily occur due to external disturbances. And in order to address this problem, in 2007, Engelen et al. from IBM conceived to use special leveraged flexures to provide sufficient stiffness to increase system rigidness. A simple illustration shown in Figure 2.17 (left) gives explicit explanations of how this concept works. For SPM applications, two branches of such structure are employed and arranged in perpendicular to each other to realize x, y scanning motions. With commercial product design, the layout is slightly rearranged to have a condensed structure as shown in Figure 2.17 (right), where the actuation is proceeded through pivot springs first and then onto the "Table"[27][28].

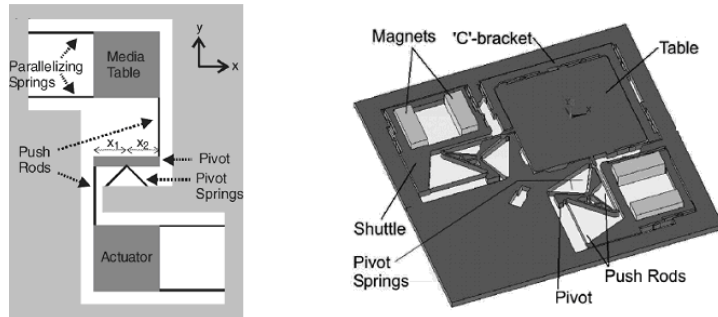


Figure 2.17, principle of motions along one axis (left) and real design with 2 DOF (right) [27]

A.3 Performance Criteria

Since various actuators have been developed for SPM scanning, it is vital to know what kind of actuator gives better performances under certain conditions and what makes it possess such quality. For this reason, different criteria are demonstrated in this chapter to help to evaluate actuator performances. Understanding the meanings of different criteria and grasping the corresponding correlations can provide designers enough evidences to work with, in case some improvements are needed, and better help customers choose a desired device according to specific requirements.

Since this report dedicates on descriptions of the piezoelectric tube actuators and the voice coil actuators, and considering the current lab situations, two specific actuators are chosen to demonstrate the differences in between when comparisons are needed. The selected model for piezoelectric tube actuators is the “scanning by sample” actuator for NTEGRA Prima which is produced by the NT-MDT Co., and the model for voice coil actuators is the “large scan” scan head for “Nanite B” that was developed by Nanosurf AG, as both of them have almost the same maximum scan range along x and y axis, with the former one of 105um and later one of 110um.

A.3.1 Scan Range

Scan range, as its name suggests, is a measure of the maximum scan area that an actuator can achieve. In general, the larger scan range an actuator has, the more comprehensive information (about the sample) it can obtain.

In reference [29], Howland and Benatar mentioned: “The maximum scan size that can be achieved with a piezoelectric tube actuator depends upon the length of the scanner tube, the diameter of the tube, its wall thickness, and the strain coefficients of the particular piezoelectric ceramic from which it is fabricated. Typically, SPMs use scanners that can scan laterally from tens of angstroms to over 100 microns, and in the vertical direction, SPM scanners can distinguish height variations from the sub-angstrom range to about 10 microns.” To approximately estimate the scan range of a particular tube structure, reference [11] [17] [30] provide two expressions separately for deflections in x/y and z axis:

Maximum tip deflections in lateral plane(x or y direction):

$$d_i = \frac{\sqrt{2}d_{31}L^2}{\pi Dh} v_i \quad (i = x, y) \quad (5)$$

And the maximum displacement in z direction:

$$\Delta L = \frac{2d_{31}L}{h} v \quad (6)$$

Where d_i is the maximum deflection along x or y direction, d_{31} is the piezoelectric strain constant, L is the length of the tube, D is the outside diameter, h is the tube thickness along radial direction, and v_i is the voltage applied in x or y axis.

For the chosen models with a same x/y scan range in the order of 100um, the scan head for NTEGRA Prima can achieve a maximum scan range of about 10um on z axis, whereas the scan head for Nanite B can reach a value up to 22 um, more than twice of the former one, meaning that the Nanite B actuator is capable of scanning rough surfaces and provide sufficient depth information for microscope image construction.

A.3.2 Resolution

Resolution for SPM actuators can be generally interpreted as the smallest step that an actuator can make in the process of scanning. In general, a small resolution contributes to detailed information and high

quality scanning images. For the Nanite B actuator, according to the technical parameters listed in the product brochure, the achievable x/y drive resolution is 1.7 nm and the resolution along z axis is about 0.34nm. But no specific numbers can be found in describing the resolutions of the NTEGRA Prima actuator. However, as remarked in reference [20], a piezoelectric actuator with a dynamic range of about 10 microns has a resolution of less than 0.5 nm, which is almost 1/20000 of the scan range in its corresponding direction. Hence it is reasonable to infer that the NTEGRA Prima with an x/y scan range of 100um and a z scan range of about 10 um may achieve a resolution of a few nanometers in the x, y direction, and an angstrom resolution in the z direction.

A.3.3 Scan speed

Scan speed is an indication of how fast a scanner can be operated during the scanning processes. Generally, this value can be predefined or selected before executions of the tasks, as long as it is set less or equal to the maximum scan speed the system can endure. It is obvious that actuators working with high speed can reduce the time costs on scanning. However, as one can find in the subsequent explanations, this criterion is actually a co-determinant, meaning that the variations of the scan speed might impact the other aspects, such as the bandwidth indicated in section 3.7, the precision and scan size accounted in section 4.1.5. Thus, changes of the other criteria will also impose influences on the scan speed.

A.3.4 Actuation force

The Actuation force indicates the maximum force that can be generated by the SPM actuators in order to proceed the scanning motions. In general, a large actuation force implying a high acceleration will probably lead to a high scan speed. The index of this criterion mostly depends on the material selections (including materials for piezoelectric tube, metal layers for electrodes, magnets, and metal coils), the structure design (of the tube size, magnet dimensions, numbers of coil windings and structure layouts), as well as the input electrical signals. Acquaintances with these parameters combined with the appropriate selections can help designers devise actuators with compact structures whilst being capable of offering high actuation force.

A.3.5 Sample size

The sample size takes into consideration the maximum sample volume a SPM actuator can measure in the process of scanning. That is to say, for a certain Microscope, sample size exceeding the default “sample size” value can not be overall scanned, and thus the obtained scanning image can not reflect the monolithic information of the targeted sample. The maximum sample size that the NTEGRA Prima actuator can handle is in the order of 40 mm in diameter and 15mm in height, while the sample size for Nanite B actuator is unlimited.

A.3.6 Power consumption

Power consumption indicates quantities of power that are needed to maintain motions for a complete scanning process. In general, piezoelectric tube actuators are driven with voltage sources, and in standard SPM designs, scanning areas of several tens of micrometers usually ask for driving voltages of more than 100 V [31]. In practical applications, the preferred voltage source ranges from 200V to 1000V. Whereas the Nanite B actuator is usually driven by current source with ± 10 V to achieve a full scale scanning.

A.3.7 Bandwidth (BW)

Bandwidth is another criterion that highly influences the performances of the SPM actuators. The concept for bandwidth is slightly different within different areas. In radio communications, for example, bandwidth is the range of frequencies occupied by a modulated carrier wave, whereas in optics it is the width of an individual spectral line or the entire spectral range [32]. For signal processing, bandwidth, also called 3dB bandwidth, by convention refers to a frequency range, within which the power has

dropped 3 dB from its maximum value, as shown in Figure 3.1.

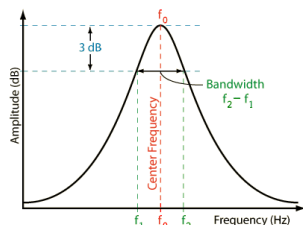


Figure 3.1, bandwidth in dynamic response

Mathematic calculation of BW is given in equation (7)

$$BW = f_2 - f_1 = \frac{f_0}{Q} \quad (7)$$

Where f_1 and f_2 separately symbolize the lower and upper cross frequency; and f_0 represents the central frequency or resonance frequency as marked in Figure 3.1. Q is the quality factor which can be written as $Q=1/2\xi$ (ξ the damping ratio). By substituting Q in equation (7), BW can be reorganized as given in equation (8):

$$BW = \frac{f_0}{Q} = 2\xi f_0 \quad (8)$$

As equation (8) suggests, bandwidth is a function of the system damping and the central frequency of its dynamic response, and for a given f_0 , BW is indeed proportional to the damping ratio. Therefore, one may draw the conclusion that a structure with a low damping ratio may have a narrow bandwidth, meaning that the system is only affected by a small range of frequencies that located near to the resonance frequency and thus less sensitive to external disturbances compared to that working with a high damping ratio.

BW vs. scan speed

Scan speed is conditioned by the system bandwidth as a narrow bandwidth usually signifies a low operational frequency, meaning that more time is needed for the cantilever to switch from one position to another, and from one scanning line to the next [33], which gives the interpretation that scan speed is in proportional with BW .

BW vs. scan range

To perform a large scan range, piezoelectric tube actuators with large dimensions are usually preferred, resulting in actuators with comparable large masses. On the other hand, increasing of an actuator's mass will lead to a decrease of its resonance frequency based on the formula $\omega=\sqrt{k/m}$. In this case, even operations at low frequency might easily stir up vibrations and lead to system instability.

BW vs. Scan Precision

As indicated above, a system with a high bandwidth is quite sensitive and may vibrate easily due to external disturbances, resulting in an unstable system with low precision. In this way, BW can be interpreted to have an inverse proportional relation with the scan precision.

Most piezoelectric tubes used in STMs and AFMs have their first resonance frequency aligned within a bandwidth of 1-2 kHz, with minorities having their first resonance modes beyond that value [15]. In general, piezoelectric materials are quite susceptible to mechanical vibrations, especially when dealing with comparable high-frequency operations, which amounts to the available operational bandwidth of the system quite low, usually 0.01- 0.1 times lower than its first resonate frequency [34] [35]. In some high-precision demanding cases, such as soft sample scanning, the operational frequencies are further confined as low as 0.1 to 1 Hz [35].

For control and modeling purpose, it is important to know the resonance modes of a tube structure, especially its 1st resonance frequency. However, this value differs greatly as tubes normally process different dimensions to satisfy requirements. To have a rough estimation of the first resonance frequency of a tube, a formula is developed and demonstrated in equation (9):

$$f_r = 1.08 \times 10^5 l^{-2} \sqrt{r_o^2 + r_i^2} \quad (9)$$

Where r_i and r_o represent the radius of the inner and outer wall respectively, and l is the length of the tube in centimeter [9]. Because many resonance modes could appear with different driven frequencies as demonstrated in Figure 3.2, the concrete dynamic property of a tube is quite complicated and difficult to predict. To tackle this problem, in reference [14], System Identification is utilized to obtain a full dynamic response of a tube by inputting swept sine waves into the x+ electrode together with some auxiliary devices, with y+ electrode being earth. The problem with this method, however, is that the designer needs to prepare a new prototype every time when he changes the tube structure and the time taken for new measurements is marvelous. Reference [36] presents an extended modeling approach for modeling the dynamic response of the piezoelectric tube actuators by combining Finite Element Analysis (FEA) and model order reduction (MOR) techniques. Although this approach has the drawback of only available for simulations in low frequency domain, it does not influence the new structure designs and simulations as SPMs are normally operated at low frequencies in avoiding vibrations. For the Nanite B actuator, the resonance frequency does not appear in the product brochure, but according to the information provided by Nanosurf AG, the resonance value is in the order of 200Hz, which can be measurement by Doppler Vibrometers.

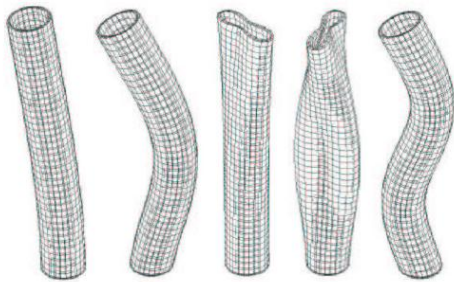


Figure 3. 2, 3D finite element mode shapes; from left to right: 1st longitudinal bending mode, 2nd longitudinal bending mode, 1st circumferential bending mode, 2nd circumferential bending mode, 3rd longitudinal bending mode [36]

Besides the criteria mentioned above, there are also other elements influencing the performance of an actuator. For example, the noise level describes whether an actuator is susceptible to disturbances from external environments, such as vibrations, noises; the linearity mean error reflects deviations in scanning images in comparison with the real sample surface. In addition, weight and cost are also critical parameters influencing the applications of different actuators in the market.

Note that although it is desirable to integrate all good qualities in one actuator, it is not possible to implement as some of the parameters do not coexist. This asks the designers to have a good sense of balancing different criteria according to specific requirements in order to have an optimized design.

A.4 Problems and solutions

The piezoelectric tube actuator has been applied in SPMs for years and widely expanded to various industrial fields thanks to its extraordinary imaging function. However, problems like mechanical vibrations or hysteresis have been constantly found in practical applications as shown in Figure 4.1, which to a certain extent eliminates applications of this actuator. On the other hand, for VCMs, fewer problems are found compared to the tube structure, probably due to its short term applications. In the following section, problems that related to both actuators are demonstrated, associated with some developed solutions.

A.4.1. Problems and solutions for Piezoelectric tube scanner

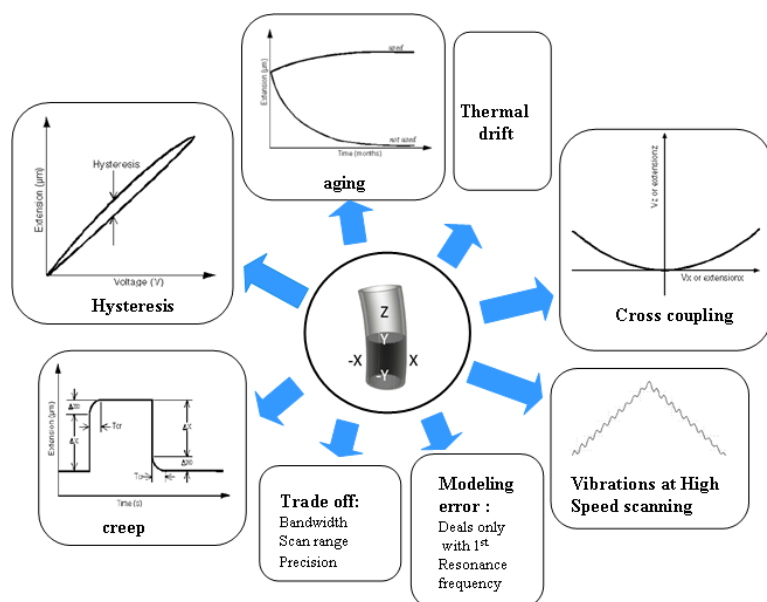


Figure 4.1, problems for the piezo tube actuator in SPM applications

A.4.1.1 Hysteresis

As in the case of magnetizing ferromagnetic materials [20], hysteresis also exists in the actuation process of a tubular piezoelectric actuator and has immense influences in the qualities of the scan images. This effect refers to the nonlinearity appears in the process of electrical signal application: applying a voltage source linearly increasing from 0 to a finite value to a piece of piezoelectric material and afterwards depressing this value down to null, the output performance of the tube in signal descending period actually differs from that in the signal ascending period, leading to the performance curve shaped like an ellipse as shown in Figure 4.2. The magnitude of the hysteresis effect is measured by the ratio of the maximum divergence of the two curves to the maximum extension that the tube created during the scanning process [29].

One of the main accounts for hysteresis lies on the fact that the orientations of the dipoles in a piezoelectric material will not stay constant as what they look like after the “poling process” treatment, and they will virtually be altered more or less in daily applications due to being exposed under electric field, which eventually results in variations of material properties, such as elastic strain constant, piezoelectric strain constant. Such changes make the actuator attempt to maintain the shape of what it used to be when subject to electrical applications, and consequently leading to a negative shaped nonlinearity when expanding and a positive shaped nonlinearity when contracting. Detailed information about hysteresis on both piezoelectric and ferroelectric materials, associated with the possible causations can be found in reference [37].

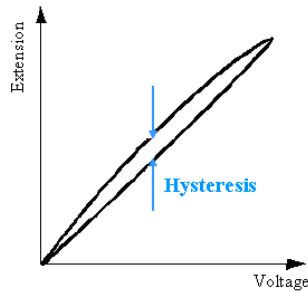


Figure 4.2, hysteresis effect in piezo tube actuator due to signal processing

There are generally two factors contributing to hysteresis: the maximum value of the input signal and its frequency. Under the impacts of a single factor mentioned above or a combination of both, hysteresis may appear and for a given input, there are more than one possibility for the output, leaving no way of modeling or predicting system behaviors without additional information, and inevitably leading to system instability.

Hysteresis modeling

Controls of hysteresis necessitate understanding of the relationship between the input and output and an accurate modeling of this effect. The polynomial equation is first cited to address this problem by capturing the major loops in I/O response. However, it failed to describe the minor loops [11], resulting in significant errors when dealing with complex inputs, such as signal inputs with multiple frequencies or amplitudes. Afterwards, on the basis of the polynomial method, Coleman-Hodgdon equations are developed to describe the nonlinearity of the hysteresis for a fixed-amplitude input. However, this recipe is not capable of resolving problems with multiple amplitude inputs [31].

Another commonly used approach to model the hysteresis is the classical Preisach hysteresis model [38][39], which can deal with different types of actuators with precise descriptions at a given frequency. This approach, however, is not rate-dependent and can be only used for single frequency applications. To compensate this phenomenon, a dynamic nonlinear Preisach method is modeled and applied in between the input and output, followed by a linear creep and vibration submodel. More information can be found in reference [11].

In addition, for different utilities, there are also other available models, such as the Maxwell resistive capacitor (MRC) model [40], the Prandtl–Ishlinskii model [41], the multiple linear-play models [42], the differential equation models [43], as well as the deterministic path models [44].

Material selection

How to take care of the hysteresis effect since it does no good to the system instability? One way to solve this problem is, from the material perspective, to try to find some natural or composite materials which could, to a certain extent, minimize the hysteresis effect, if not being totally immune to it. For most PZT materials, the charge constant increases with increments of the applied field strength, such as Nab-doped PZT, while some materials are quite insensitive, SrBi₄Ti₄O₁₅, (PbSm) TiO₃, PZT4 and PZT 8 for instance. Therefore, designers should be aware of the role that the piezoelectric materials played in actuator performance, and choose a suitable material to ensure of an optimized design.

Current/Charge drive

Another approach to eliminate hysteresis can be achieved by current/charge drive, which is considered to be a simple alternative compared to the solutions with massive and complicated control algorithms. It is commonly applied with piezoelectric shunt damping, a technique by directly attaching LCR impedance to the tube to damp vibrations, especially for nanostructure usage [30]. As given in the reference [16], the current drive approach can give a fivefold reduction of the hysteresis in contrast with the voltage drive. According to the DC accurate charge amplifier design provided by reference [5] [30], a general schematic of the current drive scheme is demonstrated in Figure 4.3, where the piezoelectric tube is modeled as a capacitor CL and the voltage across is denoted as Vp, both confined in the gray box. Thanks to the feedback opamps, it is fairly evident that the voltage across the capacitor Cs is equivalent to the reference voltage Vref, a representative of the input signal.

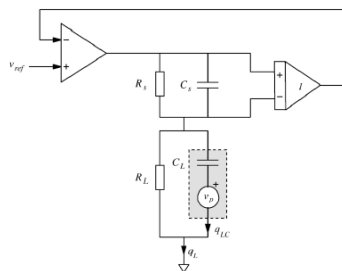


Figure 4.3, accurate charge amplifier design

The transfer function of this design was derived and showed in reference [30] [45]. As its expression suggests, as long as $RLCL=RSCS$, the system will have a constant gain of CS and a cut-off frequency in the order of $1/(2\pi RLCL)$, almost without low frequency dynamics. It can be also found that the system is charge dominated above the frequency of $1/(2\pi RLCL)$, and voltage dominated below. With an appropriate setup, experimental results under current drive shows a better scan image, where imperceptible errors appears with the value of around 1% compared to the big nonlinearity of 7.2% measured with the voltage-drive. However, despite that the charge/current drive is quite efficient at eliminating hysteresis; it can cause problems like voltage drift, poor low frequency response and saturation [31].

Control algorithms

Other ways to compensate hysteresis are mostly developed on the basis of control algorithms. One of the effective ways is achieved by using feed forward hysteresis compensation as given in the reference [11]. It generally includes the procedure of fitting the hysteresis to one of the models that was described in the section of hysteresis modeling, inverting the obtained model and feeding the desired output through to obtain the input signal. However, the challenge of this method is the complexity of the modeling process and its sensitivity to the noises.

In reference [46], adaptive and iterative control is implemented by using Preisach model to control hysteresis in smart materials, whereas it is difficult to prove the convergence of hysteresis and to find a unique response, as one single input usually corresponds to several output values. In addition, other control algorithms like Integral feedback, PID feedback, and double integral feedback, can also functionalize and be adopted to compensate the hysteresis.

A.4.1.2 Creep

Creep is another nonlinear effect found in piezoelectric tube applications. It happens when the actuator subjects to a signal with abrupt changes, such as step input or impulse input [29], which will lead to significant distortions as a scanning is usually executed in over extended periods of time at an offset position from the center of the positioning range [31]. The reason behind this effect is based on the dipolar-orientation-modification-caused material property change. As a result, the performance of the output, as shown in figure 4.4, has a slower changing rate at every end of the signal skyrocketing or plummeting period. Additionally, as indicated in reference [17], creep may exacerbate the effect of hysteresis at the turning point of the scanning trajectory.

Creep modeling

A general way to compensate the creep initiated nonlinearity is by using control algorithms, which are primarily developed on the basis of creep modeling. In general, there are two forms of models that can be used in practical applications: one is the linear creep model which is modeled as series of numbers of springs and dampers to capture the low frequency response of the actuator [31]. And the other one is the nonlinear creep model described in reference [47], which is applied associated with a PI controller to eliminate the creep effect. Note that creep is of little consequence in fast scanning probe microscopy. However, due to the fact that most SPMs are operated quite slowly, creep can not be overlooked [48].

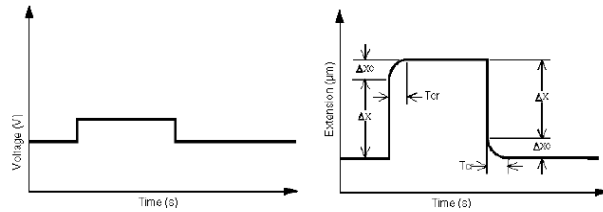


Figure 4. 4, voltage impulse input (left) for piezo tube actuator and its output (right) [29]

Integral feedback

In reference [11], an approach for compensating creep is realized by making use of an integral controller, which can provide high feedback gain at low frequency to compensate nonlinearity properties as shown in Figure 4.5. This control method can be also applied for creep compensations in high frequency operations, as long as the controller gain is set sufficiently high to overcome vibration induced errors. However, the improvements based on the high gain setting is eliminated by the low-gain-margin property of a piezoelectric actuator, resulting from a rapid lose in phase at the sharp resonance peak in its dynamic response. One possible solution is by employing a notch filter to modify the first resonance peak, which will be detailed in advanced methods in section 4.1.3. Apart from the above mentioned methods, traditional proportional-integral-derivative (PID) feedback controllers, as well as double integral controllers can also fulfill similar functions and be adopted in different applications.

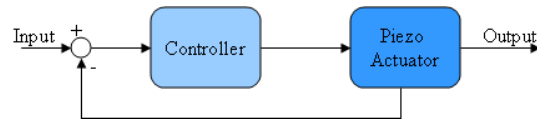


Figure 4. 5, feedback control scheme to compensate creep

A.4.1.3 Vibration

Same as the other mechanical structures, a piezoelectric scanner is also subject to vibrations when actuated at or near its resonance frequency, which is not acceptable for high precision demanding scanning. To avoid vibrations, the operational bandwidth for piezoelectric tube actuator is confined quite low, usually lower than 1/100 of its resonance frequency. In general, there are different angles that one can work on to reject or eliminate vibrations, such as to increase the first resonance frequency by optimizing the geometry of the actuator (to make it stiffer) or to reduce external disturbances. Concrete solutions are demonstrated below.

Positive Position Feedback (PPF)

One of the most successful control algorithms for vibration reduction so far is the Positive Position Feedback (PPF), which can suppress vibrations due to absences or insufficient of system damping. According to reference [14], an original form of PPF controller is adopted and positively back fed, with a simple control scheme shown in Figure 4.6, where the tube structure is modeled by system identification as a second order dynamic system marked with G. Additionally, assisted by the senseless control method (elaborated at the end of this section), this approach shows satisfactory results in eliminating vibrations.

A disadvantage of this control algorithm is that it is comparable difficult to decide the root locus of a PPF controller [15], which is usually intractable and experience demanding. Yet, as indicated in reference [14], it is always good to start with the controller frequency half value of the original system frequency, which although might not be an optimal value.

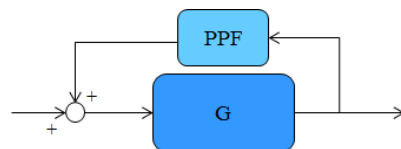


Figure 4. 6, PPF for vibration control [14]

Positive Position and Velocity Feedback (PVPF)

Analogous to the method of PPF, PVDF, in fact a modification of PPF, is considered to be more suitable for vibration controls for the piezoelectric materials. And the detailed instructions about the controller design process and parameter selections can be found in reference [16]. Again, the high resonance modes of the tube are neglected and a second-order dynamic model is hereby considered as a representative of the tube structure. In general, The PVPF takes the form as given in equation (10).

$$K_{PVPF}(S) = \frac{\Gamma_1 s + \Gamma_2}{s^2 + 2\zeta\omega s + \omega^2} \quad (10)$$

By convention, a well damped system requires all roots allocated inside the left half plane. By calculating the transfer function of the closed system, one can easily find its poles, and choosing an appropriate parameter in this case can better help achieve a stable system. With the obtained result, there is no denying that PVDF can effectively reduce vibrations and improve actuator performances.

Integrated Resonate Control (IRC)

Integrated resonate control, acronym for IRC, is a feedback control algorithm that used to damp the resonate frequencies of the tubes and increase their operational bandwidths for high speed scanning. In reference [15], combined with a feed through item d, an integral controller is tried straight forward to compensate mechanical vibrations (normally 5-10Hz), with a simple scheme shown in figure 4.7.

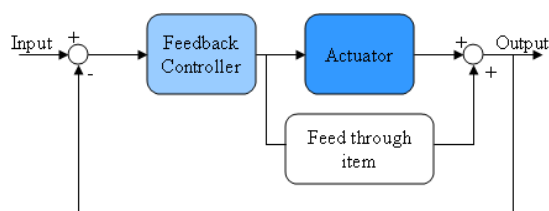


Figure 4.7, closed loop system with the integral controller [15]

The transfer function in this case can be easily calculated, and according to the Hermite Biehler theorem that for a stable system, the roots of the imaginary part of the denominator of the transfer function must be less than the absolute value of the roots of its real part [15], one may find appropriate values for parameters of the controller. And as experimental result suggests, the tube performance with IRC controller shows impressive improvements on vibration reductions at frequency as high as 0.1 of its resonance frequency.

Iterative control

Since the scanning motions of a piezoelectric tube actuator are repetitive, the vibration problem can then be tackled by iterative control, which can significantly reduce the accumulated scanning errors and increase the operational bandwidth without influencing the precision. This method is extremely useful for applications where probe and sample interactions are needed, especially for biological applications.

Senseless control

One of the main vibration sources is induced by applications of external sensors, which are usually quite expensive and difficult for integrations in compact Microsystems. A good way to tackle this problem is by using the piezo tube itself as a sensor to transform the mechanical deflections into electrical signals, as piezo tube structures can work as sensors in virtue of direct piezoelectric effect. This internal sensor design is depicted in figure 4.8, where one of the opposite electrodes is used as an actuator, and the other one is regarded as a sensor, with its sensed signal back fed as controller input. However, the disadvantage of this method is that only one of the electrodes is used for actuation, making the test signal half amplitude of the signals measured from designs with external sensors.

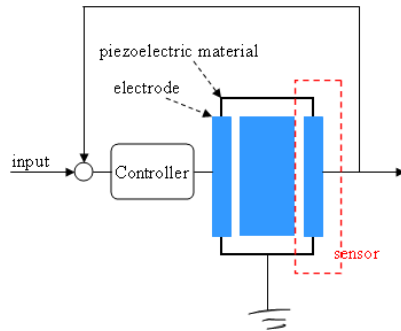


Figure 4.8, sensorless feedback control by using internal sensor combined with feedback controller

Another senseless control technique is called shunt damping which is achieved by connecting an impedance to an electrode pair, x-x or y-y, with the other end grounded [11] [30]. A configuration of this design is depicted in Figure 4.9. The impedance in this case can be regarded as a compensator which can generate electrical resonances to reduce the amplitude of the structure dynamic resonances. An advantage of this approach, compared to the internal sensor design, is that after a short period modification of the impedance, the terminal for signal detection can be again used as actuators, leading to a full range scanning.

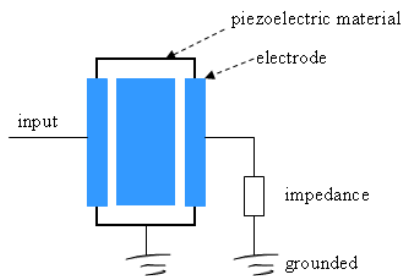


Figure 4.9, sensorless control with shunt damping

Advance method

The solutions introduced above mostly aim at solving one particular problem, however, in practical applications, hysteresis, vibrations or creep do not appear to be lonely. Therefore, a good actuation system should be capable of dealing with all these problems simultaneously. Of course, it is possible to combine the potential solutions introduced above to achieve a complete control system, however, such solution often ends up with a complicated control algorithm which will be quite difficult to implement and likely cause additional problems. Therefore, advanced solutions that raised in early years are also presented.

▪ State feedback systems

As is known, velocity feedback can help move the oscillating poles of a system to the left in the s-plane to depress resonances. In the reference [50], a state feedback mechanism is employed by using a first state observer to obtain the velocity information, achieved by calculating the derivative of the displacement information which can be directly measured by sensors. The derived velocity and the measured displacement will be together back fed in order to increase the system damping at high resonance frequency. The experiment result shows significant improvements on suppressions of the resonance peaks, including the main resonance and the sub-resonance just below it.

▪ Notch filter feedback

In this mechanism, vibration control is achieved by the usage of a notch filter, which can cancel the resonance peaks of a tube structure. As shown in figure 4.10, the control algorithm is implemented with associations of an integrator to obtain a high loop gain in the low frequency range, and a low-pass filter to attenuate the peaks within the desired higher band [50]. The testing result of this design shows high improvements on not only the operation speed, but also the system stability.

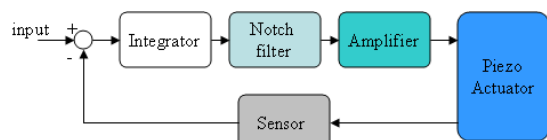


Figure 4. 10, notch filter feedback control

▪ Model based inversion feedback approach

Another approach to improve operation accuracy and scanning speed is achieved by using inverse model as illustrated in the dashed frame in Figure 4.11. This design is further accomplished by feedback control to achieve a stable performance. The composition of the series of inverse submodels makes the control system capable of suppressing hysteresis, vibration and creep at the same time. The modeling of different effects is achieved by controlling the input signals of their frequencies or amplitudes to eliminate the other effects, leaving the tube structure manifesting one effect at a time. Detailed information about the modeling process can be found in Reference [31].

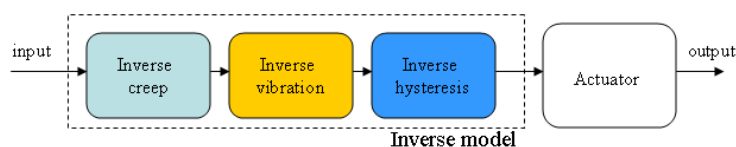


Figure 4. 11, inverse model control

A.4.1.4 Thermal drift

As the piezoelectric material is quite sensitive and the operational environment of the SPM is not constant, any changes in temperature will cause contractions or expansions of the tube itself. Additionally, different parts of the piezo tube have different thermal expansion coefficients as they are manufactured in different materials [51]. In a typical AFM operated in ambient temperature, a 1° change in temperature can cause a 50 nm drift [52]. Although this effect can be suppressed in low temperature experiments (mainly in UHV SPMs), applications of interrogations or manipulations with matters in ambient temperature still amount to substantial hurdles.

A number of techniques have been proposed to compensate this effect. Recent research [52] proved that Kalman filtering technique can help make estimations according to the measurements and effectively reduce thermal drifts. Ito et al. developed the method of using computer controlled servomechanism to lock the STM tip to improve the system resolution [53]. And in reference [54], Rahe et al. present a recipe by using the measured drift velocity to correct both lateral and vertical linear thermal drift.

A.4.1.5 Tradeoff

As it has been indicated in section 3, different criteria reflect emphases of different measuring requirements. For example, requirement of a clear scanning image might ask for a system with high resolution, while the scan speed in this case might not be that important, and vice versa. The relations between system bandwidth and the other criteria, like scan range, precision, have been stressed in section 3; hereby some other existing relations are demonstrated.

Scan speed vs. precision

For each scan point at the x or y plane, there should be a respective z-coordinate to fulfill the 3 dimensional image reconstructions. Therefore, a higher scan speed in the x, y plane will result in a fast positioning at z direction as well. However, if the sample surface is quite rough, the time for z axis positioning might be too short that the tip has not enough time to have a full response according to the surface structure. That is to say, no sufficient information can be attained to reflect the roughness of the surface. As such, the performance on precision would be quite low, which proves the relation that scanning speed is inversely proportional to the precision.

Precision vs. scan range

As explained in section 3, bandwidth is inversely proportional to the scan range, and scan precision as well, the relation between the scan range and precision can be perceived to be in direct proportion. Additionally, noises in digital controller implementations also contribute to this relation. For example, analog-to-digital conversion (when using analog sensors such as thermal and capacitive sensors) as well as digital-to-analog conversion (for actuation) can introduce noise, which adversely affects the controller performance [11].

A.4.1.6 Cross coupling

Cross-coupling refers to the effect that motions along one axis (x, y or z axis) have a ripple effect on either of the other two axes, and this represents one of the main complications existing in actuations of the piezoelectric tubes. In general, the cross-coupling effect can be grouped in two categories: one is the in plane coupling, meaning the coupling between x and y axis; and the other is the out plane coupling, referring to the motion interferences between the x (and y) axis and the z axis.

To generate a raster scan pattern, the SPM actuator is usually driven by a triangular signal along the x axis and a synchronized staircase or ramp signal along the y axis, with the triangular waveform consisting of all odd harmonics of the fundamental frequencies. Although with attenuations, these electrical signals may still excite the resonance modes of the tube actuator. As a consequence, the signal applied to the x-axis and y axis will not only corrugate the traced trajectory in the x-y plane, but also cause deviations along the z axis [55]. Note that the effect of the y-axis movement on the z axis tends to be less prominent because the y scan frequency is substantially smaller than the x scan frequency.

Besides the reason mentioned above, geometric change is another primary contribution to the out-plane coupling. For example, if one of the electrode pairs, either x-x or y-y, is supplied with an electrical signal, due to the piezoelectric effect, one electrode of the pair will shrink, while the other one will get expanded at the same time. As a result, the tube will bend with an arc trajectory at its end, which more or less changes the z coordinate of the tip. In figure 4.12, the out plane coupling effect on z axis is plotted as a function of the x- axis motion. As can be observed, the extent to which the coupling effect impacts the z axial motions depends on the scan range in the x-y plane. In addition, other reasons, for example, the electric field is not uniform across the scanner, the strain field is not a constant, also contribute to the coupling effect [43].

Kinematic model

Tian et al. in reference [56] reported the method of using kinematic model to solve the scanning size error and out plane cross coupling error. Since the tube will have lateral translations and rotate motions when subject to electrical signals, a mathematic model is derived to quantitatively calculate these deflections. As the developed model suggests, the cross coupling error is dependent on the tip offset relative to the tube axis, nominal scanning size and sample thickness; with a zero tip offset and with a small scan range, the cross coupling phenomenon can be effectively eliminated. In the occasions when the tip offset can not be calibrated by simply adjusting the scanner base position, the report suggests a way of compensating errors according to the kinematic model in the process of operation.

Mechanical decoupling

Yong et al. presented a method in reference [24] to mechanically attenuate the effect of cross coupling. The essential of this method is to replace the original tube design with some hinged structures to increase system stiffness to reduce relative motions. The concept of this design was briefly described in section 2.

H controller feedback

In this method, the H controller is employed to minimize the in-plane coupling (between x and y axis) of the tube actuator, particularly at its mechanical resonance frequency. For simplicity, the dynamic motions of the tube structure along x and y direction are separately modeled as second order systems, with its out-of-bandwidth modes neglected. The control scheme is given in figure 4.13. As critical components to reduce coupling effect, two low order band pass weighting functions W_{bpx} , W_{bpy} are separately adopted at the x, and y axis, with both tuned at the first resonance frequency of its corresponding axis to suppress the cross coupling effect, as profound

impacts will be generated when operated at these frequencies. Additionally, W_u , a constant coefficient, is applied to limit signals to avoid saturations, as well as a W_p controller to erase good axis tracings.

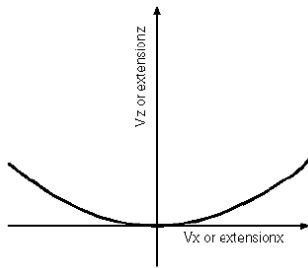


Figure 4.12, out plane coupling, motions along x axis causes deflections in the z axis [29]

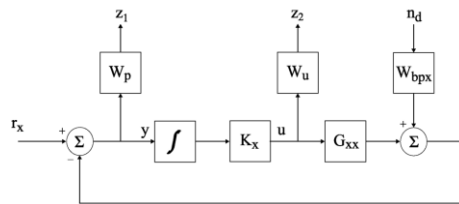


Figure 4.13, H controller feedback control scheme

Open loop controller with H model

In reference [56], Schitter et al. developed an H model based open loop controller to compensate lateral oscillations of a piezoelectric tube actuator stemming from its mechanical resonances. For practical applications, particular scanning requirements, such as accurate tracings, suppressed errors at high frequencies, are always appreciated as to accomplish different tasks. Surprisingly, The H model allows designers to transform these requirements into mathematic equations and allows calculating the open loop controller through the obtained functions. By making use of this open loop controller, the experimental result shows significant improvements on out-plane cross coupling.

Iterative inversion-based feed forward control

A special control algorithm, with an iterative inversion-based feed forward controller, is raised in reference [35] to augment current feedback and to reduce the x-z dynamic coupling effect. The scheme of this control system is depicted in Figure 4.14, where a feed forward input, denoted as u_{ff} , is chosen with the inversion-based approach to compensate the deflections that might appear due to the x-z dynamic coupling. This inverse input can be further used as an input in an iterative approach to compensate the accumulated coupling error.

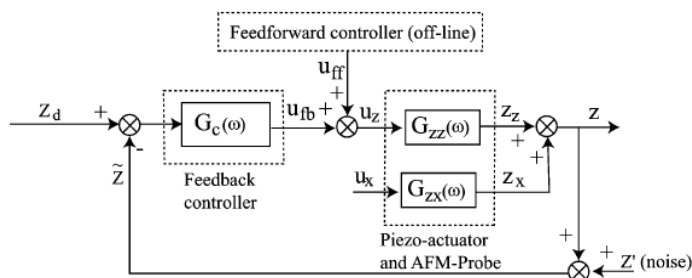


Figure 4.14, Iterative inversion-based feed forward control

A.4.1.7 Aging

Aging is a nonlinearity phenomenon that every piezoelectric tube has to confront to, and it refers to the performance changes of a scanner as a function of its product life. The generation of this effect is caused by the variations of the material properties—mainly the strain constant—due to the electric field applications. As indicated in section 2, most piezoelectric material need to experience a poling procedure to get their randomly

located dipoles realigned, however, the alignments can not ensure all dipoles perfectly orient along the electric field and parallel to each other as shown in figure 2.2 (b). That is to say, the dipoles only roughly point to one direction as shown in figure 2.2 (c). Based on this scenario, when a tube actuator is consistent in usage, it will suffer a prolonged electrical treatment, the roughly aligned dipoles will be better or worse oriented depending on how the electric field aligns, which will either improve or worsen the piezoelectric effect. If it is an improving effect, the performance of the tube structure can be described by the upper line in Figure 4.15.

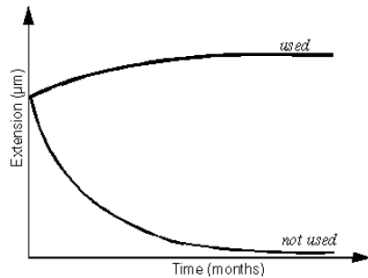


Figure 4. 15, aging of a tube scanner

On the other hand, if a scanner is out of use for quite a long time, the pre-aligned dipoles will gradually return to its original state—randomly aligned--and in that case as showed in the lower curve of Figure 4.15, a fewer dipoles will contribute to deflections of the scanner and the performance quality will get exponentially decreased. To deal with this problem, a good proposal is by frequently using the tube scanner to avoid realignments of the dipoles. In addition, one can also choose materials that are more insensitive or resistant to the aging effect.

A.4.1.8 Modeling error

It has been roughly mentioned in the previous section: modeling errors are generated on the design phase, as in most cases only the first resonance frequency is targeted based on the fact that the tube are normally operated at low frequencies. In such circumstance, higher frequency modes are ignored, as they are considered to have fewer effects on performances of the tube. However they do have impacts and induce errors on system performances. However, modeling of resonance modes in high frequency domains are extremely difficult, the only recipe for this problem is by employing feedback control algorithms [35].

A.4.2 Problems and solutions for voice coil actuator

A.4.2.1 Ringing/ vibration

Despite that the voice coil actuator makes progress at scan performances compared to PZT tube scanners; it has a major disadvantage that its structure usually possesses a quite low damping coefficient such that the system is susceptible to vibrations or sensor noises. One of the related effects is called ringing.

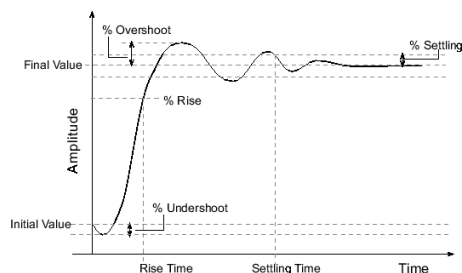


Figure 4. 16, ringing/ vibration effect

Ringling refers to the oscillation effect that appears in signal processing periods, especially when the input is with sudden changes. Due to system imperfection, the output can not exactly follow what the input gives, thus effect like step response occurs as given in Figure 4.16, with overshoot and a gradually damped oscillation. The oscillation effect in that case is called ringling, sometimes referred as ripple, vibration as well. As the VCM basically works on

balancing between the leading spring and electromagnet force, ringing effect will occur and have impacts on system precision if the suspension system is devised without sufficient damping, similar to an undamped second order system. To increase the system damping, two approaches are roughly demonstrated.

Material selection

In the original design of the VCM scanner, the platform, made of stainless steel possesses a high quality factor, which leads to a less damped system as damping is reciprocal to the quality factor. To solve this problem, grease is applied in between the platform and magnets to increase the critical damping of the whole structure for higher speed scanning. However, such design is not compatible in low temperature when the grease gets stiffed, meaning that the system can not offer sufficient damping due to large viscosity variations of the greases or oils [22]. This is very likely to lead to distortions of the scanning images.

In references [21] [22], an approach by using polyimide springs as damping mechanism has been investigated to address the insufficient damping problem within the original design. This solution tackles the problem from the material point of view since each material has its own damping constant, called internal friction sometimes, and it is easy to choose an appropriate material with high damping constant. With testing under certain conditions, Reference [22] demonstrates the damping properties of several different materials, where Polyamides show a lower quality factor than stainless steel and other materials.

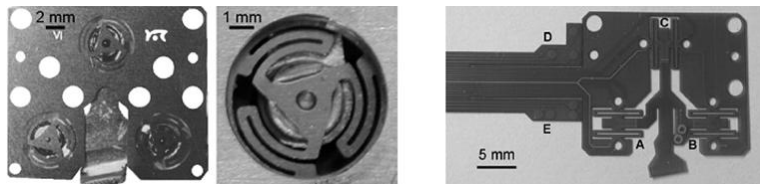


Figure 4. 17, original voice coil actuator with a stainless steel platform (left) and new design with polyamides to increase system damping (right) [21]

With a new structure design as shown in figure 4.17, the experiment result suggests that damping with flex springs is twice higher than that with stainless steel springs (without greases), and proves that this design can efficiently work in low temperature and the corresponding scanning speed is improved more than twice due to the high damping of the polyamides.

Input shaping pre-filter

Another way to solve the problem of ringing/ vibration can be achieved by using an input shaping pre-filter to block the frequencies near to the system resonance frequency. In this way, the system can avoid being interrupted by the unwanted signals. The input shaping pre-filter introduced in [58] [59] actually acts as a band stop filter, which mainly consists of three parts: a low pass filter, a high pass filter and a band pass filter. A configuration of the feedforward part of the compensate scanner is given in figure 4.18. By choosing right parameters for the shaping pre-filter, the vibration effect, as the experimental result shows, has disappeared, which proves the efficiency of this application.

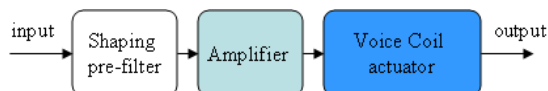


Figure 4. 18, Pre-filter Feedforward control for VCM

A.5 Conclusions

This report demonstrates and compares the different SPM actuators, especially the two popular ones adopted in most of today's commercial microscope products: the piezoelectric tube actuator and the voice coil actuator, which are separately developed on the basis of the inverse piezoelectric effect and the electromagnetic effect respectively. Reading the provided information, one can comprehend their working principles, configurations, actuation methods, etc. This report presents problems that have been found in practical applications with respect to the two actuators, such as hysteresis, creep, vibrations, and the possible solutions developed in recent years. Such information can help designers better understand the problem sources, and choose potential solutions to tackle corresponding problems. In addition, the presence of other SPM actuator concepts that based on either the piezoelectric effect or the electromagnetic effect provides evidences for further developments, and the concept by combining two effects together to achieve 3-DOF actuation seems to be quite intriguing.

As this report aims at summarizing the current situations of the SPM actuators and the previous contributions, the contents presented here are not entirely new. Further developments on SPM actuators can be found in posterior reports.

A. References

- [1] Scanning Tunneling Microscopy (STM), <http://www.fkf.mpg.de/ga/research/stmtutor/stmex.html>
- [2] S. Hla, "STM Single Atom/Molecule Manipulation and Its Application to Nanoscience and Technology", *J. Vac. Sci. Tech.* 2005.
- [3] biological applications of AFM <http://www.chembio.uoguelph.ca/educmat/chm729/afm/applicat.htm>
- [4] <http://vanha.physics.utu.fi/opiskelu/kurssit/SFYS4294/6-AFM.pdf>
- [5] Development of Crosstalk Eliminated (XE) Atomic Force Microscopy, park systems, http://www.parkafm.com/AFM_technology/technology.php.
- [6] B. Bhushan and O. Marti, "Scanning Probe Microscopy-principle of operation, instrumentations and probes", Springer Handbook of Nanotechnology, 2010, Part C, 573-617, DOI: 10.1007/978-3-642-02525-9_21.
- [7] Piezoelectric Effect, PC in control, http://www.pc-control.co.uk/piezoelectric_effect.htm
- [8] Piezoelectric materials, <http://www.piezomaterials.com/>
- [9] C. Bai, "Scanning Tunneling Microscopy and its Application", Springer Series in Surface Science, Berlin, pp. 62-77. 1994.
- [10] piezoelectric effect, <http://www.physics.leidenuniv.nl/sections/cm/ip/Onderwijs/Scanning-Probe-Microscopy/Chapters/CHEN%20Chapter%209%20Piezoelectric%20scanner%2013-235.pdf>
- [11] S. Devasia, E. Eleftheriou, and S. O. R. Moheimani, "A survey of control issues in nanopositioning", *IEEE Transactions on Control Systems Technology*, vol. 15, no. 5, pp. 802–823, September 2007.
- [12] A. J. Fleming and S. O. R. Moheimani, "Sensorless vibration suppression and scan compensation for piezoelectric tube nanopositioners", *IEEE Trans. Control Syst. Technol.*, vol. 14, no. 1, pp. 33–44, Jan. 2006.
- [13] Review B: Coordinate systems, department of Physics, Massachusetts Institute of Technology. <http://web.mit.edu/8.02t/www/materials/modules/ReviewB.pdf>
- [14] M. Ratnam, B. Bhikkaji, A. J. Fleming and S. O. R. Moheimani, "PPF Control of a Piezoelectric Tube Scanner", Proceedings of the 44th IEEE Conference on Decision and Control, and the European Control Conference 2005, Seville, Spain, December 12-15, 2005.
- [15] B. Bhikkaji and S. O. Reza Moheimani, "Integral Resonant Control of a Piezoelectric Tube Actuator for Fast Nanoscale Positioning", *IEEE/ASME Transactions on Mechatronics*, VOL. 13, NO. 5, October 2008.
- [16] B. Bhikkaji, M. Ratnam, A. J. Fleming and S. O. R. Moheimani, "High-Performance Control of Piezoelectric Tube Scanners", *IEEE Transactions on Control System Technology*, VOL. 15, NO. 5, September 2007.
- [17] S. O. Reza Moheimani, "Invited Review Article: Accurate and fast nanopositioning with piezoelectric tube scanners: Emerging trends and future challenges", *Review of Scientific Instruments* 79, 071101, 2008.

- [18] S. O. Reza Moheimani and Y. K. Yong, "Simultaneous sensing and actuation with a piezoelectric tube scanner", *Review of Scientific Instruments* 79, 073702, 2008.
- [19] S. Robinson, "Driving Piezoelectric Actuators" *Power Electronics Technology*, pp. 40-44, Apr. 2006.
- [20] R. M. Schmidt, "Mechatronic System Design", pp. 113-162, 2009.
- [21] D. Parrat, "Atomic Force Microscopy for Characterizing Dust Particles of the Martian Arctic Soils", 2008.
- [22] D. Parrat, S. Gautsch, L. Howald, D. Brändlin-Müller, N. F. De Rooij and U. Staufer, "design and evaluation of a polyimide system for the scanning force microscope of the phoenix mars mission 2007", In *Proceedings of the 11th European Space Mechanisms and Tribology Symposium*, Lucerne, Switzerland, p 281–287. 2005.
- [23] G. Schitter, K.J. Astrom, B.E. DeMartini, P.J. Thurner, K.L. Turner and P.K. Hansma, "Design and Modeling of a High-Speed AFM-Scanner", *IEEE Transactions on Control Systems Technology*, Volume 15, pp. 906 – 915, Sept. 2007.
- [24] Y.K. Yong, K. Liu, S. O.R. Moheimani, "reducing cross coupling in a compliant XY nanopositioner for fast and accurate raster scanning", *IEEE Transactions on Control System Technology*, Volume 18, pp.1172-1179, Sept. 2010.
- [25] P. Vettiger, M. Despont, U. Drechsler, U. Durig, W. Haberle, M. I. Lutwyche, H. E. Rothuizen, R. Stutz, R. Widmer and G. K. Binnig, "The "milliped"- more than one thousand tips for future AFM data storage", *IBM J. Res. Dev.* 2000, 44, 323. Nanoink, Inc. (<http://www.nanoink.net>).
- [26] G. K. Binnig, G. Cherubini, M. Despont, U. T. Dürig, E. Eleftheriou, H. Pozidis, P. Vettiger, "the millipede- a nanotechnology-based AFM data storage system", *IBM Journal of Research and Development*, 2000.
- [27] M. A. Lantz, H. E. Rothuizen, U. Drechsler, W. Häberle, and M. Despont, "A Vibration Resistant Nanopositioner for Mobile Parallel-Probe Storage Applications", *Journal Of Microelectromechanical Systems*, VOL. 16, NO. 1, Feb. 2007.
- [28] A. Knoll, P. Bächtold, J. Bonan, G. Cherubini, M. Despont, U. Drechsler, U. Durig, B. Gotsmann, W. Häberle, C. Hagleitner, D. Jubin, M.A. Lantz, A. Pantazi, H. Pozidis, H. Rothuizen, A. Sebastian, R. Stutz, P. Vettiger, D. Wiesmann and E.S. Eleftheriou, "Integrating nanotechnology into a working storage device", *Microelectronic Engineering* 83. 2006.
- [29] R. Howland and L. Benatar, "A practical guide to scanning probe microscopy", Copyright by ThermoMicroscopes, 2000.
- [30] A. J. Fleming and S. O. R. Moheimani, "Sensorless Vibration Suppression and Scan Compensation for Piezoelectric Tube Nanopositioners", *IEEE Transactions on Control Systems Technology*, VOL. 14, NO. 1, pp. 33-44, January, 2006.
- [31] D. Croft, G. Shed and S. Devasia, "Creep, Hysteresis, and Vibration Compensation for Piezoactuators: Atomic Force Microscope Application", *Journal of Dynamic Systems, Measurement, and Control*, 123(1), 35–43. 2001.
- [32] Bandwidth, URL: <http://cnx.org/content/m13375/latest/>.
- [33] S. Balemi, J. Moerschell, J. M. Breguet, D. Brändlin, S. Bottinelli and I. Beltrami, "Surface inspection system for industrial applications", *Surface inspection system for industrial applications*, Mechatronics and Robotics, Aachen, Sept. 2004.
- [34] G. Song, S. Schmidt and B. N. Agrawal, "Experimental Study of Vibration Suppression of Flexible Spacecraft using Modular Control Patch", *Proc. of IEEE Aerospace Conference*, Snowmass, Colorado, 1998.

- [35] S. Tien, Q. Zou, and S. Devasia, "Iterative control of dynamics-coupling- caused errors in piezoscanners during high-speed AFM operation", *IEEE Trans. Control Syst. Technol.*, vol. 13, no. 6, pp. 921–931, Nov. 2005.
- [36] J. Maess, A. J. Fleming and F. Allgöwer, "Simulation of Piezoelectric Tube Actuators by Reduced Finite Element Models for Controller Design", *Proceedings of the 2007 American Control Conference*
Marriott Marquis Hotel at Times Square New York City, USA, July 11-13, 2007.
- [37] D. Damjanovic, "Hysteresis in piezoelectric and ferroelectric materials", in *The Science of Hysteresis*, edited by I. Mayergoyz and G. Bertotti (Elsevier, New York, 2005).
- [38] J. M. Cruz-Hernández and V. Hayward, "Phase Control Approach to Hysteresis Reduction", *IEEE Transactions on control system technology*, VOL. 9, NO. 1, January, 2001.
- [39] P. Ge and M. Jouaneh, Member, "Tracking Control of a Piezoceramic Actuator", *Transactions on control system technology*, VOL 4, NO 3, MAY 1996.
- [40] M. Goldfarb and N. Celanovic, "A lumped parameter electromechanical model for describing the nonlinear behavior of piezoelectric actuators", *J. Dyn. Syst., Meas., Control*, vol. 119, pp. 478–485, Sep. 1997.
- [41] K. Kuhnene and H. Janocha, "Inverse feedforward controller for complex hysteretic nonlinearities in smart-material systems", *Control Intell. Syst.*, vol. 29, no. 3, pp. 74–83, 2001.
- [42] H. Janocha and K. Kuhnen, "Real-time compensation of hysteresis and creep in piezoelectric actuators", *Sensors Actuators A*, vol. 79, pp. 83–89, 2000.
- [43] H. J. M. T. A. Adriaens, W. L. de Koning, and R. Banning, "Modeling piezoelectric actuators", *IEEE/ASME Trans. Mechatron.*, vol. 5, no. 4, pp. 331–41, Dec. 2000.
- [44] S. B. Jung and S. W. Kim, "Improvement of scanning accuracy of PZT piezoelectric actuators by feed-forward model-reference control", *Precision Eng.*, vol. 17, pp. 49–55, 1994.
- [45] A.J. Fleming and K.K. Leang, "Charge drives for scanning probe microscope positioning stages", *Ultramicroscopy* 108, pp. 1551– 1557, 2008.
- [46] X. Tan and J. S. Baras, "Adaptive identification and control of hysteresis in smart materials", *IEEE Trans. Autom. Control*, vol. 50, no. 6, pp. 827–839, Jun. 2005.
- [47] H. Jung, J. Y. Shim, and D. Gweon, "New open-loop actuating method of piezoelectric actuators for removing hysteresis and creep", *Rev. Sci. Instrum.*, vol. 71, no. 9, pp. 3436–3440, Sep. 2000.
- [48] S. O. Reza Moheimani, "Invited Review Article: Accurate and fast nanopositioning with piezoelectric tube scanners: Emerging trends and future challenges", *Reviw OF Scitific Instruments* 79, 071101. 2008.
- [49] S. Tien, Q. Zou, and S. Devasia, "Iterative control of dynamics-coupling- caused errors in piezoscanners during high-speed AFM operation", *IEEE Trans. Control Syst. Technol.*, vol. 13, no. 6, pp. 921–931, Nov. 2005.
- [50] Y. Okazaki, "A micro-positioning tool post using a piezoelectric actuator for diamond turning machines", *Prec Eng*, pp. 151-156, 1990.
- [51] Vorlesungsskript Physikalische Elektronik und Messtechnik
http://wwwex.physik.uniulm.de/lehre/physikalischeelektronik/phys_elektr/node238.html

- [52] B. Mokaberi and A. A. G. Requicha, "Towards automatic nanomanipulation: drift compensation in scanning probe microscopes", Proc. IEEE Int'l Conf. on Robotics and Automation, New Orleans, LA, pp. 416-421, April 25-30, 2004.
- [53] K. J. Ito, Y. Uehara, and S. Ushioda, "Servomechanism for locking scanning tunneling microscope tip over surface nanostructures", Review of scientific instruments, Volume 71, Number 2 February, 2000.
- [54] P. Rahe, R. Bechstein, and A. Kühnle, "Vertical and lateral drift corrections of scanning probe microscopy images", Journal of Vacuum Science & Technology B, Volume 28, Issue 3, 2010.
- [55] basic calculations on actuators, "Piezoelectric ceramic properties & applications", <http://www.morganelectroceramics.com/download.php?6532623650657334754e666d533032362f424c587a554c56697858794849732b3763434955656d76387877765773d3d>.
- [56] X. J. Tian, Y. C. Wang, N. Xi, et al. "A study on single CNT's accurate assembly and electrical contact for fabricating nanoelectronic device", Journal of Chinese Electron Microscopy Society (in Chinese), May 2006.
- [57] G. Schitter, A. Stemmer, "Model-based signal conditioning for high-speed atomic force and friction force microscopy", Microelectron. Eng., pp. 938-944. 2003.
- [58] G. Schitter, K. J. Astrom, B. E. DeMartini, P. J. Thurner, K. L. Turner, and P. K. Hansma, "Design and modeling of a high-speed AFM-scanner", IEEE Trans. Control Syst. Technol., Vol. 15, No. 5, pp. 906-915 (2007).
- [59] W. Youm, J. Jung, S. Lee and K. Park, "Control of voice coil motor nanoscanners for an atomic force microscopy system using a loop shaping technique", Review of Scientific Instruments, 79, 013707, 2008.

Appendix C

Voltage(V)	0.00	0.20	0.40	0.60	0.80	1.00	1.20	1.40
Pixel shift	0	2	3	5	6	8	8	10
	0	1	3	4	6	7	8	10
	0	2	2	5	6	7	8	10
	0	2	3	4	6	7	8	10
	0	1	3	4	6	7	9	10
	0	1	3	5	6	7	9	11
	0	2	3	5	6	8	9	11
	0	2	3	5	7	8	9	10
	0	2	3	5	7	7	9	11
	0	1	2	4	6	7	8	10
	0	2	2	4	7	7	9	10
	0	2	3	4	7	8	8	10

Table C 1, the pixel shift of different points under different power input.

Voltage(V)	0.00	0.20	0.40	0.60	0.80	1.00	1.20	1.40
Deflection (m)	0	4.3956E-06	6.5934E-06	1.0989E-05	1.3187E-05	1.7582E-05	1.7582E-05	2.1978E-05
	0	2.1978E-06	6.5934E-06	8.7912E-06	1.3187E-05	1.5385E-05	1.7582E-05	2.1978E-05
	0	4.3956E-06	4.3956E-06	1.0989E-05	1.3187E-05	1.5385E-05	1.7582E-05	2.1978E-05
	0	4.3956E-06	6.5934E-06	8.7912E-06	1.3187E-05	1.5385E-05	1.7582E-05	2.1978E-05
	0	2.1978E-06	6.5934E-06	8.7912E-06	1.3187E-05	1.5385E-05	1.9780E-05	2.1978E-05
	0	2.1978E-06	6.5934E-06	1.0989E-05	1.3187E-05	1.5385E-05	1.9780E-05	2.4176E-05
	0	4.3956E-06	6.5934E-06	1.0989E-05	1.3187E-05	1.7582E-05	1.9780E-05	2.4176E-05
	0	4.3956E-06	6.5934E-06	1.0989E-05	1.5385E-05	1.7582E-05	1.9780E-05	2.1978E-05
	0	4.3956E-06	6.5934E-06	1.0989E-05	1.5385E-05	1.5385E-05	1.9780E-05	2.4176E-05
	0	2.1978E-06	4.3956E-06	8.7912E-06	1.3187E-05	1.5385E-05	1.7582E-05	2.1978E-05
	0	4.3956E-06	4.3956E-06	8.7912E-06	1.5385E-05	1.5385E-05	1.9780E-05	2.1978E-05
	0	4.3956E-06	6.5934E-06	8.7912E-06	1.5385E-05	1.7582E-05	1.7582E-05	2.1978E-05

Table C 2, the corresponding deflection calculated based on the pixel shifts in Table C1

Appendix D

Input voltage (V)	1-layer design (m)	2-layer design (m)	3-layer design (m)	4-layer design (m)
0	0.0000E+00	0.0000E+00	0.0000E+00	0.0000E+00
10	1.0767E-05	2.1849E-05	3.2300E-05	4.3154E-05
20	2.1535E-05	4.3698E-05	6.4599E-05	8.6309E-05
30	3.2302E-05	6.5547E-05	9.6899E-05	1.2946E-04
40	4.3069E-05	8.7395E-05	1.2920E-04	1.7262E-04
50	5.3836E-05	1.0924E-04	1.6150E-04	2.1577E-04
60	6.4604E-05	1.3109E-04	1.9380E-04	2.5893E-04
70	7.5371E-05	1.5294E-04	2.2610E-04	3.0208E-04
80	8.6138E-05	1.7479E-04	2.5840E-04	3.4524E-04
90	9.6905E-05	1.9664E-04	2.9070E-04	3.8839E-04
100	1.0767E-04	2.1849E-04	3.2300E-04	4.3154E-04
110	1.1844E-04	2.4034E-04	3.5530E-04	4.7470E-04
120	1.2921E-04	2.6219E-04	3.8760E-04	5.1785E-04
130	1.3997E-04	2.8404E-04	4.1990E-04	5.6101E-04
140	1.5074E-04	3.0588E-04	4.5220E-04	6.0416E-04
150	1.6151E-04	3.2773E-04	4.8450E-04	6.4732E-04
160	1.7228E-04	3.4958E-04	5.1680E-04	6.9047E-04
170	1.8304E-04	3.7143E-04	5.4910E-04	7.3363E-04
180	1.9381E-04	3.9328E-04	5.8140E-04	7.7678E-04
190	2.0458E-04	4.1513E-04	6.1370E-04	8.1994E-04
200	2.1535E-04	4.3698E-04	6.4599E-04	8.6309E-04

Table D 1, the influence of the power input on the maximum deflection.

Bender length (m)	1-layer design (m)	2-layer design (m)	3-layer design (m)	4-layer design (m)
7.0000E-03	2.4062E-07	6.3345E-07	7.5777E-07	1.1210E-06
8.0000E-03	4.9249E-07	1.1116E-06	1.4987E-06	2.0901E-06
9.0000E-03	8.4853E-07	1.8616E-06	2.4968E-06	3.3639E-06
1.0000E-02	1.2581E-06	2.6759E-06	3.7233E-06	5.0673E-06
1.1000E-02	1.7477E-06	3.6550E-06	5.2469E-06	6.9987E-06
1.2000E-02	2.3310E-06	4.8447E-06	6.9482E-06	9.2329E-06
1.3000E-02	2.9751E-06	6.1361E-06	8.8679E-06	1.1850E-05
1.4000E-02	3.6451E-06	7.5430E-06	1.0968E-05	1.4742E-05
1.5000E-02	4.4484E-06	9.1454E-06	1.3401E-05	1.7894E-05
1.6000E-02	5.3346E-06	1.0927E-05	1.6021E-05	2.1425E-05
1.7000E-02	6.2812E-06	1.2843E-05	1.8804E-05	2.5100E-05
1.8000E-02	7.3162E-06	1.4790E-05	2.1908E-05	2.9156E-05
1.9000E-02	8.4068E-06	1.7025E-05	2.5138E-05	3.3710E-05
2.0000E-02	9.5449E-06	1.9415E-05	2.8617E-05	3.8226E-05
2.1000E-02	1.0767E-05	2.1849E-05	3.2410E-05	4.3154E-05

Table D 2, the influence of the bender length on the maximum deflection.

Gluewidth/Overlap (m)	1-layer design (m)	2-layer design (m)	3-layer design (m)	4-layer design (m)
0.001	1.5029E-05	2.9902E-05	4.4671E-05	5.9710E-05
0.002	1.2872E-05	2.5851E-05	3.8510E-05	5.1378E-05
0.003	1.0767E-05	2.1849E-05	3.2410E-05	4.3154E-05
0.004	8.8552E-06	1.8148E-05	2.6761E-05	3.6022E-05
0.005	7.1529E-06	1.4758E-05	2.1515E-05	2.8857E-05
0.006	5.5697E-06	1.1586E-05	1.6850E-05	2.2622E-05
0.007	4.1325E-06	8.6877E-06	1.2550E-05	1.6813E-05
0.008	2.9058E-06	6.2008E-06	8.7002E-06	1.1640E-05
0.009	1.7600E-06	3.8521E-06	5.2887E-06	7.2060E-06
0.01	7.9483E-07	1.8816E-06	2.2397E-06	3.1854E-06

Table D 3, the influence of the overlap/glue width on the maximum deflection